UCGE Reports
Number 20201

Department of Geomatics Engineering

Modeling Inertial Sensors Errors Using Allan Variance

(URL: http://www.geomatics.ucalgary.ca/links/GradTheses.html)

by

Haiying Hou

September 2004

UNIVERSITY OF CALGARY

Modeling Inertial Sensors Errors Using Allan Variance

by

Haiying Hou

A THESIS

SUBMITTED TO THE FACULTY OF GRADUATE STUDIES

IN PARTIAL FULFILMENT OF THE REQUIREMENTS FOR THE

DEGREE OF MASTER OF SCIENCE

DEPARTMENT OF GEOMATICS ENGINEERING

CALGARY, ALBERTA

September, 2004

ABSTRACT

It is well known that Inertial Navigation Systems (INS) can provide high accuracy information on the position, velocity, and attitude over a short time period. However, their accuracy degrades rapidly with time. The requirements for accurate estimation of navigation information necessitate the modeling of the sensors' noise components.

Several methods have been devised for stochastic modeling of inertial sensors noise. Each of them is useful but each has its own disadvantage. The Adaptive Kalman filter is one of the mostly used methods to estimate inertial sensor noise, but the form of the model needs to be known first. Frequency domain approaching uses the power spectral density to estimate transfer functions. It is straightforward but it is difficult for non-system analysts to understand. In the time domain methods, the correlation function approach is very model sensitive. Variance techniques are basically very similar, and primarily differ only in that various signal processing, by way of weighting functions, window functions, etc., are incorporated into the analysis algorithms in order to achieve a particular desired result for improving the model characterizations. The simplest technique is the Allan variance method.

Allan variance is a method of representing root mean square (RMS) random drift error as a function of average time. It is simple to compute and relatively simple to interpret and understand. Allan variance method can be used to determine the character of the underlying random processes that give rise to the data noise. This technique can be used to characterize various types of noise terms in the inertial sensor data by performing certain operations on the entire length of data.

In this thesis, the Allan variance technique is used in noise analysis of different grade Inertial Measurement Units (IMU), which include:

- Navigation grade IMU: The Honeywell Commercial IMU (CIMU);
- Tactical grade IMU: The Honeywell HG1700; and

- Consumer grade MEMS based IMU: The Systron Donner MotionPak II-3g

By performing a simple operation on the entire length of data, a characteristic curve is obtained whose inspection provides a systematic characterization of various random errors contained in the inertial sens or output data. Being a directly measurable quantity, Allan variance can provide information on the types and magnitude of various noise terms. The research work will cover both the theoretical basis for Allan Variance for modeling inertial sensors noise terms, and its implementation in modeling different noise terms existing in the different grade inertial sensors. Simple implementation and ease of interpretation make the Allan variance method suitable in inertial sensor noise identification and stochastic modeling.

ACKNOWLEDGEMENTS

I would like to express my sincere gratitude to my supervisor Dr. Naser El-Sheimy for his continuous support, encouragement, guidance and advice, trust, stimulating discussion, proposed ideas and constructive suggestions during my graduate studies. Also, I would like to express my deepest appreciation to Dr. Xiaoji Niu for his constant support, interest in the topic, immeasurable contributions, kind assistance and wonderful friendship throughout my graduate studies.

Thanks are given to all of my colleagues at The University of Calgary, especially my group mates in the Mobile Multi-Sensor System Group: Dr. Sameh Nassar, Kai-Wei Chiang, Eun-Hwan Shin, Walid Abd El-Hamid, Todd Richert, Landra Trevis, Thilanka Galappaththi, and Mahmoud El-Gizawy. My work and discussion with them were always a pleasure that created an ideal working environment for my research.

This research is part of the project led by my supervisor, Dr. Naser El-Sheimy and funded by the Canadian Natural Sciences and Engineering Research Council of Canada (NSERC) and Geomatics for Informed Decisions (GEOIDE) Network Centers of Excellence (NCE).

Finally, I offer my deepest gratitude, appreciation and love to my parents for their unlimited and unconditional love, inspiration, guidance, support, care and

encouragement. I have learned so much from you and gained great confidence in establishing the backbone of my life and future career.

Last but not least, I shall be forever indebted to my wife Xing for her everlasting love, patience, understanding, cooperation, encouragement, pleasant and calm living and working atmosphere, which have certainly contributed a lot to the successful accomplishment of this thesis.

TABLE OF CONTENTS

LIST OF TABLES

LIST OF FIGURES AND ILLUSTRATIONS

NOTATION

1. ACRONYMS

- 3D Three dimensional
- AC Alternating current
- A/D Analog to Digital convert
- ARW Angle random walk
- AV Allan variance
- CIMU Commercial Inertial Measurement Unit
- CWT Continuous wavelet transform
- DFT Discrete Fourier transform
- DTG Dynamically tuned free rotor gyroscope
- DWT Discrete wavelet transform
- ESG Electrostatic Gyro
- FFT Fast Fourier transform
- FPS Foot per second
- FOG Fiber-optic Gyroscope
- GPS Global Positioning System
- IFOG Interferometric fiber-optic gyro
- IMU Inertial Measurement Unit
- INS Inertial Navigation System
- LOD Level of Decomposition

- MEMS Micro electro-mechanical system
- MMS Mobile Multi-Sensor System
- PIGA Pendulous Integrating Gyro Accelerometer
- ppm Part per million
- PSD Power Spectral Density
- RLG Ring Laser Gyro
- RMS Root mean square
- SDM Servo-driven member
- SF Scale factor
- SFS Specific force sensor

2. COORDINATE FRAME

- Operational Inertial Frame (i-frame)
    - Origin: at the centre of mass of the Earth;
    - Z-axis: towards the north celestial pole;
    - X-axis: towards the mean vernal equinoctial;
    - Y-axis: completes a right-handed system.
- Earth-Fixed Frame (e-frame)
    - Origin: at the centre of mass of the Earth;
    - Z-axis: parallels to the mean spin axis of the Earth;
    - X-axis: towards the mean Greenwich meridian in the equinoctial plane;
    - Y-axis: completes a right-handed system.

- Body frame (b-frame)
    - Origin: at the center of accelerometer proof masses. Assumed to be identical with center of rotation of rotated sensor unit;
    - Y-axis: pointing forward;
    - X-axis: pointing to the right handed side when looking forward;
    - Z-axis: pointing upward and completing a right-handed system.
- Local-Level Frame (l-frame)
    - Origin: at the center of the b-frame;
    - Z-axis: pointing outward along the ellipsoidal normal;
    - Y-axis: towards the ellipsoidal north;
    - X-axis: towards the ellipsoidal east.

3. LIST OF SYMBOLS

A	Azimuth
$\mathbf{a}$	Acceleration Vector
a	Wavelet Scaling Parameter
B	Bias Instability Coefficient
b	Wavelet Translation Parameter
$\mathbf{b}_f$	Vector of Accelerometer Bias
$\mathbf{b}_\omega$	Vector of Gyro Bias
$\mathbf{F}$	Newtonian Force Vectot
$\mathbf{f}$	Vector of True Specific Force
f_0	Cut-off Frequency

g	Acceleration Unit/Universal Constant
H	Kalman Filter Design Matrix
H	System Transfer Function
I	Identity Matrix
$\mathbf{I}_f$	Vector of Accelerometer Measurement
$\mathbf{I}\omega$	Vector of Gyro Measurement
K	Rate Random Walk Coefficient
$\mathbf{K}_k$	Kalman Gain Matrix
$K(\tau)$	Covariance of Random Process
$\mathbf{l}_v$	Unit Vector
M	Mass
N	Non-orthogonal Matrix of Gyro Triad
N	Total Number of Data Points
n	Number of Data Points Contained in the Cluster
P	Kalman Filter Error States Covariance Matrix
P, Q, R	Vehicular angular rates
Q	Kalman Filter Covariance Matrix of Input Noise
Q	Random Walk Coefficient
Q_Z	Quantization Noise Coefficient
q_c	Exponentially Correlated (Markov) Noise Coefficient
R	Kalman Filter Covariance Matrix of Measurement Noise
R	Drift Rate Ramp Coefficient

R_x	Autocorrelation Function
$\mathbf{S}$	Gyro Scale Factor in Matrix Form
$\mathbf{S}_1$	Accelerometer Linear Scale Factor in Matrix Form
$\mathbf{S}_2$	Accelerometer Non-linear Scale Factor in Matrix Form
S_E	Estimated Scale Factor
S_{input}	Input Power Spectral Density
S_{output}	Output Power Spectral Density
S_T	True Scale Factor
S_Ω	Power Spectral Density of the Random Process
$S^1(f)$	Single Sided Power Spectral Density
$S(\omega)$	Two Sided Power Spectral Density of Random Process
T	Cluster Length
Ta	Alignment Time
T_c	Exponentially Correlated (Markov) Noise Correlation Time
t_0	Sample time
$\mathbf{V}$	Inertial Velocity Vector
$X_{a,b}$	Continuous Wavelet Transform
x_{ev}	Even Elements of the Sequence of x(n)
x_{od}	Odd Elements of the Sequence of x(n)
x()	Measurement Data Sequence
Φ,Θ,Ψ	Euler Angles
W	Angular Velocity Vetor

Ω_0	Sinusoidal Noise Amplitude
$\overline{\Omega}_k$	Cluster Average
$\overline{\Omega}_{next}$	Subsequent Cluster Average
$\Omega(t)$	Instantaneous Output Rate of Inertial Sensor
α	Unknown Parameter
β	Inverse Correlation Time
δA	Azimuth Error
$\delta \mathbf{g}$	Anomalous Gravity Vector
δ_{AV}	Fractional Error
$\delta(x)$	Dirac Delta Function
ε	Noise
ϕ	Latitude
σ	Standard Deviation
$\sigma(\delta_{AV})$	Percentage Error
σ^2	Variance
τ	Correlation Time
ω	Vector of True Angular Velocity
ω_e	Earth Rotation Rate
ξ	Cluster Difference
$\psi_{m,n}$	Discrete Wavelet Family Function
$<>$	Averaging Operation
$\underline{\Delta}$	Denotes

CHAPTER ONE: INTRODUCTION

Navigation is a very ancient skill or art, which has become a complex science. It is essentially about travel and finding the way from one place to another and there are a variety of means by which this may be achieved (Titterton and Weston 1997).

The navigator may choose to observe objects or naturally occurring phenomena to determine his/her position. An ancient and well-established technique is to take sightings of certain fixed stars to which the navigator can relate his/her position. The fixed stars effectively define a reference frame, which is fixed in space. Such a reference is commonly referred to as an *inertial reference frame* and star sightings enable an observer to determine his/her position with respect to that frame. Given the knowledge of motion of the Earth and the time of the observation, the navigator is then able to use the celestial measurements to define his/her position on the surface of the Earth. Navigation systems of this type, which rely on observation of the outside world, are known as position fixed systems.

An alternative approach is to use the principle of *dead reckoning* by which one's present position may be calculated from the knowledge of one's initial position and speed and direction measurements. The process of dead reckoning is performed by taking the last known position and the time at which it was obtained, and noting the average speed and heading since that time to the current time. The speed must be resolved through the heading angle to provide the velocity components in the north and east directions. Each is

then multiplied by the time that has elapsed since the last position was obtained, thereby giving the change in position. Finally, the position changes are summed with the initial position to obtain the present position.

An equivalent process may be conducted using inertial sensors-gyroscopes and accelerometers-that sense rotational and translational motion with respect to an inertial reference frame. This is known as inertial navigation.

1.1 INERTIAL NAVIGATION SYSTEMS

The operation of an inertial navigation system (INS) depends on the laws of classical mechanics as formulated by Newton. Newton's First law states, *"An object at rest tends to stay at rest and an object in motion tends to stay in motion with the same speed and in the same direction unless acted upon by an unbalanced force*". Newton's Second law states, "*The acceleration of an object as produced by a net force is directly proportional to the magnitude of the net force, in the same direction as the net force, and inversely proportional to the mass of the object*". Given the ability to measure the moving body acceleration, it is possible to calculate the change in velocity and position by performing successive mathematical integrations of the acceleration with respect to time. Acceleration can be determined using an accelerometer. An inertial navigation system usually contains three accelerometers, which are commonly mounted with their sensitive axes perpendicular to one another. The working theory of accelerometer is based on the Newton's laws.

In order to navigate with respect to the inertial reference frame, it is necessary to keep track of the direction in which the accelerometers are pointing. Rotational motion of the body with respect to the inertial reference frame may be sensed using gyroscopic sensors and used to determine the orientation of the accelerometers at all times. Given this information, it is possible to transform the accelerations into the computation frame before the integration process takes place. At each time-step of the system's clock, the navigation computer time integrates this quantity to get the body's velocity vector. The velocity vector is then time integrated, yielding the position vector. These steps are continuously iterated throughout the navigation process (Verplaetse 1995). Figure 1.1 shows this concept in a schematic form. This procedure is, usually, considered as IMU mechanization. The mechanization results will be fed into the Kalman filter to correct inertial sensor errors for best estimation solution.

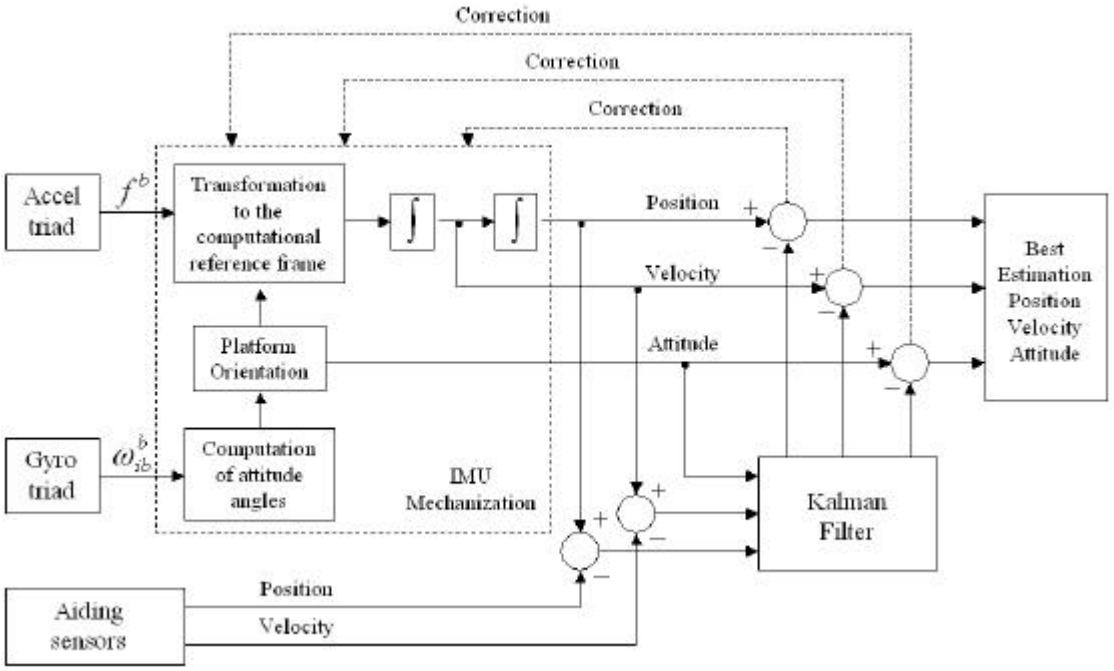

Figure 1.1 Inertial Navigation Schematic Plot (after El-Sheimy 2003)

Hence, inertial navigation is the process whereby the measurements provided by gyroscopes and accelerometers are used to determine the position of the vehicle in which they are installed. By combining the two sets of measurements, it is possible to define the translational motion of the vehicle within the inertial reference frame and to calculate its position within that frame.

1.2 BACKGROUND AND OBJECTIVE

The Inertial Measurement Unit (IMU) typically provides an output of the vehicle's (e.g. aircraft) acceleration and angular rate, which are then integrated to obtain the vehicle's position, velocity, and attitude. The IMU measurements are usually corrupted by different types of error sources such as sensor noises, scale factor and bias variations with temperature (nonlinear, difficult to characterize), etc. By integrating the IMU measurements in the navigation algorithm, these errors will be accumulated, leading to significant drift in the position and velocity outputs. A stand-alone IMU by itself is seldom useful since the inertial sensor biases and the fixed-step integration errors will cause the navigation solution to diverge quickly. Inertial systems design and performance prediction depend on the accurate knowledge of the sensors' noise model. The requirements for accurate estimation of navigation information necessitate the modeling of the sensors noise components.

Several methods have been devised for the stochastic modeling of the sensors' noise. The frequency domain approach, which uses the power spectral density (PSD) to estimate transfer functions is straightforward but difficult for non-system analysts to understand.

The correlation function approach is the time-domain equivalent of the PSD approach, being related as Fourier transforms pairs. This is analogous to expressing the frequency response function in terms of partial fraction expansion. The correlation method is very model sensitive and not well suited to dealing with odd power law processes, higher order processes or wide dynamic ranges. They work best with a priori knowledge based on a model of few terms (IEEE Std 952-1977).

For the variance techniques, they are basically very similar, and primarily differ only in that various signal processing, by way of weighting functions, window functions, etc., are incorporated into the analysis algorithms in order to achieve a particular desired result for improving the model characterizations. The simplest is the Allan variance.

Allan variance is a method of representing root mean square (RMS) random drift error as a function of averaging time (IEEE Std 952-1977). It is simple to compute and relatively simple to interpret and understand. The Allan variance method can be used to determine the characteristics of the underlying random processes that give rise to the data noise. This technique can be used to characterize various types of noise terms in the inertial sensor data by performing certain operations on the entire length of data.

Although the Allan variance statistic remains useful for revealing broad spectral trends, Allan variance does not always determine a unique noise spectrum cause the mapping from spectrum to Allan variance is not one-to-one (Greenhall 1998). This puts a

fundamental limitation on what can be learned about a noise process from examination of its Allan variance.

The main objective of this thesis is to investigate, implement, and test the Allan variance as a unified method in identifying and modeling noise terms of different grade IMU sensors. In order to improve the performance of the inertial sensors, both the manufacturers and the users are keen to know more detail about the noise component. Once the noise terms are revealed, the manufacturers can find a way to remove or minimize the sources causing the noise, during the manufacture process. Complementary to this is that the users can have a better modeling of the stochastic part to improve the navigation solution. The major success of this thesis is that it proves that Allan variance method can be used to investigate all potential noise terms for different levels of inertial sensors. Comparing with other methods, such as autocorrelation and power spectral density, Allan variance is much easier to implement and understand. Thus this method can be widely used in inertial sensor stochastic modeling.

Under the overall objectives, the following tasks have been addressed:

- Investigate the methodology of Allan variance,
- Distinguish the noise terms obtained from the Allan variance method,
- Implement the Allan variance in a software for IMU sensors noise analysis,
- Implement short and long term static tests with IMU sensors,
- Investigate and model noise terms in different grade IMU sensors.

1.3 THESIS OUTLINE

In Chapter Two, the operation principle of both gyro and accelerometer are first introduced as well as the technologies that dominate the current market. Then the major error sources, which will affect the inertial sensor performance, are discussed. Different methodologies that can be used to eliminate or minimize these errors are finally presented.

In Chapter Three, the algorithm of discrete Kalman filter is introduced followed by the general stochastic modeling methods, such as the autocorrelation method, power spectral density method, variance method, and adaptive Kalman filter method. In addition, the useful techniques in stochastic modeling including the fast Fourier transform and wavelet de-nosing method are reviewed.

The definition and properties of Allan variance are given in Chapter Four. The procedure for the analysis and modeling of different noise terms are discussed. The method used to evaluate the analysis results is given.

In Chapter Five, the results of testing different types of IMU are presented. The tested systems include:

- Navigation grade IMU: The Honeywell CIMU;
- Tactical grade IMU: The Honeywell HG1700; and
- Consumer grade MEMS based IMU: The Systron Donner MotionPak II-3g

Finally, Chapter Six draws the major conclusions from this research work and provides recommendations for future work.

Some of the material presented in Chapter Four and Five has been previously published in papers. In those cases where the author has been an author or co-author of these papers, quotations are not indicated as such, but are simply referenced.

CHAPTER TWO: INERTIAL SENSORS AND THEIR ERROR SOURCES

The operation principles as well as the technologies used in the current market of both gyro and accelerometer are introduced in this chapter. Then the major error sources of inertial sensors are discussed. Finally, the general methods used to eliminate or minimize these errors are presented.

2.1 INERTIAL NAVIGATION PRINCIPLE

The objective of modeling motion in space is to describe the motion of objects on the earth's surface or close to it. These objects are affected by the earth's gravitational attraction due to the Earth's gravity field and rotation. The general motion of a rigid body in space can be described by six parameters. They are typically identified as three position and three orientation parameters. Determining the position and orientation of the rigid body in 3D space is, in principle, a problem of trajectory determination. This necessitates measuring systems with the capability to sense six independent quantities from which these parameters can be derived. The motion of any point of a rigid body in space can be described as the sum of two vectors: the position vector of the center of mass of the body with respect to the earth fixed coordinate frame and the vector between the center of mass and another point on the body (El-Sheimy 1996).

Position, velocity and attitude, when presented as a time variable function, are called navigation states because they contain all necessary navigation information to georeference a moving object at a specific moment of time (El-Sheimy 2003). A

combination of sensors capable of determining all navigation states makes up a navigation system. Obviously, different sensors can be used to determine the same subvector of the navigation states, such as position state or attitude state. Navigation comprises the methods and technologies to determine the time varying position and attitude of a moving object by measurement.

An equivalent process may be conducted using inertial sensors-gyroscopes and accelerometers, which are the two categories of inertial sensor -to sense rotational and translational motion with respect to an inertial reference frame. In order to navigate with respect to the inertial reference frame, it is necessary to keep track of the direction in which the accelerometers are pointing. Rotational motion of the body with respect to the inertial reference frame may be sensed using gyroscopic sensors and used to determine the orientation of the accelerometers at all times. Given this information, it is possible to resolve the accelerations into the reference frame before the integration process takes place. Double integration of the accelerations provides the position according to the inertial reference frame. This is known as inertial navigation.

The principle of inertial navigation is based on Newton's first law of motion: *every body continues in its state of rest or uniform motion in straight line, unless it is compelled to change that state by forces imposed on it*. The full meaning of Newton's first law is not easily visualized in the Earth's reference frame. To apply Newton's laws, the body must be in an inertial reference frame (non-rotating frame in which there are no inherent forces, such as gravity). Newton's second law of motion, *acceleration is proportional to*

the resultant force and is in the same direction as this force, shares importance with his first law in inertial navigation. The physical quantity in which inertial navigation system is interested is acceleration since velocity and displacement can be derived from acceleration by integration. An inertial navigation system is an integrated system consisting of a detector and an integrator. It first detects acceleration and then integrates it to derive the velocity. Then integrates velocity to derive the displacement (Schwarz and El-Sheimy, 1999).

Measuring the vehicle acceleration in an inertial frame of reference and transforming it to the navigation frame and integrating it with respect to time, velocity, attitude and position differences in the navigation frame can be obtained. In this mode of operation, an Inertial Navigation System (INS) can be considered as a highly sophisticated dead-reckoning system.

2.2 INERTIAL SENSORS

Many types of inertial instruments have been invented in the past, are currently being invented, and will continue to be invented as the market for guidance, navigation, and control continues to expand. Based on the technologies used, which decide the size, cost, and performance, some of the inertial instruments have found a niche in current applications, while some did not progress much beyond the laboratory/prototype stage. This will be true to the future development of inertial sensors (Barbour et al. 1992).

2.2.1 INERTIAL ROTATION SENSORS

In this section some of the most important gyroscopic rotation sensors that have been in use will be discussed.

2.2.1.1 PRINCIPLE OF OPERATION

The typical quantities to be measured by inertial rotation sensors are the vehicle attitude Euler angles Φ, Θ, and Ψ, which are defined with respect to the local level frame and the inertial vehicular angular rates P, Q, R. These quantities are depicted in Figure (2.1). The transformation of any vector from the Earth's axes X_e, Y_e, Z_e to the INS body axes x_b, y_b, z_b is performed by the Euler transformation $[E]=[\Phi][\Theta][\Psi]$, formulated in detail in (Merhav 1996).

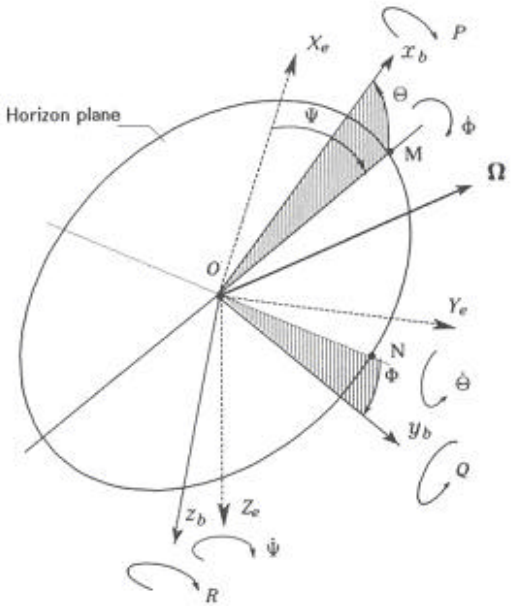

Figure 2.1 Rotation of body axes and Earth axes (after Merhav 1996).

It is important to realize that the inertial angular rates P, Q, R are not identical to the Euler angular rates $\dot{\Phi}, \dot{\Theta}, \dot{\Psi}$. The former triplet represents the projections of the total inertial angular rate vector Ω on the vehicle body axes x_b, y_b, z_b while the latter triplet represents the Euler angular rates $\dot{\Phi}, \dot{\Theta}, \dot{\Psi}$ around the axes OM, ON and Z_e respectively. The kinematic relationships between P, Q, R and $\dot{\Phi}, \dot{\Theta}, \dot{\Psi}$ are known as the Euler differential equations presented in, among others, McRuer et al. (1973), Blakelock (1991) and El-Sheimy (2003). They are repeated here for the sake of completeness.

$$P = \dot{\Phi} - \dot{\Psi} \sin \Theta \tag{2.1}$$

$$Q = \dot{\Theta} \cos \Phi - \dot{\Psi} \cos \Theta \sin \dot{\Phi} \tag{2.2}$$

$$R = -\dot{\Theta} \sin \Phi + \dot{\Psi} \cos \Theta \cos \Phi \tag{2.3}$$

Alternatively, solving for $\dot{\Phi}, \dot{\Theta}, \dot{\Psi}$ in terms of P, Q, R yields

$$\dot{\Phi} = P + Q \sin \Phi \tan \Theta + R \cos \Phi \tan \Theta \tag{2.4}$$

$$\dot{\Theta} = Q \cos \Phi - R \sin \Phi \tag{2.5}$$

$$\dot{\Psi} = Q \frac{\sin \Phi}{\cos \Theta} + R \frac{\cos \Phi}{\cos \Theta} \tag{2.6}$$

Equations (2.4) to (2.6) are of particular important technique because they permit the computation of the Euler angles Φ, Θ, Ψ given their initial value Φ_0, Θ_0, Ψ_0 by alignment and using the measurements P, Q, R provided by the triad of rate gyros.

$$\Theta = \Theta_0 + \int_0^t \dot{\Theta} dt \tag{2.7}$$

$$\Phi = \Phi_0 + \int_0^t \dot{\Phi} dt \tag{2.8}$$

$$\Psi = \Psi_0 + \int_0^t \dot{\Psi} dt \tag{2.9}$$

Thus, the Euler angles can be derived simultaneously from the measured inertial angular rate components *P, Q, R* and the computational algorithm based on Equation (2.4) to (2.9). However, the measured angular rates *P, Q, R* invariably incorporate errors known as drift rates. Therefore, the integrations of Equation (2.7) to (2.9) will accumulate these errors, which will cause the angular output diverge with time. For this reason, the method based on the integration of the Euler equations is applicable only in either high-precision and costly inertial guidance technology or in very short-term guidance applications (Merhav 1996).

2.2.1.2 CATEGORY AND APPLICATIONS

This section begins by describing the different gyroscope technologies that dominate the current market and explains, in terms of performance and technology being used, why they have been successful. Since accuracy requirements can be attained by existing technologies, the competition is driven by the desire for low cost, small size, and low production cost (Barbour et al. 1992).

The spinning mass gyroscope first found a home around 1920 in the single-degree-of-freedom rate gyro used as a basic turn indicator for instrument flying (Smith and Meyraugh 1990). After continuous evolution and improvement it was later used to

provide lead angle data for aircraft fire control sights, and later still for aircraft and missile flight control systems. The basic configuration of a rate gyro is a ball bearing rotor housed in a gimbal whose gyroscopic precession in response to an angular rate is restrained by a mechanical spring, making it relatively inexpensive, very rugged, and reliable. Rate gyros dominate the 10 deg/h gyro drift rate and applications such as flight control, stability augmentation, autopilots, etc (Barbour et al. 1992).

With the need for better performance, such as in aircraft navigation, it was logical to improve the rate gyro. When it was identified that the rate gyro's performance was limited by its spring (Smith and Meyraugh 1990) (i.e., the very mechanism that allows it to function also limits its capability), the performance requirements were mastered by the development of the single-degree-of-freedom, rate-integrating gyroscopes. The integrating gyro is basically a rate gyro in which the primary restraining torque on the gyro gimbal is a damping reaction with a servo loop to maintain the gimbal at null. The floated integrating gyro progressed from revolutionizing aircraft navigation in the 50s to enabling strategic missile guidance, autonomous submarine navigation, and space flight in the 60s, 70s and 80s (Smith and Meyraugh 1990).

The gas bearing was a significant part of the floated gyro evolution, leading to better stability, and a self-aligning capability for strategic missiles, a capability that no other instrument to date provides (Barbour et al. 1992). Another benefit of the gas bearing is the reduction of the angle noise of the floated instrument, so that it is used in satellite

navigation and control; its most recent application is in the Hubble telescope (Barbour et al. 1992).

Floated integrating gyros have a relatively high cost, are labor intensive, and have long warm-up (reaction) times (Barbour et al. 1992). Clearly, if a suitable alternate technology could be found, it would take advantage of these perceived problems -- and this is exactly what happened.

The free rotor gyroscope, which is basically a ball bearing rotated spinning mass that is unrestrained about the gyroscope precession axes, was another early development (Smith and Meyraugh 1990). The use of one or two gimbals allows these instruments to be used as directional gyros for directional references and cockpit displays such as the gyrocompass, artificial horizon, etc. These are very low-accuracy instrument, but they have maintained their role in the market place (Smith and Meyraugh 1990).

Another early instrument that offered potential advantages over the floated gyro was the two-degree-of-freedom, gas-film supported, free rotor gyroscopes. However, it was not until the mid-50s that this instrument became viable when the rotor time constant problem was solved (Smith and Meyraugh 1990). This type of instrument has fast reaction times and results in lower costs because of its two degrees of freedom, but it cannot match the best performing floated gyros.

The free rotor gyro can be regarded as a precursor to the two-degree-of-freedom electrostatic gyro (ESG). The ESG only became viable when machining techniques became available to generate the very precise finishes and geometry required. The ESG has much lower drift than the best floated gyros and is small; unfortunately, its applications are limited to relatively benign environments since it has low g capability (Barbour et al. 1992). ESGs are being replaced by lower cost technologies that are better suited for strapdown applications.

In the early 60s, the dynamically tuned free rotor gyroscope (DTG) was invented (Smith and Meyraugh 1990). The DTG is a two-degree-of-freedom instrument whose rotor is suspended by a universal hinge of zero stiffness at the turned speed and rotated by a ball bearing. Because of their relatively low cost, fast reaction time, small size and ruggedness, DTGs have dominated the market compared to other mechanical instruments in most areas where performance is comparable (Barbour et al. 1992).

At the same time that the DTG was being invented, the principle of detecting rotation by the Sagnac effect was first demonstrated (1963) in a ring laser gyroscope (RLG). The RLG operates by setting up clockwise and count clockwise resonant light beams reflected around a closed cavity by mirrors and detecting phase shifts between these beams due to a rotation. The laser is inside the cavity, which contains the lasing medium; hence, the RLG is termed an active device (Barbour et al. 1992). The RLG is an excellent strapdown device because of good scale-factor (SF) linearity and SF stability in the tens of parts per billion compared with tens of parts per million for mechanical sensors, and almost

negligible g sensitivity (Merhav 1996). The RLG has other attractive features such as digital output, very fast reaction times, excellent dormancy characteristics, lower cost, and the absence of moving parts. RLG technology is still advancing, but is at the practical limit for today's technology (Barbour et al. 1992).

The fiber-optic gyroscope (FOG) is implemented using an integrated optics chip constructed in lithium niobate, and fiber-optic sensing coil, diode light source, and photo-detectors (Smith and Meyraugh 1990). This configuration is expected to be supplemented eventually by quantum well technology, such as gallium arsenide, which will then allow integration of most of the above components into a single substrate, increasing reliability, and reducing costs even further (Smith and Meyraugh 1990). The most recent emerging technology is the interferometric fiber-optic gyro (IFOG). It provides the closed optical path by a multi-turn optical fiber coil wound on a coil. It is more compact and potentially of lower cost than the RLG (Smith and Meyraugh 1990).

The growing need for highly rugged miniature angular rate sensors has initiated a number of studies and prototype product development programs. These products are potentially suitable for medium to low accuracy applications. One principle approach is the Coriolis angular rate sensor. The underlying idea is to put an accelerometer in motion that is relative to the rotating vehicle body. The development of the basic concept is given in Merhav (1982), where the realization and analysis are provided, particularly, for rotating accelerometers. An alternative mechanization is through vibrating accelerometers, and is also presented in Merhav (1982). The leading idea is that these accelerometers are

potentially much cheaper, smaller, and more rugged than gyroscopic devices. Micromechanical gyroscopes are primarily Coriolis force sensors.

2.2.2 INERTIAL FORCE SENSORS – ACCELEROMETERS

This section introduces specific force sensors, or, as traditionally known in the technical literature, accelerometers. They range from traditional spring-mass devices to modern vibrating beam quartz or silicon technologies.

2.2.2.1 PRINCIPLE OF OPERATION

A fundamental requirement in navigation system design and operation is the measurement of vehicular acceleration with respect to inertial space. Sensors commonly known as accelerometers provide these measurements. Often they are called force sensor or specific force sensors (SFS). Specific force, denoted by the vector **a**, implies the total Newtonian force **F** acting on the vehicle divided by its mass **M**, i.e.

$$\mathbf{a} = \frac{\mathbf{F}}{\mathbf{M}} \; m/s^2 \tag{2.10}$$

a is commonly resolved along the body-axes of the vehicle *x, y*, and *z*, so that $\mathbf{a} \underline{\Delta} [a_x, a_y, a_z]^T$, where *T* denotes the transpose. Since SFS's are single input-axis devices, each axis requires the dedication of at least one SFS.

The term SFS is used because this sensor does not actually measure acceleration. This is best verified by considering a vehicle in free fall equipped with an SFS. While the vehicle

clearly accelerates at g = 9.8 m/s^2, the SFS reading is zero. The reason, of course, is that the gravitational pull acts equally on each mass particle of the SFS so that no relative displacement takes place between the proof mass m and the SFS casing (Merhav 1996). Specific force and acceleration are only identical in a gravitation-free environment that, strictly speaking, does not exist in our planetary system, or for that matter in the universe. Thus, in every situation, in order to establish the reading of an SFS, one has to identify inertial (Newtonian) forces only, disregarding gravitational forces or their projections caused by the tilting of the vehicle with respect to the local horizon (Merhav 1996).

2.2.2.2 SPECIFIC FORCE READING ON MOVING PLATFORMS

Consider the vehicle as a rigid body with a mass M, which moves with the inertial velocity $\mathbf{V}$ and angular velocity Ω. From Newton's second law,

$$\mathbf{F} = \frac{d}{dt}(\mathbf{M}\,\mathbf{V}) = \frac{dM}{dt}\mathbf{V} + \mathbf{M}\frac{d\mathbf{V}}{dt} \tag{2.11}$$

Assuming that M = const, so that the first term is zero. Thus, $\mathbf{F}$ is determined by the second term only, namely (Merhav 1996),

$$\mathbf{F} = M\frac{d\mathbf{V}}{dt} = \mathbf{l}_v M\frac{d\mathbf{V}}{dt} + M(\mathbf{\Omega}\times\mathbf{V}) \tag{2.12}$$

where $\mathbf{l}_v \underline{\Delta}(i, j, k)^T$ is the unit vector with its components i, j, k along the x, y, z body-axes. Dividing through by M, the acceleration vector is

$$\mathbf{a} = \mathbf{l}_v\frac{d\mathbf{V}}{dt} + \mathbf{\Omega}\times\mathbf{V} \tag{2.13}$$

The first term represents the tangential acceleration. The second term, often termed the Coriolis acceleration, is actually the centripetal acceleration resulting from the angular velocity W of the velocity vector **V** in the inertial space. Thus,

$$\mathbf{V} \triangleq iU + jV + kW \tag{2.14}$$

$$\mathbf{O} \triangleq iP + jQ + kR \tag{2.15}$$

With these notations, we have

$$\mathbf{l}_v \frac{d\mathbf{V}}{dt} = i\dot{U} + j\dot{V} + k\dot{W} \tag{2.16}$$

and

$$\mathbf{O} \times \mathbf{V} = \begin{vmatrix} i & j & k \\ P & Q & R \\ U & V & W \end{vmatrix} = i(QW - RV) + j(RU - PW) + k(PV - QU) \tag{2.17}$$

We denote

$$\mathbf{F} = iF_x + jF_y + kF_z \tag{2.18}$$

Combining Equation (2.12) with Equation (2.16) and (2.17) and dividing through by **M**, the Newtonian sensed reading $\mathbf{a}^n$ of the SFS's are

$$\begin{bmatrix} a_x^n \\ a_y^n \\ a_z^n \end{bmatrix} = \begin{bmatrix} \dot{U} + QW - RV \\ \dot{V} + RU - PW \\ \dot{W} + PV - QU \end{bmatrix} \tag{2.19}$$

They consist of the linear acceleration components and the components of centripetal acceleration due to the curved path of the vehicle. The earth is initially assumed to be flat and non-rotating (Merhav 1996).

A case of special interest, is a vehicle with the resultant net local vertical force $F_z + W = 0$, namely, $F_z = -W$, and one which determines the projections of the specific force $a_z = F_z/M = -g$ on the x, y, z body axes by means of the Euler transformation previously defined in Figure (2.1) (Merhav 1996):

$$\begin{bmatrix} a_x^g \\ a_y^g \\ a_z^g \end{bmatrix} = \begin{bmatrix} c\Psi c\Theta & s\Psi c\Theta & -s\Theta \\ (c\Psi s\Theta s\Phi - s\Psi c\Phi) & (s\Psi s\Theta s\Phi + c\Psi c\Phi) & c\Theta s\Phi \\ (c\Psi s\Theta c\Phi + s\Psi s\Phi) & (s\Psi s\Theta c\Phi - c\Psi s\Phi) & c\Theta c\Phi \end{bmatrix} \begin{bmatrix} 0 \\ 0 \\ -g \end{bmatrix} = \begin{bmatrix} gs\Theta \\ -gc\Theta s\Phi \\ -gc\Theta c\Phi \end{bmatrix} \qquad (2.20)$$

where $s(\bullet) \triangleq \sin(\bullet)$ and $c(\bullet) \triangleq \cos(\bullet)$.

Combining (2.19) and (2.20), the total specific force vector is expressed as (Merhav 1996).

$$\begin{bmatrix} a_x \\ a_y \\ a_z \end{bmatrix} = \begin{bmatrix} a_x^n \\ a_y^n \\ a_z^n \end{bmatrix} + \begin{bmatrix} a_x^g \\ a_y^g \\ a_z^g \end{bmatrix} = \begin{bmatrix} \dot{U} + QW - RV \\ \dot{V} + RU - PW \\ \dot{W} + PV - QU \end{bmatrix} + \begin{bmatrix} gs\Theta \\ -gc\Theta s\Phi \\ -gc\Theta c\Phi \end{bmatrix} \qquad (2.21)$$

It is important to realize that the readings of on-board SFS's are, in general, not identical to the vehicular acceleration as seen by an outside observer.

2.2.2.3 CATEGORY AND APPLICATIONS

New technologies continue to be developed to meet the SFS market needs. However, since accuracy requirements can be attained by existing technology, and since the new and emerging technologies offer little in any performance improvement, the decision to insert or develop them will depend on low life-cycle cost, small size, and low production cost (Barbour et al. 1992). While several of the new technologies are described herein, it is expected that only two or three will impact the market in a significant way.

The majority of electromechanical accelerometers are the restrained mass or force-rebalance types, in which a proof mass is supported in a plane perpendicular to the input (sense) axis by a flexure, torsion bar, or pivot and jewel (Norling 1990). The motion of this proof mass under changes of acceleration is detected by a pickoff. A rebalance force may be generated through a servo feedback loop to restore the proof mass to its null position. The force rebalance type of accelerometer has been successful not only because it is relatively small, simple, very rugged, and reliable, but also because it can be designed to meet different performance and application requirements by careful selection of the flexure and mass configuration, electromagnetic pickoffs and forces, servo electronics, fluid and damping, and materials (Savage 1978). Force rebalance accelerometers can operate in strapdown or gimbaled modes. The output needs to be digitized (Barbour et. al. 1992).

The highest performance accelerometer available is the Pendulous Integrating Gyro Accelerometer (PIGA), which is used for strategic missile guidance (Barbour et al. 1992). The PIG part of the PIGA is identical to the floated single-degree-freedom, integrating gyro with the addition of a pendulous mass located on the spin axis. The PIGA is a very stable, linear device, with very high resolution over a wide dynamic range. PIGAs are relatively complex and perceived to have high life-cycle costs due to the three rotating mechanisms (gas bearing, servo-driven member (SDM), and slip ring) (Barbour et al. 1992).

Another type of accelerometer is the resonator or open-loop type such as the vibrating string accelerometer. This device has low shock tolerance (Barbour et al. 1992).

Angular accelerometers were initially used in the 50s for dynamic compensation of AC (alternating current) servomechanisms. The basic configuration is a fluid-filled ring with a vane extending into it. Under rotational motion of the ring, the vane is restrained by a torquer, whose current indicates the angular displacement (Norling 1990). Such devices are used in applications requiring high bandwidth (2000Hz), small magnitude stabilization, or jitter compensation. However, angular displacement sensors are not as accurate as floated gyros or DTGs below about 20Hz, but the high cost of these gyros restricts their use (Barbour et al. 1992).

In less than 20 years, MEMS (micro electro-mechanical systems) technology has gone from an interesting academic exercise to an integral part of many common products (Weinberg 2004). Silicon micromechanical instruments can be made by bulk micromachining (chemical etching) single crystal silicon or by surface micromachining layers of polysilicon (Yun and Howe 1991). Many manufactures are developing gyros and accelerometers using this technology. Their extremely small size combined with the strength of silicon makes them ideal for very high acceleration applications. Silicon sensors provide many advantages over other materials, such as quartz or metal, for micro-sized rate sensor development. These advantages include excellent scale factor matching and stability, long life, bias stability, virtually no degradation, and the ability to handle larger stress levels (Yun and Howe 1991).

2.2.3 SUMMARY

An excellent survey on the state of the art of rotation and force sensors and their potential applications is provided in Barbour et al. (1992) along with the better-known mechanical and optical gyros. Figures (2.2) and (2.3) describe performance contours of current sensor technologies for gyros and accelerometers and their applications as related to ppm of scale factor (i.e., how well the gyroscope or accelerometer reproduces the sensed rate or acceleration) and μg or deg/h of inherent bias stability (i.e., the error independent of inertial rate or acceleration). While these performance factors are not the only ones that influence sensor selection, they are useful for comparison purposes. The closed contours are mapped in terms of bias and scale factor uncertainties. The various applications are indicated within these contours. Thus, one can see the association between current technologies and their operational utilization at a glance.

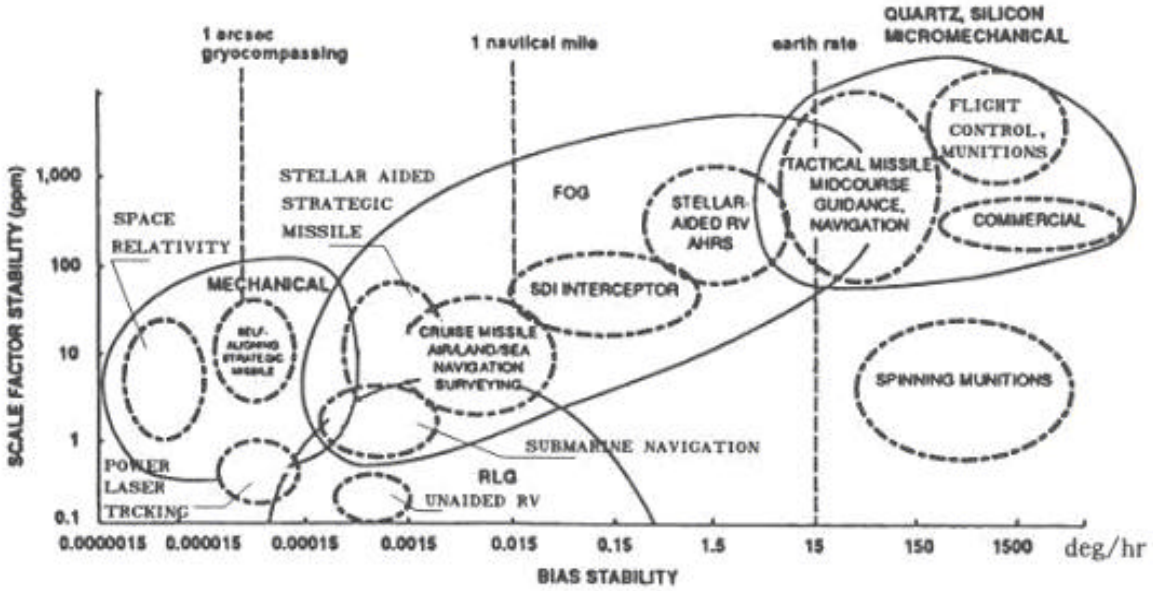

Figure 2.2 Current Gyro Technology Applications (After Merhav 1996)

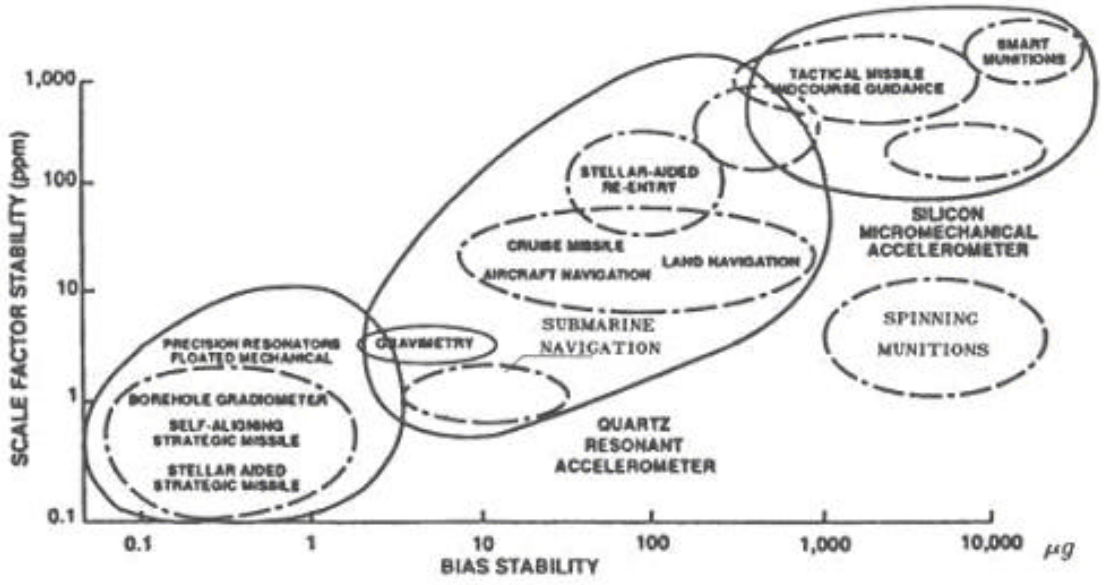

Figure 2.3 Current Accelerometer Technology Applications (After Merhav 1996)

The utilization of solid-state inertial sensors like those described above have potentially significant cost, size, and weight advantages over conventional instruments, which will result in a rethinking of the options for which such devices can be used in systems (Barbour et al. 1992). Micromechanical inertial sensors are currently dominating the low-performance end of the application spectrum. These instruments will continue to evolve into the middle-performance ground. The commercial market for micromechanical inertial sensors is orders of magnitude larger than any contemplated military market. The application of micromechanical gyro technology to the automobile industry is one case. Products designed for this industry must be inexpensive and reliable, both characteristics of solid-state technology. Many other micromechanical inertial sensor applications exist for automobiles such as airbags, braking, leveling, and augmentation to Global Positioning System (GPS) navigation systems. Additional commercial applications can

be found in products such as camcorders, factory automation, general aviation, medical electronics, and perhaps one of the largest areas of all, children's toys and games. If the cost can be brought down low enough, one could expect to see an IMU in every home (Barbour et al. 1992).

2.3 INERTIAL SENSOR ERRORS

The performance characteristics of inertial sensors (either gyroscopes or accelerometers) are affected by a variety of errors. Most errors can be categorised into sensor bias, scale factor, axes misalignment, and noise. In the following section, these errors will be discussed briefly.

2.3.1 BIAS

2.3.1.1 DEFINITION

The bias for gyro/accelerometer is the average over a specified time of accelerometer/gyro output measured at specified operating conditions that have no correlation with input acceleration or rotation. The gyro bias is typically expressed in degree per hour (°/h) or radian per second (rad/s) and the accelerometer bias is expressed in meter per second square [m/s^2 or g]. Bias generally consists of two parts: a deterministic part called bias offset and a random part. The bias offset, which refers to the offset in the measurement provided by the inertial sensor, is deterministic in nature and can be determined by calibration. The random part is called bias drift, which refers to the rate at which the error in an inertial sensor accumulates with time. The bias drift and the sensor output uncertainty are random in nature and they should be modeled as a

stochastic process. Bias errors can be reduced from the reference values, but the specific amount is range and type dependent (El-Sheimy 2003).

In addition to the above, there are another two characteristics used to describe the sensor bias. The first is the bias asymmetry (for gyro or accelerometer), which is the difference between the bias for positive and negative inputs, typically expressed in degree per hour (°/h) or meter per second square [m/s^2, g]. The second is the bias instability (for gyro or accelerometer), which is the random variation in the bias as computed over specified finite sample time and averaging time intervals. This non-stationary (evolutionary) process is characterized by a 1/f power spectral density. It is typically expressed in degree per hour (°/h) or meter per second square [m/s^2, g], respectively.

2.3.2 SCALE FACTOR

Scale factor is the ratio of a change in the input intended to be measured. Scale factor is generally evaluated as the slope of the straight line that can be fit by the method of least squares to input-output data. The scale factor error is deterministic in nature and can be determined by calibration. Scale factor asymmetry (for gyro or accelerometer) is the difference between the scale factor measured with positive input and that measured with negative input, specified as a fraction of the scale factor measured over the input range. Scale factor asymmetry implies that the slope of the input-output function is discontinuous at zero input. It must be distinguished from other nonlinearities (El-Sheimy 2003).

Scale factor stability, which is the capability of the inertial sensor to accurately sense angular velocity (or acceleration) at different angular rates (or at different accelerations), can also be used to describe scale factor. Scale factor stability is presumed to mean the variation of scale factor with temperature and its repeatability, which is expressed as part per million (ppm). Deviations from the theoretical scale are due to system imperfections.

2.3.3 MISALIGNMENT

Axes misalignment is the error resulting from the imperfection of mounting the sensors. It usually results in a non-orthogonality of the axes defining the INS body frame. As a result, each axis is affected by the measurements of the other two axes in the body frame. Axes misalignment can, in general, be compensated or modeled in the INS error equation (El-Sheimy 2003).

2.3.4 NOISE

Noise is an additional signal resulting from the sensor itself or other electronic equipment that interfere with the output signals trying to measure. Noise is in general non-systematic and therefore cannot be removed from the data using deterministic models. It can only be modeled by stochastic process.

2.3.5 SENSORS GENERAL MEASUREMENT MODEL

2.3.5.1 GYROS MEASUREMENT MODEL

Gyroscope is an angular rate sensor providing either angular rate in case of rate sensing type or attitude in the case of the rate integrating type. The following model represents most of the errors contained in a single gyroscope measurement of the angular rate:

$$\mathbf{?}_w = \mathbf{?} + \mathbf{b}_w + \mathbf{S?} + \mathbf{N?} + \mathbf{e}(w) \tag{2.22}$$

where $\boldsymbol{I}_?$ is the vector of measurements in (deg/hr), $\boldsymbol{?}$ is the vector of true angular velocities (the theoretically desired measurement) (deg/hr), $\boldsymbol{b}_?$ is the vector of gyroscope instrument bias (deg/hr), $\boldsymbol{S}$ is the gyro scale factor in matrix form, $\boldsymbol{N}$ is the matrix representing the non-orthogonality of the gyro triad and $\boldsymbol{e}(?)$ is the vector of the gyro sensor noise (deg/hr). These errors are, in principle, minimized by estimation techniques.

2.3.5.2 ACCELEROMETER MEASUREMENT ERRORS

The accelerometer error sources are quite similar to those of gyroscopes except for the scale factor, which contains two components (linear and non-linear). The following specific force model represents the errors contained in a single accelerometer measurement:

$$\mathbf{?}_f = \mathbf{f} + \mathbf{b}_f + \mathbf{S}_1\mathbf{f} + \mathbf{S}_2\mathbf{f} + \mathbf{Nf} + d\mathbf{g} + \mathbf{e}(f) \tag{2.23}$$

where $\boldsymbol{I}_\mathrm{f}$ is the vector of measurements in (m/s^2), $\boldsymbol{f}$ is the vector of true specific forces (m/s^2), $\boldsymbol{b}_\mathrm{f}$ is the vector of accelerometer instrument biases (m/s^2), $\boldsymbol{S}_1$ is the linear scale factor in matrix form, $\boldsymbol{S}_2$ is the non-linear scale factor in matrix form, $\boldsymbol{N}$ is the matrix representing the non-orthogonality, $d\boldsymbol{g}$ is the anomalous gravity vector (deviation from

the theoretical gravity value) (m/s^2) and $\boldsymbol{e}(f)$ is the vector representing the accelerometer sensor noise (m/s^2). These errors are, in principle, minimized by estimation techniques.

2.3.6 SENSOR ERRORS ELIMINATION / MINIMIZATION TECHNIQUES

In order to minimize the effect from bias and scale factor, the sensor errors elimination methods are necessary. The estimation and differencing are introduced only for the bias elimination process in accelerometer measurements; however, the principle for the gyro is the same. The calibration method is more generally used in inertial sensor bias and scale factor elimination.

2.3.6.1 ESTIMATION

The mathematical model of accelerometer measurement, if it can be perfectly aligned with gravity, can be simplified as:

$$I_f = f + b_f + e \tag{2.24}$$

where f, b_f, and e represent acceleration, bias and noise.

By aligning the accelerometer with the local gravity, the accelerometer measurement can be expressed as

$$I_f = -g + b_f + e \tag{2.25}$$

Then the bias can be estimated as

$$b_f = \left(I_f + g\right) + e \tag{2.26}$$

Clearly, the estimated value for the bias depends on the accuracy of estimating local gravity, *g*. Also, the noise component is assumed to be small. Repeating tests at the same point and averaging the measurement can improve the accuracy of estimation.

2.3.6.2 DIFFERENCING

If there are two known local gravity test points, by aligning the same accelerometer with each local gravity, the accelerometer measurement can be expressed as

$$I_{f_1} = -g_1 + b_f + e_1 \tag{2.27}$$

$$I_{f_2} = -g_2 + b_f + e_2 \tag{2.28}$$

Then the bias is eliminated by the measurement procedure:

$$I_{f_1} - I_{f_2} = (g_2 - g_1) + \Delta e \tag{2.29}$$

Here, the sensor axis is also assumed to align perfectly with the local gravity. Thus the measurement can be expressed as Equation (2.25).

2.3.6.3 CALIBRATION

Calibration is defined as the process of comparing instrument outputs with known reference information and determining coefficients that force the output to agree with the reference information over a range of output values. The calibration parameters to be determined can change according to the specific technology in an inertial measurement unit (IMU). The calibration usually takes place in a lab environment in which the inertial system is mounted on a level table with each sensitive axis pointing alternatively up and down (six positions). Therefore, it is possible to extract estimates of the accelerometer

bias and scale factor by summing and differencing combinations of the inertial system measurements.

$$I_{f_{up}} = b_f - (1+S)g \tag{2.30}$$

$$I_{f_{down}} = b_f + (1+S)g \tag{2.31}$$

where b_f, S, and g represent bias, scale factor and gravity, respectively. The bias and scale factor of the Z-axis accelerometer can be calculated from these measurements as

$$b_f = \left(I_{f_{up}} + I_{f_{down}}\right)/2 \tag{2.32}$$

$$S = \left(I_{f_{down}} - I_{f_{up}} - 2g\right)/2g \tag{2.33}$$

Similarly for the gyros, placing the sensor in static mode with the axis being calibrated pointing vertically upward and using the average of 10 to15 minutes' measurements,

$$I_{w_{up}} = b_w + (1+S_w)w_e \sin f \tag{2.34}$$

where b_ω, S_ω, f and w_e represent bias, scale factor, latitude of the gyro location and Earth's rotation rate, respectively. Rotate the sensor 180° such that the same axis is pointing vertically downward and get the average measurement,

$$I_{w_{down}} = b_w - (1+S_w)w_e \sin f \tag{2.35}$$

The bias and scale factor of the gyro under calibration can be calculated from these measurements as,

$$b_w = \left(I_{w_{up}} + I_{w_{down}}\right)/2 \tag{2.36}$$

$$S_w = \left(I_{w_{up}} - I_{w_{down}} - 2w_e \sin f\right)/(2w_e \sin f) \tag{2.37}$$

As described above, the noise is ignored during the calibration process. However, the value of the bias and scale factor is still contaminated by residual noise after calibration. As a result, further techniques are needed to estimate noise in navigation algorithm.

2.3.7 IMPACT OF SENSOR BIAS

An uncompensated accelerometer bias error will introduce an error proportional to time, *t*, in the velocity and an error proportional to t^2 in the position.

$$v = \int b_f dt = b_f t \Leftrightarrow p = \int v dt = \int b_f t dt = \frac{1}{2} b_f t^2 \tag{2.38}$$

From Equation (2.38), an accelerometer bias introduces first order errors in velocity and second order errors in the position. If there is a 100μg level accelerometer bias, the error in position after 10 seconds is 0.05m and that after 1000 seconds is 500m (assume g=10m/s^2).

An uncompensated gyro bias in the *X* or *Y* gyro error will introduce an angle (in roll or pitch) error proportional to time *t*,

$$dq = \int b_w dt = b_w t \tag{2.39}$$

This small angle will cause misalignment of the INS, and therefore the acceleration vector will be projected wrong. This, in turn, will introduce acceleration in one of the horizontal channels with a value $a = g \sin(dq) \approx g dq \approx g b_w t$ (Merhav 1996).

$$v = \int b_w g t dt = \frac{1}{2} b_w g t^2 \Leftrightarrow p = \int v dt = \int \frac{1}{2} b_w g t^2 dt = \frac{1}{6} b_w g t^3 \tag{2.40}$$

Therefore, a gyro bias introduces second order errors in velocity and third order errors in the position. If there is a 0.2 deg/h level axis gyro drift, the error in position due to gyro drift is 0.0016m after 10 seconds and 1600m after 1000seconds (assume g=10m/s^2). That means gyro drift is a significant error source. For more details about the effect of inertial sensor errors on the derived navigation quantities, it is advised to consult with El-Sheimy (2003).

2.3.8 IMPACT OF SCALE FACTOR

According to Equation (2.22), if only the scale factor error is considered, then

$$I_w = S_T w + S_E w \tag{2.41}$$

where S_T is the true scale facto and S_E is the scale factor error. Clearly, the scale factor error worked as a gyro bias, and the value is proportional to the angular rate. Based on the previous analysis, gyro drift is a significant error source and a gyro bias introduces second order errors in velocity and third order errors in the position.

Similarly, the effect of accelerometer scale factor error, according to Equation (2.23), can be expressed, if only linear scale factor is considered, as

$$I_f = S_T f_1 + S_E f_1 \tag{2.42}$$

Clearly, the scale factor error worked as an accelerometer bias, and the value is proportional to the acceleration. Based on the previous analysis, accelerometer bias introduces first order errors in velocity and second order errors in the position.

2.3.9 IMPACT OF INS MISALIGNMENT

Initial alignment includes two steps: accelerometer leveling and gyro compassing. Accelerometer leveling is aligning the z-axis of the accelerometer triad Z^b to the z-axis of the navigation frame by driving the output of the horizontal accelerometers to zero level surface. The assumption for a triad error-free accelerometers, with the accelerometers measurements f_x and f_y described the tilt in the x and y directions of the vertical accelerometer with respect to the vertical direction, results in:

$$f_x = g \sin q_x \rightarrow q_x = \sin^{-1}\left(f_x / g\right) \tag{2.43}$$

$$f_y = g \sin q_y \rightarrow q_y = \sin^{-1}\left(f_y / g\right) \tag{2.44}$$

where q_x and q_y are the tilt in the x and y directions respectively (usually called roll and pitch). This clearly indicates that the roll and pitch accuracy are dependent on the accelerometer accuracy, which is mainly governed by the accelerometer bias. For small roll and pitch angles, the accuracy of roll and pitch angles will be given by:

$$dq_x = b_{f_x} / g \tag{2.45}$$

$$dq_y = b_{f_y} / g \tag{2.46}$$

where b_{f_x} is the x-axis accelerometer bias and b_{f_y} is the y-axis accelerometer bias. By driving f_x and f_y to zero (mathematically in the case of a strapdown system or mechanically in the case of a gimballed system), the true vertical is established and therefore the x^b and y^b accelerometers are located in a level plane.

Gyro compassing makes use of the fact that the gyro with its sensitive axis in the horizontal plane (i.e. after accelerometer levelling) at an arbitrary point on the surface of

the Earth, will sense a component of the Earth rotation. This component will be at a maximum when the sensitive axis points North and zero when it points East (El-Sheimy 2003).

After accelerometer levelling has been established, that is x^b and y^b accelerometers are located in a level plane, the x^b and y^b accelerometers will be arbitrarily rotated with an angle, the azimuth (A), with respect to the east and north directions. The X-axis gyro measurement will be given by:

$$w_x^b = -w_e \cos f \sin A \tag{2.47}$$

The Y-axis gyro measurement will be given by:

$$w_y^b = -w_e \cos f \cos A \tag{2.48}$$

Therefore, the azimuth can be obtained through:

$$\tan A = -w_x^b / w_y^b \tag{2.49}$$

It should be noted that the latitude of the INS does not need to be known in order to accomplish gyro compassing.

Consider the case of small azimuth angles, e.g. A approaching zero, therefore $\sin A = A$ and $\cos A = 1$. Then the X and Y gyro measurements will be given by:

$$w_x^b = -w_e \cos f \sin A = -A w_e \cos f \tag{2.50}$$

$$w_y^b = -w_e \cos f \cos A = w_e \cos f \text{ (Independent with } A\text{)} \tag{2.51}$$

This means that the accuracy of the azimuth will mainly depend on the x-axis gyro accuracy, which is mainly governed by the gyro bias,

$$dA = \frac{b_{w_x^b}}{w_e \cos f} \tag{2.52}$$

In addition to the alignment errors produced by the gyro drift, errors in azimuth also arise as a result of gyro random noise (defined by the gyro angle random walk (ARW): the angular error build-up with time that is due to white noise in angular rate). Gyro noise gives rise to an RMS azimuth alignment error, which is inversely proportional to the square root of the alignment time (T_a) (El-Sheimy 2003),

$$dA = \frac{ARW}{w_e \cos f \sqrt{T_a}} \Rightarrow T_a = \left(\frac{ARW}{w_e \cos f \, dA} \right)^2 \tag{2.53}$$

This means that, for a given gyro ARW, we can achieve different azimuth accuracies with different alignment time.

2.3.10 SUMMARY

Based on the above discussion, the gyro and accelerometer sensor errors of a strapdown inertial navigation system can be divided into two parts: a constant (or deterministic) part and a stochastic (or random) part. The deterministic part includes bias and scale factor, which can be determined by calibration and therefore can be removed from the raw measurements. The random part includes, for example, bias drift, axis misalignment, and random noise. These errors can be modeled in stochastic model and included the Kalman filter state vector.

Table (2.1) summarizes the characteristics of different inertial sensors error sources as well as the procedures to remove or minimize them.

Table 2.1 Summary of Inertial Sensor Errors					
Errors	Characteristic		Procedures to Remove/Minimize		
	Deterministic	Random	Calibration	Compensation	Stochastic Modeling
Bias Offset	v		v		
Bias Drift		v			v
Scale Factor	v		v		
Misalignment	v	v		v	v
Noise		v			v

CHAPTER THREE: REVIEW OF STOCHASTIC MODELING TECHNIQUES

In this chapter, the algorithm of discrete Kalman filter is introduced. Then, the general stochastic modeling methods are reviewed and examples are provided. In addition, the useful techniques in stochastic modeling, such as fast Fourier transform and wavelet de-nosing method, are introduced.

3.1 INTRODUCTION

The general non-linear problem was posed by Norbert Wiener during the early 1940s (Wiener 1961): given the yet to be analyzed system, which he defined as a black box, Wiener identified and characterized the system in terms of bodies of known structures, or what he called white boxes.

Based on that concept, the solution to the linear problem uses various time and frequency domain techniques to find an operational equivalent of the black box, which may then be constructed by combining certain canonical forms of these white boxes. Although the model structure may be different from the true structure, the input-output properties are to be equivalent.

The foundation of modeling goes back to approximately 1800 with Gauss's method of least square estimation (Gelb 1974). Current methods of determining the steady-state input-output characteristics of a variety of devices are based on this approach.

By 1960, Kalman conceived a time domain approach to optimal recursive filter design (Kalman 1960 and Gelb 1974). By 1963, Signal Identification (Gelb 1974) and frequency domain Time Series Analysis (TSA) (Van Trees 1968 and Gelb 1974) methods were developed. In 1965 Tukey and Cooly published their famous paper on the fast Fourier transform (FFT) (Gelb 1974). In 1966 David Allan proposed a simple variance analysis method for the study of oscillator stability (Allan 1966). Parameter Identification methods were known by 1968 (Gelb 1974 and Brogan 1974). During the decades that followed, time domain and frequency domain characterization of sensors gained importance.

All these methods are important for modeling inertial sensor noise and the next few sections will review some of these important methods including the autocorrelation method and power spectral density method. In addition, examples are provided to show how they will be used in modeling inertial sensors errors.

3.2 THE DISCRETE KALMAN FILTER

In 1960, Kalman published his famous paper describing a recursive solution to the discrete data linear filtering problem (Kalman 1960). Since that time, due in large part to advances in digital computing; the Kalman filter has been the subject of extensive research and application, particularly in the area of autonomous or assisted navigation. A very “friendly” introduction to the general idea of the Kalman filter can be found in (Maybeck 1979), while a more complete introductory discussion can be found in (Sorenson 1970), which also contains some interesting historical narrative. More

extensive references include Gelb (1974), Brown (1983), Lewis (1986), Grewal (1993), and Welch and Bishop (2004).

The Kalman filter is a set of mathematical equations that provides an efficient computational (recursive) solution of the least-square method. The filter is very powerful in several aspects: it supports estimations of past, present, and even future states, and it can do that even when the precise nature of the modeled system is unknown (Welch and Bishop 2004). The following discussion is based mainly on Brown (1983) and Welch and Bishop (2004).

3.2.1 THE PROCESS TO BE ESTIMATED

The Kalman filter addresses the general problem of estimating the state $\mathbf{x} \in R^n$ of a discrete time controlled process that is governed by the linear stochastic difference equation (Welch and Bishop 2004).

$$\mathbf{x}_k = \mathbf{A}\mathbf{x}_{k-1} + \mathbf{B}\mathbf{u}_k + \mathbf{w}_{k-1} \tag{3.1}$$

with a measurement $\mathbf{z} \in R^m$ that is

$$\mathbf{z}_k = \mathbf{H}\mathbf{x}_k + \mathbf{v}_k \tag{3.2}$$

The random variables $\mathbf{w}_k$ and $\mathbf{v}_k$ represent the process and measurement noise, respectively. They are assumed to be independent (of each other), white, and with normal probability distributions

$$p(w) \sim N(0, Q) \tag{3.3}$$

$$p(v) \sim N(0, R) \tag{3.4}$$

In practice, the process noise covariance **Q** and measurement noise covariance **R** matrices might change with each time step or measurement, however, here we assume they are constant.

The $n \times n$ matrix **A** in the difference equation (3.1) relates the state at the previous time step k-1 to the state at the current step k, in the absence of either a driving function or process noise. Note that in practice **A** might change with each time step, but here we assume it is constant. The $n \times 1$ matrix **B** relates the optional control input $\mathbf{u} \in R^l$ to the state x. The $m \times n$ matrix **H** in the measurement equation (3.2) relates the state to the measurement z_k. In practice **H** might change with each time step or measurement, but here we assume it is constant.

3.2.2 THE COMPUTATIONAL ORIGINS OF KALMAN FILTER

Define $\hat{\mathbf{x}}_k^- \in R^n$ to be a priori state estimate at step k given knowledge of the process prior to step k, and $\hat{\mathbf{x}}_k \in R^n$ to be a posteriori state estimate at step k given measurement $\mathbf{z}_k$. Define the a priori and the a posteriori estimate errors as (Welch and Bishop 2004)

$$\mathbf{e}_k^- \equiv \mathbf{x}_k - \hat{\mathbf{x}}_k^- \tag{3.5}$$

$$\mathbf{e}_k \equiv \mathbf{x}_k - \hat{\mathbf{x}}_k \tag{3.6}$$

The a priori estimate error covariance is

$$\mathbf{P}_k^- = E[\mathbf{e}_k^- \mathbf{e}_k^{-T}] \tag{3.7}$$

and the a posteriori estimate error covariance is

$$\mathbf{P}_k = E[\mathbf{e}_k \mathbf{e}_k^T] \tag{3.8}$$

In deriving the equations for the Kalman filter, begin with the goal of finding an equation that computes an a posteriori state $\hat{\mathbf{x}}_k$ as a linear combination of an a priori estimate and a weighted difference between an actual measurement $\mathbf{z}_k$ and a measurement prediction $\mathbf{H}\hat{\mathbf{x}}_k^-$ as shown below in Equation (3.9) (Welch and Bishop 2004).

$$\hat{\mathbf{x}}_k = \hat{\mathbf{x}}_k^- + \mathbf{K}_k\left(\mathbf{z}_k - \mathbf{H}\hat{\mathbf{x}}_k^-\right) \tag{3.9}$$

The difference ($\mathbf{z}_k$ - $\mathbf{H}\hat{\mathbf{x}}_k^-$) in Equation (3.9) is called the measurement innovation, or the residual. The residual reflects the discrepancy between the predicted measurement $\mathbf{H}\hat{\mathbf{x}}_k^-$ and the actual measurement $\mathbf{z}_k$. A residual of zero means that the two are in complete agreement.

The $n \times m$ matrix $\mathbf{K}_k$ in Equation (3.9) is chosen to be the gain or blending factor that minimizes the a posteriori error covariance, Equation (3.8). This minimization can be accomplished by first substituting Equation (3.9) into the above definition for $\mathbf{e}_k$, substituting that into Equation (3.8), performing the indicated expectations. Then by taking the derivative of the trace of the result with respect to $\mathbf{K}_k$, setting that result equal to zero, and then the $\mathbf{K}_k$ can be determined. One form of the resulting $\mathbf{K}_k$ that minimizes Equation (3.8) is given by

$$\mathbf{K}_k = \mathbf{P}_k^- \mathbf{H}^T \left(\mathbf{H}\mathbf{P}_k^- \mathbf{H}^T + \mathbf{R}\right)^{-1} = \frac{\mathbf{P}_k^- \mathbf{H}^T}{\mathbf{H}\mathbf{P}_k^- \mathbf{H}^T + \mathbf{R}} \tag{3.10}$$

Looking at Equation (3.10), as the measurement error covariance $\mathbf{R}$ approaches zero, the gain $\mathbf{K}_k$ weights the residual more heavily. Specifically,

$$\lim_{R_k \to 0} \mathbf{K}_k = \mathbf{H}^{-1} \tag{3.11}$$

On the other hand, as the a priori estimate error covariance $\mathbf{P}_k^-$ approaches zero, the gain $\mathbf{K}_k$ weights the residual less heavily. Specifically,

$$\lim_{P_k^- \to 0} \mathbf{K}_k = 0 \tag{3.12}$$

Another way of thinking about the weighting by $\mathbf{K}_k$ is that as the measurement error covariance $\mathbf{R}$ approaches zero, the actual measurement $\mathbf{z}_k$ is trusted more and more, while the predicted measurement $\mathbf{H}\hat{\mathbf{x}}_k^-$ is trusted less and less. On the other hand, as the a priori estimate error covariance $\mathbf{P}_k^-$ approaches zero the actual measurement $\mathbf{z}_k$ is trusted less and less, while the predicted measurement $\mathbf{H}\hat{\mathbf{x}}_k^-$ is trusted more and more (Welch and Bishop 2004).

3.2.3 THE DISCRETE KALMAN FILTER ALGORITHM

The Kalman filter estimates a process by using a form of feedback control: the filter estimates the process state at some time and then obtains feedback in the form of (noisy) measurements. As such, the equations for the Kalman filter fall into two groups: time update equations and measurement update equations. The time update equations are responsible for projecting forward (in time) the current state and error covariance estimates to obtain the a priori estimates for the next time step. The measurement update equations are responsible for the feedback, i.e. for incorporating a new measurement into the a priori estimate to obtain an improved a posteriori estimate (Welch and Bishop 2004).

The time update equations can also be thought of as predictor equations, while the measurement update equations can be thought of as corrector equations. Indeed the final estimation algorithm resembles that of a predictor-corrector algorithm for solving numerical problems.

The specific equations for the time and measurement updates are presented below in Table (3.1) and Table (3.2).

Table 3.1 Discrete Kalman filter time update equations

$$\hat{\mathbf{x}}_k^- = \mathbf{A}\hat{\mathbf{x}}_{k-1} + \mathbf{B}\mathbf{u}_k \tag{3.13}$$

$$\mathbf{P}_k^- = \mathbf{A}\mathbf{P}_{k-1}\mathbf{A}^T + \mathbf{Q} \tag{3.14}$$

Again notice how the time update equations in Table (3.1) project the state and covariance estimates forward from time step k-1 to step k. **A** and **B** are from Equation (3.1), while **Q** is from Equation (3.3). Initial conditions for the filter are discussed in the earlier references.

Table 3.2 Discrete Kalman filter measurement update equations

$$\mathbf{K}_k = \mathbf{P}_k^-\mathbf{H}^T\left(\mathbf{H}\mathbf{P}_k^-\mathbf{H}^T + \mathbf{R}\right)^{-1} \tag{3.15}$$

$$\hat{\mathbf{x}}_k = \hat{\mathbf{x}}_k^- + \mathbf{K}_k\left(\mathbf{z}_k - \mathbf{H}\hat{\mathbf{x}}_k^-\right) \tag{3.16}$$

$$\mathbf{P}_k = \left(\mathbf{I} - \mathbf{K}_k\mathbf{H}\right)\mathbf{P}_k^- \tag{3.17}$$

The first task during the measurement update is to compute the Kalman gain, $\mathbf{K}_k$. Notice that the equation given here as Equation (3.15) is the same as Equation (3.10). The next

step is to actually measure the process to obtain z_k, and then to generate an a posteriori state estimated by incorporating the measurement as in Equation (3.16). Again Equation (3.16) is simply Equation (3.9) repeated here for completeness. The final step is to obtain an a posteriori error covariance estimate via Equation (3.17).

After each time and measurement update pair, the process is repeated with the previous a posteriori estimates used to project or predict the new a priori estimates. This recursive nature is one of the very appealing features of the Kalman filter—it makes practical implementations much more feasible than, for example, an implementation of a Wiener filter (Brown 1983), which is designed to operate on all of the data directly for each estimate. The Kalman filter instead recursively conditions the current estimate on all of the past measurements. Figure (3.1) below offers a complete picture of the operation of the filter (Welch and Bishop 2004).

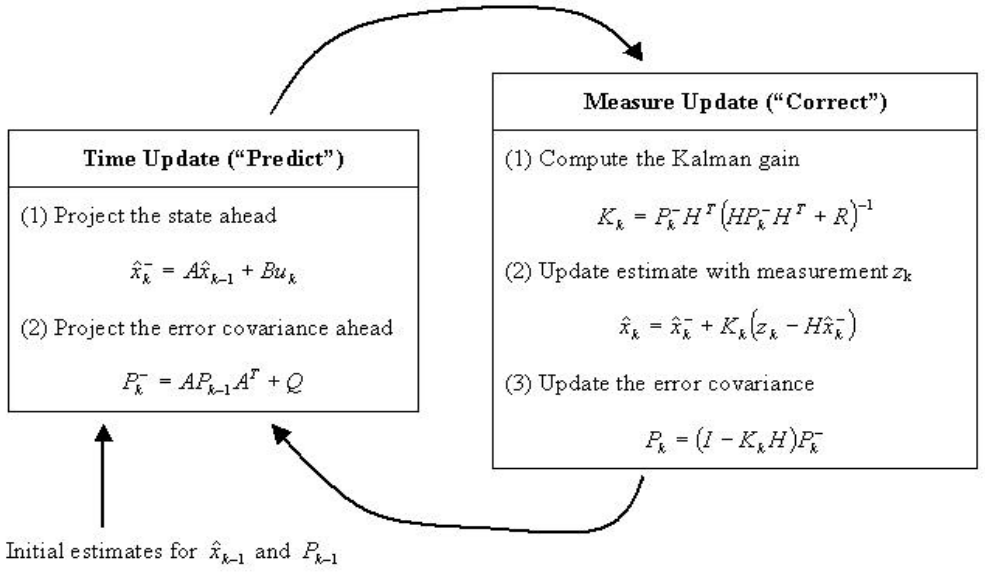

Figure 3.1 A complete picture of the operation of the Kalman filter (after Welch and Bishop 2004)

3.2.4 FILTER PARAMETERS AND TUNING

In the actual implementation of the filter, the measurement noise covariance **R** is usually measured prior to operation of the filter. Measuring the measurement error covariance **R** is generally practical (possible) because we need to be able to measure the process regardless (while operating the filter) thus we are generally able to take some off-time sample measurements in order to determine the variance of the measurement noise.

The determination of the process noise covariance **Q** is generally more difficult as we typically do not have the ability to directly observe the process we are estimating. Sometimes a relative simple (poor) process model can produce acceptable results if one "injects" enough uncertainty into the process via the selection of **Q**. Certainly in this case one would hope that the process measurements are reliable.

In either case, whether or not we have a rational basis for choosing the parameters, often times superior filter performance (statistically speaking) can be obtained by tuning the filter parameters **Q** and **R**. The tuning is usually performed off-line, frequently with the help of another (distinct) Kalman filter in a process generally referred to as system identification (Welch and Bishop 2004).

In closing we note that under conditions where **Q** and **R** are constant, both the estimation error covariance $\mathbf{P}_k$ and Kalman filter gain $\mathbf{K}_k$ will stabilize quickly and then remain

constant (see the filter update equations in Figure (3.1)). If this is the case, these parameters can be pre-computed by either running the filter off-line or, for example, by determining the steady-state value of $\mathbf{P}_k$ as described in Grewal (1993).

3.3 DIGITAL SIGNAL PROCESSING TOOLS

The subject of digital signal processing has received considerable attention in the past few decades, and this has occured concurrently with the advancement of computer technology (Brown 1983). In spectral analysis, Fourier transform is a powerful tool to identify or distinguish the different frequency sinusoids and their respective amplitudes (Brigham 1988). The fast Fourier transform is a discrete Fourier transform algorithm that reduces the number of computations needed. Wavelet analysis, in contrast to Fourier analysis, uses approximating functions that are localized in both time and frequency space. This unique characteristic makes wavelets particularly useful, for example, in approximating data with sharp discontinuities (Mallat 1989).

3.3.1 FAST FOURIER TRANSFORMS

In 1965 Cooly and Turkey described a computationally efficient algorithm for obtaining Fourier coefficients (Gelb 1974). The fast Fourier transform (FFT) is a method for computing the discrete Fourier transform (DFT) of a time series of discrete data samples. Such time series result when digital analysis techniques are used for analyzing a continuous waveform. It takes advantage of the fact that many computations are repeated in the DFT due to the periodic nature of the discrete Fourier kernel: $e^{-j2\pi kn/N}$. The form of the DFT is (Embree and Danieli 1999)

$$X(k) = \sum_{n=0}^{N-1} x(n) e^{-j 2\pi kn / N} \tag{3.18}$$

By letting $W^{nk} = e^{-j2\pi kn/N}$, Equation (3.18) is rewritten as

$$X(k) = \sum_{n=0}^{N-1} x(n) W^{nk} \tag{3.19}$$

Now, $W^{(n+qN)(k+rN)} = W^{nk}$ for all q, r, which are integers due to the periodicity of the Fourier kernel.

Break the DFT into two parts (Embree and Danieli 1999):

$$X(k) = \sum_{n=0}^{N/2-1} x(2n) W_N^{2nk} + \sum_{n=0}^{N/2-1} x(2n+1) W_N^{(2n+1)k} \tag{3.20}$$

Where the subscript N on the Fourier kernel represents the size of the sequence. If we represent the even elements of the sequence $x(n)$ by x_{ev} and the odd elements by x_{od}, then the equation can be rewritten

$$X(k) = \sum_{n=0}^{N/2-1} x_{ev} W_{N/2}^{nk} + W_{N/2}^{k} \sum_{n=0}^{N/2-1} x_{od} W_{N/2}^{nk} \tag{3.21}$$

We now have two expressions in the form of DFTs so we can write

$$X(k) = X_{ev}(n) + W_{N/2}^{k} X_{od}(n) \tag{3.22}$$

Notice that only DFTs of $N/2$ points need to be calculated to find the value of $X(k)$. Since the index k must go to N-1, however, the periodic property of the even and odd DFTs is used. In other words:

$$X_{ev}(k) = X_{ev}\left(k - \frac{N}{2}\right) \qquad for \frac{N}{2} \le k \le N-1 \tag{3.23}$$

For the original DFT, the number of multiplications required is of the order N^2. This can easily get out of hand, especially in "on-line" applications. Fortunately, in an FFT algorithm, the number of required multiplications is of the order of $N\log_2 N$. The computational saving is spectacular for large N. For example let N be 2^{10}=1024, which is a modest number of time samples for many applications (Brown 1983). Then N^2 would be about 10^6, whereas $N\log_2 N$ is only about 10^4. This represents a saving of about a factor of 100 and impacts directly on the time required for the transformation. Because of its efficiency, the FFT is used almost universally in both on-line and off-line spectral analysis applications (Brown 1983).

The FFT has applicability in the generation of statistical error models from series of test data. The algorithm can be modified to compute the autocorrelation function of a one-dimensional real sequence or the cross-correlation function and convolution of two one-dimensional real sequences. It can also be used to estimate the power spectral density of a one-dimensional real continuous waveform from a sequence of evenly spaced samples. The considerable efficiency of the FFT, relative to conventional analysis techniques, and the availability of the outputs from which statistical error models are readily obtained, suggest that the FFT will be of considerable utility in practical applications of linear system techniques.

Figures 3.2 and 3.3 show examples of FFT results for two hours static x-gyro data of the CIMU and the MotionPak II strapdown inertial systems. The first system is a navigation grade Ring Laser Gyro systems while the 2nd system is a tactical grade MEMS-based

system. The spectrum information can be obtained from the plots. The power at the zero frequency is much higher than the rest, so the y-axis value is limited to 4 to make the power spectrum clear. For static data, the high frequency info can be considered as noise. For CIMU gyro, the major noise gathers close to the range around 100Hz, which means that the noise part can easily be removed with a low pass filter. On the other hand, the noise for MotionPak II gyro distributes over almost all of the whole frequency ranges, which means that it is difficult to remove all the noise to obtain the true signal.

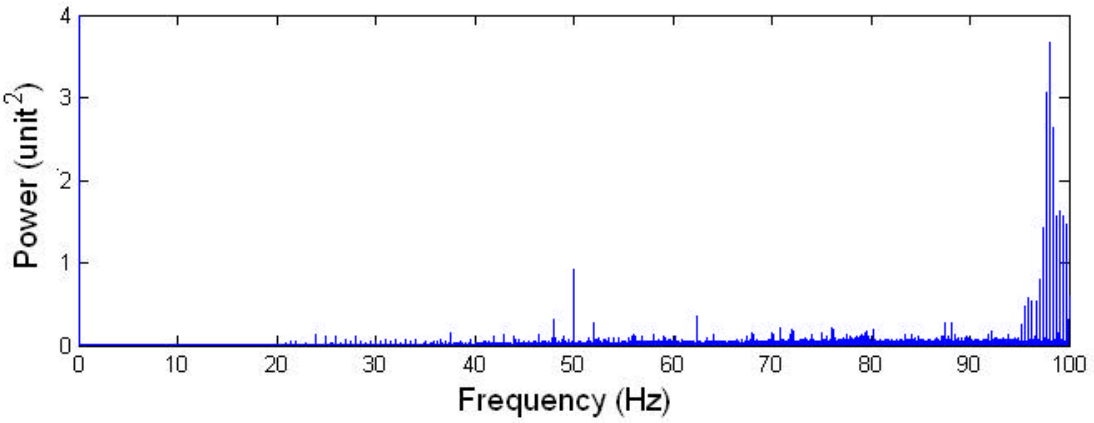

Figure 3.2 Two Hours CIMU X-axis Gyro FFT Result

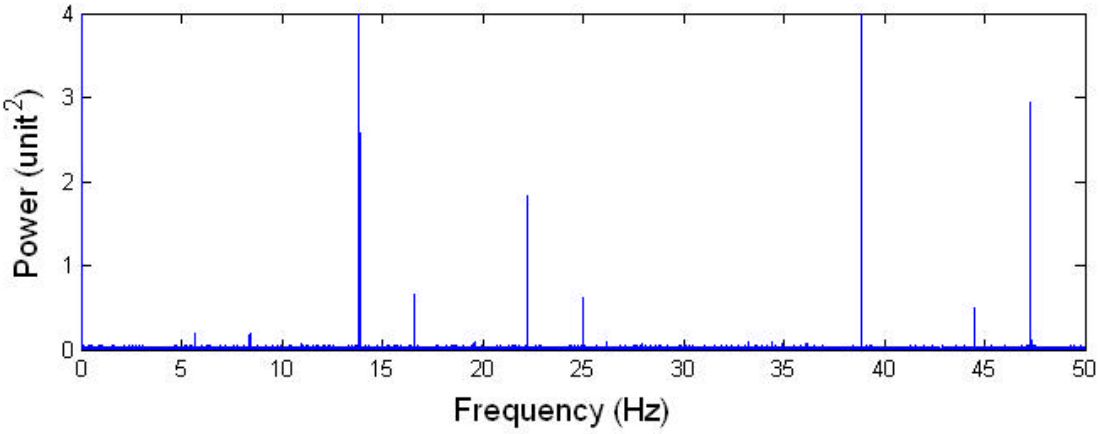

Figure 3.3 Two Hours MotionPak II X-axis Gyro FFT Result

3.3.2 WAVELET ANALYSIS

Wavelets, as a mathematical tool, have received extensive attention in the engineering profession during the last two decades. Wavelet analysis is a powerful method for decomposing and representing signals that has proven useful in a broad range of fields (Mallat 1989). Wavelet transforms are somewhat similar to Fourier transforms, in that they expose a function's frequency content. Fourier analysis begins with a waveform; a sequence of values indexed by time, and transforms this waveform into a sequence of coefficients, which are indexed by frequency. In a similar manner, wavelet techniques can also be used to analyze a time-indexed function and represent it as a group of frequency components. Wavelet techniques are based on analyzing a signal through signal windowing but with variable window size. This gives an advantage to wavelets over other signal processing techniques as it is capable of performing local analysis, i.e. analyzing a localized portion of a large signal (Nassar 2003). This is possible since wavelets allow the use of narrow windows (short time intervals) if high frequency information is needed and wide windows (long time intervals) if low frequency information is required.

The continuous wavelet transform (CWT), $X_{a,b}$, of a continuous-time domain signal $x(t)$ is defined as the inner product of $x(t)$ with a family of functions $y_{a,b}(t)$ as (Nassar 2003):

$$X_{a,b} = \langle x(t), y_{a,b}(t) \rangle \tag{3.24}$$

The family $y_{a,b}(t)$ is defined by continuous scaling (dilation or compression) parameters, a, and translation parameters, b, of a single analyzing function $y(t)$, which can be written as follows

$$y_{a,b} = \frac{1}{\sqrt{a}} y\left(\frac{t-b}{a}\right) \qquad a > 0 \tag{3.25}$$

Since we are dealing with discrete time signals, the Discrete Wavelet Transform (DWT) is implemented instead of the CWT. In this case, the basis functions are obtained by discretizing (sampling) the continuous parameters a and b. In the DWT, the sampling of a and b is based on powers of some constant number a, and the coefficient computations will be performed at specific scales and locations. Hence, the sampling of a and b in the DWT takes the form (Nassar 2003):

$$a = a^n \tag{3.26a}$$

$$b = ma^n \tag{3.26b}$$

where n and m are integer numbers representing the discrete dilation and translation indices. Moreover, from the practical aspects of the wavelet theory analysis, it has been found that the most efficient way of determining a and b is the "dyadic" one, i.e. to take the value of a to be 2 (Nassar 2003). Then the basis function is given by

$$y_{m,n}(t) = \frac{1}{\sqrt{2^n}} y\left(\frac{t}{2^n} - m\right) \tag{3.27}$$

For many signals, the low frequency component of the signal is the one of interest since it gives the signal its identity. On the other hand, the high frequency component usually constitutes the signal noise. In wavelet terminology, the low frequency component of a signal is called the "approximation part" while the high frequency component is called

the “detail part”. Therefore, to obtain finer resolution frequency components of a specific signal, the signal is broken down into many lower-resolution components by repeating the DWT decomposition procedure with successive decompositions of the obtained approximation parts. This procedure is called wavelet multi-resolution analysis.

In theory, the decomposition process can be continued indefinitely, but in reality it can be performed only until the individual details consist of a single sample. Practically, an appropriate Level of Decomposition (LOD) is chosen based on the nature of the signal or on a specific criterion (Misiti 2000).

For static inertial data, the sensor output contains the following signals: the Earth gravity components, the Earth rotation rate components and the sensors long-term errors (Nassar 2003). These signals have a very low frequency, and hence, they can be separated easily from the high frequency noise components by the wavelet multi-resolution analysis. To select an appropriate LOD in this case, several decomposition levels are applied and the raw data was decomposed into low and high frequency components. At each level, the mean of the high frequency component was computed as shown in Figure (3.4) and Figure (3.5) for CIMU and MotionPak II gyro data, respectively. Since noise is assumed to be zero mean, the wavelet decomposition level at which the mean becomes non-zero should be used for decomposition, since further decomposition would mean that actual trends in the data are being interpreted as noise (Lachapelle, et al. 2003). Therefore, the LOD for CIMU gyros is 15 for X and Z-axis and 18 for Y-axis while that for MotionPak II is 14.

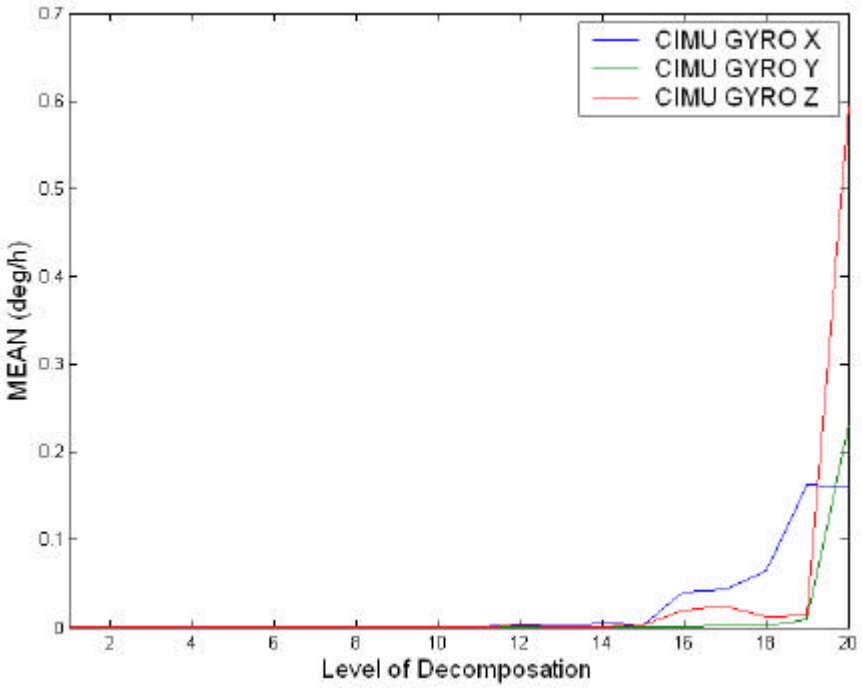

Figure 3.4 Mean of High Frequency Component Versus Wavelet Level for CIMU Gyros

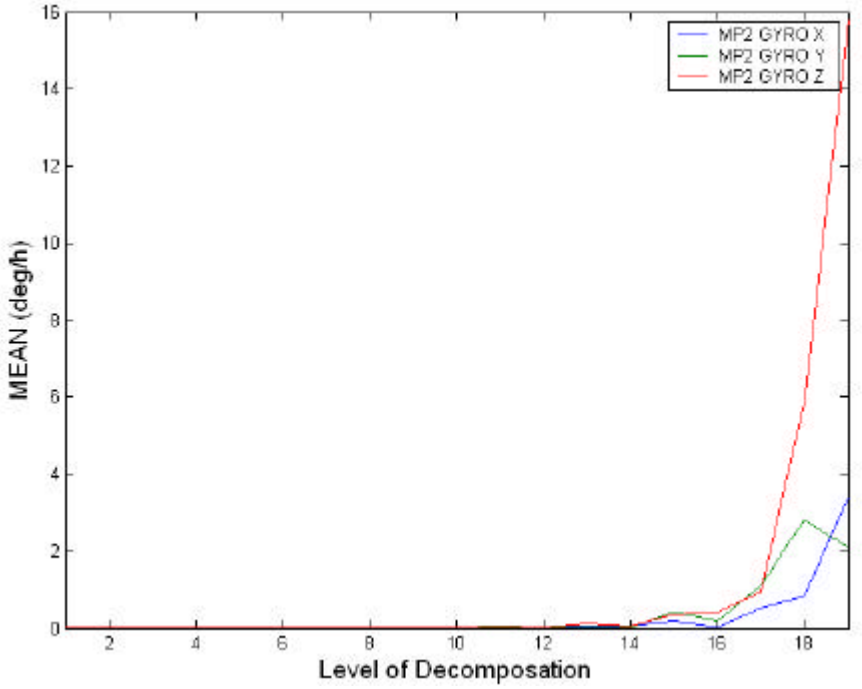

Figure 3.5 Mean of High Frequency Component Versus Wavelet Level for MotionPak II Gyros

Figure (3.6) shows the original data of CIMU Gyro X before (Figure 3.6a) and that after 15^{th} level decomposition (Figure 3.6b).

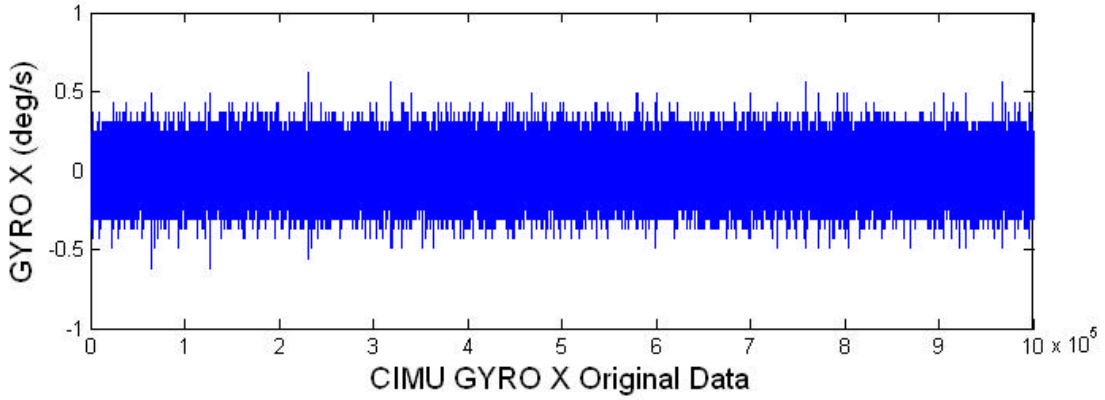

Figure 3.6a CIMU X-Axis Gyro Measurements

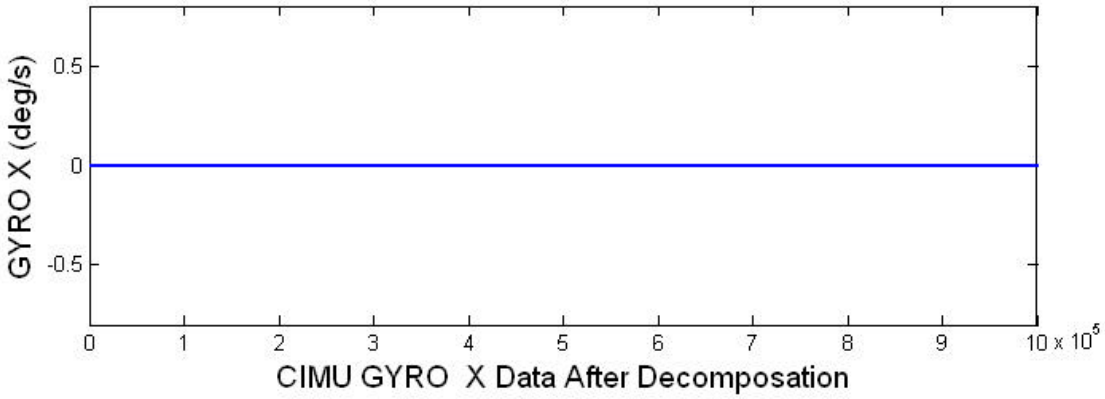

Figure 3.6b CIMU X-Axis Gyro Measurements After Decomposition

3.4 STOCHASTIC MODELING

Some of the important applications of modeling occur in simulation studies, performance evaluation, and Kalman filter design (Britting 1971). The basic difference between dynamic and stochastic modeling is as follows: in dynamic modeling, given one or more

inputs (input vector) and one or more outputs (output vector), it is desired to determine the input/output relationships from both time series. Applications include those where random noise is summing at the output (IEEE Std 952 1997).

In stochastic modeling, on the other hand, there may be no direct access to an input. A model is hypothesized which, as though excited by white noise, has the same output characteristics as the unit under test. Such models are not generally unique, so certain canonical forms are chosen (IEEE Std 952 1997). The next section will describe the general application of several methods in investigation of stochastic models.

3.4.1 AUTOCORRELATION FUNCTION

3.4.1.1 DEFINITION AND PROPERTY

The correlation function of a stochastic process with itself is called its autocorrelation function and is defined as (Brown 1983)

$$R_x(t_1, t_2) = E[X(t_1)X(t_2)] \tag{3.28}$$

where t_1 and t_2 are arbitrary sampling times. The units of a correlation function are equal to the product of the units of the signals of interest. The autocorrelation function of a stochastic process is essentially a measure of the dependence of the value of the process at one time with its value at other times.

A stochastic process is called stationary if its probability density functions are invariant with time (Brown 1983). The autocorrelation function of such a process depends only on

the time difference $t = t_1 - t_2$. Thus R_x reduces to a function of just the time difference variable t, that is,

$$R_x(t) = E[X(t)X(t+t)] \tag{3.29}$$

where t_1 is now denoted as t and t_2 is $(t+t)$. Stationary assures that the expectation is not dependent on t and the autocorrelation function is even (Brown 1983).

3.4.1.2 APPLICATION

A stationary Gaussian process $X(t)$ that has an exponential autocorrelation is called a Gauss-Markov process. The autocorrelation function for this process is then of the form (Brown 1983)

$$R_x(t) = s^2 e^{-b|t|} \tag{3.30}$$

The function is sketched in Figure (3.7). The noise variance value and time constant for the process are given by the s^2 and $1/b$ parameters, respectively. The correlation at time $1/b = t$ is

$$R_x(t) = s^2 e^{-1} = s^2 / e = 0.3678\, s^2 \tag{3.31}$$

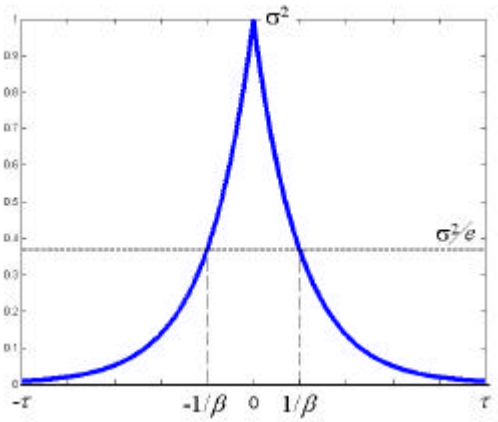

Figure 3.7 Autocorrelation Function

The exponential autocorrelation function indicates that sample values of the process gradually become less and less correlated as the time separation between samples increases. The autocorrelation function approaches zero as $t \to ¥$, and thus the mean value of the process must be zero.

The Gauss-Markov process is an important process in applied work because it seems to fit a large number of physical processes with reasonable accuracy, and it has a relatively simple mathematical description. As in the case of all stationary Gaussian processes, specification of the process autocorrelation function completely defines the process. This means that any desired higher-order probability density function for the process may be written out explicitly, given the autocorrelation function (Brown 1983).

Since this is a matter of statistical interference, there will always remain some statistical uncertainty in the result. For a Gaussian process, the variance of an experimentally determined autocorrelation function satisfies the inequality (Brown 1983)

$$Var[V_x(t)] \leq \frac{4}{T}\int_0^{\infty} R_x^2(t)\,dt \tag{3.32}$$

where it is assumed that a single sample realization of the process is being analyzed, and

- T is the time length of the experimental record
- $R_x(t)$ is the autocorrelation function of the Gaussian process under consideration
- $V_x(t)$ is the autocorrelation function determined from a finite record of experimental data.

The above equation can help to estimate the needed amount of data to reach a certain desired accuracy. Thus, for the Gaussian-Makov process (Brown 1983),

$$Var[V_x(t)] \le \frac{4}{T}\int_0^{\infty}\left(s^2 e^{-b|t|}\right)^2 dt = \frac{2s^4}{bT} \tag{3.33}$$

The accuracy is then defined as the ratio of the standard deviation of $V_x(t)$ to the variance of the process, $R_x(t)$, as:

$$accuracy = \frac{\sqrt{Var[V_x(t)]}}{s^2} \le \sqrt{\frac{2}{bT}} \tag{3.34}$$

Here is the autocorrelation function plot of X-axis gyro of CIMU two hours static data after 15 levels decomposition as shown in Chapter 3.3.2. In order to show clearly, only the center part of the plot is presented.

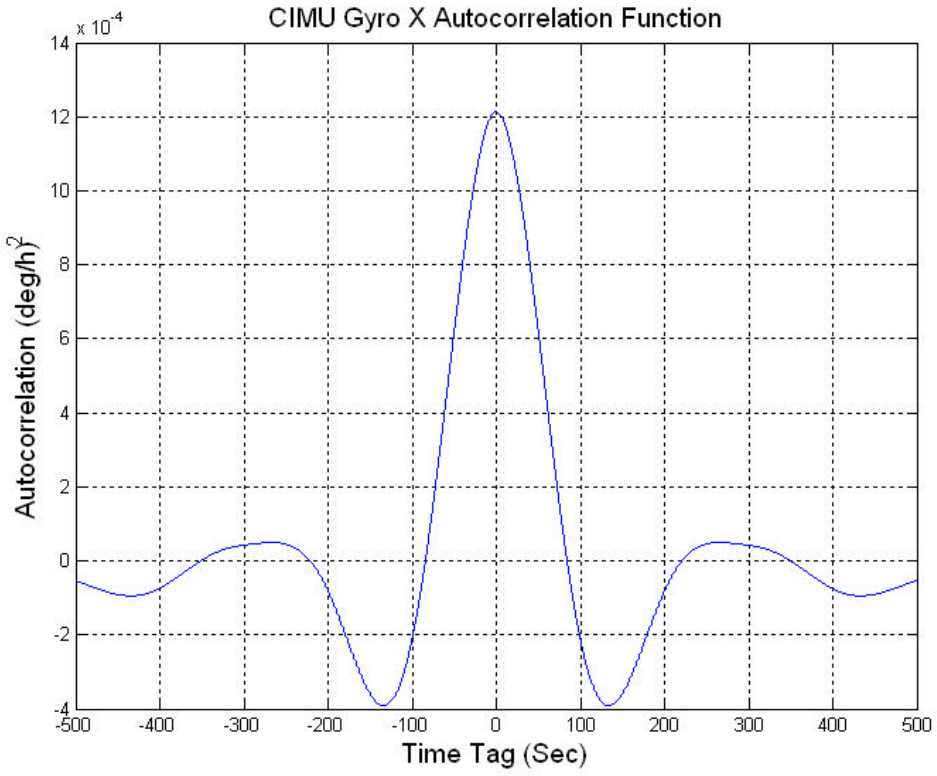

Figure 3.8 CIMU Gyro X Autocorrelation Function

Similar results can be obtained from other axes gyros. The estimated parameters are listed in Table (3.3). The same performance is applied on the data of MotionPak II gyros and the estimated parameters are listed in Table (3.3) as well.

Table 3.3 Gauss-Markov Autocorrelation Parameters

	σ^2 (deg^2/h^2)	$1/\beta$ (sec)	Accuracy (%)
CIMU Gyro X	1.22×10^{-3}	58	12.69
CIMU Gyro Y	7.05×10^{-5}	72	14.14
CIMU Gyro Z	5.70×10^{-3}	33	9.57
MP2 Gyro X	545.05	355	31.40
MP2 Gyro Y	235.11	512	37.71
MP2 Gyro Z	749.58	690	43.78

The accuracy values are obtained by using Equation (3.34) with the obtained parameters (T=2 hours). These numbers indicate that it is very difficult to obtain accurate autocorrelation parameters from experimental data, especially for high-grade IMU sensors.

3.4.2 POWER SPECTRAL DENSITY

The frequency domain approach of using the power spectral density to estimate transfer functions is straightforward but difficult for non-system analysts to understand. The Power Spectral Density (PSD) is the most commonly used representation of the spectral decomposition of a time series. It is a powerful tool for analyzing or characterizing data,

and stochastic modeling. The PSD, or spectrum analysis, is also better suited to analyzing periodic or non-periodic signals than other methods (IEEE Std 952 1997).

The basic relationship for stationary processes between the two sided PSD, $S(w)$, and the covariance, $K(t)$, which are Fourier transform pairs, is expressed by (IEEE Std 952 1997):

$$S(w) = \int_{-\infty}^{\infty} e^{-jwt} K(t) dt \tag{3.35}$$

It can be shown that for non-stationary processes, the average covariance $K(t)$ and average power spectrum $S(w)$ are related in the same way (Papoulis 1965).

It is most common for data to be taken at discrete times using a digital computer. Consider N samples of the sensor output with sample time Δt. Thus, the length of the time ensembles is $T = N \times \Delta t$. In the following computations, the one-sided PSD estimate is given by (IEEE Std1293-1998):

$$S^1(f) = \frac{1}{T}|X(f)|^2 \tag{3.36}$$

where $X(f)$ is the Fourier transform of the measured time series $x(t)$ and the superscript 1 in $S^1(f)$ to differentiate the one sided PSD. The discrete Fourier transform approximates the continuous Fourier transform at discrete frequencies f_j by (IEEE Std1293-1998)

$$X(f_j) \cong X_j \Delta t \tag{3.37}$$

with

$$f_j = \frac{j}{N \cdot \Delta t} = \frac{j}{T} Hz \tag{3.38}$$

Thus, the estimate from a finite span of sampled data of the one-sided PSD at frequency f_j is (IEEE Std1293-1998):

$$S^1(f) = \frac{\Delta t^2}{T} \left| X_j \right|^2 , \qquad j = 1, 2, \ldots, \left[\frac{N}{2} \right] \tag{3.39}$$

3.4.2.1 USEFUL PROPERTIES

For linear systems, the output PSD is the product of the input PSD and the magnitude squared of the system transfer function. If state space methods are used, the PSD matrices of the input and output are related to the system transfer function matrix by (IEEE Std 952 1997) :

$$S_{output}(w) = H(jw) S_{input}(w) H^{*T}(jw) \tag{3.40}$$

where H is the system transfer function matrix

H^{*T} is the complex conjugate transpose of H

S_{output} is the output PSD

S_{input} is the input PSD

Thus, for the special case of white noise input (S_{input} is equal to some constant value, i.e. N_i^2), the output PSD directly gives the system transfer function. The transfer function form of the stochastic model may be estimated directly from the PSD of the output data (on the assumption of an equivalent white noise driving function).

The idea of applying white noise and constructing the transfer function in this manner is important to stochastic modeling. In stochastic modeling, there may be no direct access to an input. A model is hypothesized which, as though excited by white noise, has the same output characteristics as the unit under test. The reason for that is, if the input is white noise, you can estimate the transfer function of a linear, minimum phase, time invariant system simply from the power spectrum of the output. Instead of getting the cross power spectral density (PSD) between input and output, the transfer function can be estimated from the power spectrum of the output alone. The phase information is uniquely determined from the magnitude response. Thus, for a linear time-invariant system, by having knowledge of the output only, and assuming white noise input, it is possible to characterize the unknown model. Such models are not generally unique, so certain canonical forms are usually used (IEEE Std952-1997).

For a process to have finite power, its PSD must eventually terminate in a negative slope at high frequencies. This property must be produced to satisfy the Nyquist sampling criterion for sampled data. Likewise, a PSD cannot continue to rise (without limit) toward zero frequency (over a finite time interval). In practice, the finite length of the time series limits this (IEEE Std952-1997).

3.4.2.2 APPLICATION

Normally, the PSD of a random process is expected to exhibit even order log-log slopes, indicating even powers of frequencies. Thus, the different types of noise imposed on the measurement are represented in the PSD by straight lines with different slopes. The

expressions of noise are shown together with Allan variance expressions in Chapter Four. The typical characteristic slopes are shown in Figure (3.9), where the actual units and frequency range are hypothetical. With real data, gradual transitions would exist between the different PSD slopes (IEEE Std1293-1998), rather than the sharp transitions in Figure (3.9); and the slopes might be different than −2, -1, 0, and +2 values in Figure (3.9). A certain amount of noise or hash would exist in the plot curve due to the uncertainty of the measured PSD.

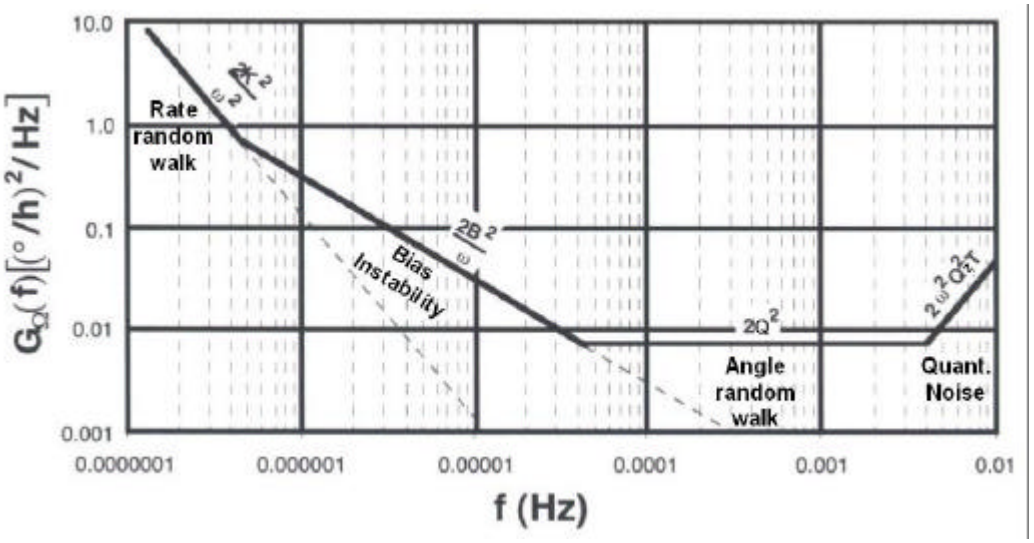

Figure 3.9 Hypothetical Gyro in Single-sided PSD Form (after IEEE Std952-1997)

3.4.2.3 TEST RESULTS

The same data sets used in section 3.3.2 are used here for power spectral density analysis. Applying the PSD method described previously, the PSD result on log-log plot is shown in Figure (3.10) for CIMU X-axis gyro data. Because of the bunching of the high frequency data points in the log-log plot, it is difficult to identify noise terms and obtain parameters in such conditions. Hence, the frequency averaging technique (IEEE Std

1293-1998) is used to reduce the number of points in the PSD result and make the noise term identification easier.

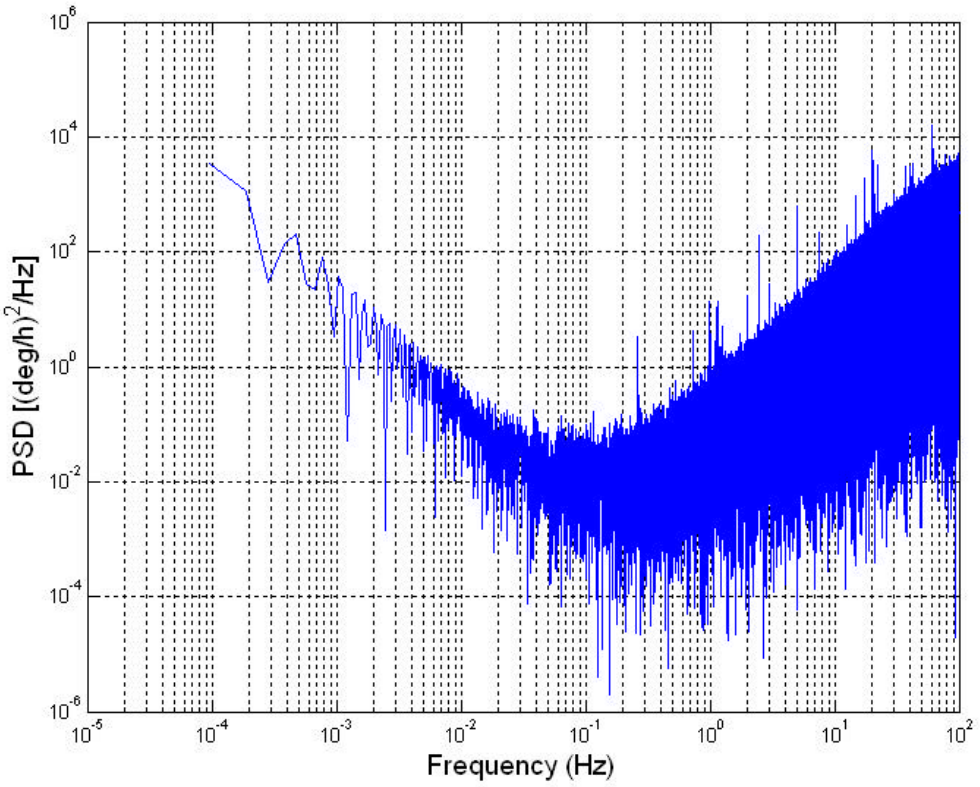

Figure 3.10 CIMU X-Gyro PSD Results

The frequency averaging technique is used to calculate a single PSD for, as an example, N = 32 768 measurements, and then average the adjacent frequency values according to the scheme in Table (3.4). That is to keep the first 32 frequency data points. And then, at each average level (N), obtain 16 averaged frequency data points from 2^N frequency data points. As a result, the low frequency part of the PSD plot has high uncertainty, but still conveys some information. The high frequency part of the PSD plot has the uncertainty obtained by ensemble averaging and is conveniently plotted with the low frequency data

because the frequency averaging prevents bunching of the high frequency data points in the log-log plot.

Table 3.4 Logarithmic Frequency Averaging of 32768 Points
(after IEEE Std1293-1998)

Frequency Data Points Index	Total Data Points Covered	Number of Points per Averaging	Number of Points to Plot	Average Level (N)
1-32	32	1	32	
33-64	32	2	16	1
65-128	64	4	16	2
129-256	128	8	16	3
257-512	256	16	16	4
513-1024	512	32	16	5
1025-2048	1024	64	16	6
2049-4096	2048	128	16	7
4097-8192	4096	256	16	8
8193-16384	8192	512	16	9
16385-32768	16384	1024	16	10

The PSD results with the frequency averaging technique are shown in Figure (3.11) for CIMU X-axis gyro data and Figure (3.12) for MotionPak II X-axis gyro data.

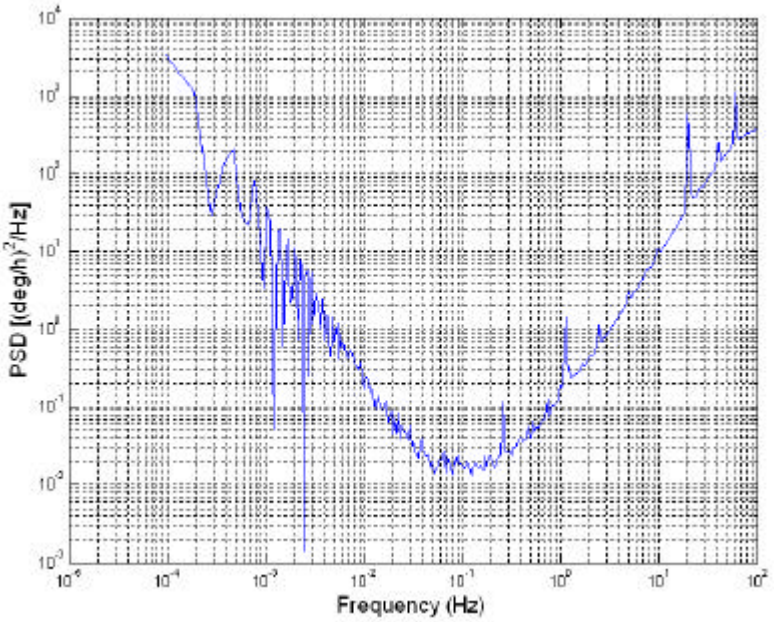

Figure 3.11 CIMU X-Gyro PSD Results with Frequency Averaging Technique

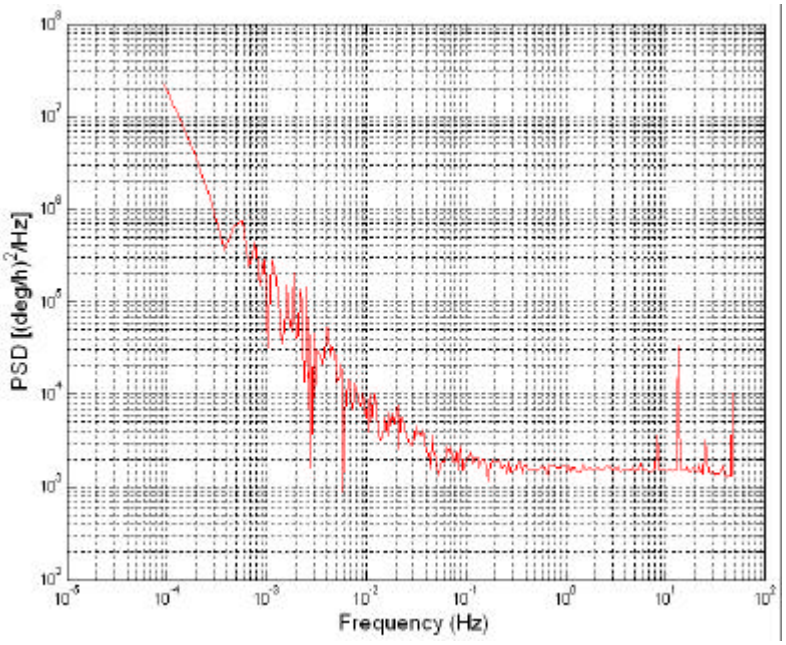

Figure 3.12 MotionPak II X-Gyro PSD Results with Frequency Averaging Technique

From Figure (3.11), the slopes of the curve include –2, 0, and +2, which indicate that the CIMU X-axis gyro data contains rate random walk, angle random walk, and quantization noise, respectively. The acquisition of parameters for noise terms from PSD result plot is complex. So here only the calculation of angle random walk parameter Q is discussed. According to IEEE Std 952 1997,

$$Q(^\circ/\sqrt{h}) = \frac{1}{60}\sqrt{\frac{1}{2}PSD\left[\left(\frac{^\circ}{h}\right)^2/Hz\right]} \tag{3.41}$$

The estimated results are listed in Table (3.5).

Table 3.5 PSD Estimation Results for the CIMU and the MotionPak II X-axis Gyro

	Sample Rate (Hz)	Random Walk ($deg/h^{1/2}$)
CIMU X Gyro	200	0.0015
MP2 X Gyro	100	0.5

From Figure (3.12), the slopes of the curve include –1 and 0, which indicate MotionPak II X-axis gyro data contains bias instability and angle random walk, respectively. According to Equation (3.41), the estimated angle random walk coefficient, Q, is listed in Table (3.5). These results shown in Table (3.5) will compare with Allan variance results later in Chapter Five.

3.4.3 VARIANCE TECHNIQUES

Another class of time domain methods, specifically several variance techniques, have been devised for stochastic modeling. They are basically very similar, and primarily differ in that various signal processing, by way of weighting functions, window

functions, etc., is incorporated into the analysis algorithms in order to achieve a particular desired result of improving the model characterizations (IEEE Std952-1997). The simplest is the Allan variance, which will be discussed in Chapter Four.

3.4.4 ADAPTIVE (SELF-LEARNING) KALMAN FILTER

The adaptive Kalman filter is another means of system identification (Gelb 1974). The noise covariance and dynamics may be estimated if the form of the model is known. This may be combined with a model adjustment or learning model approach for more flexibility.

In the conventional Kalman filter, all the process parameters are assumed to be known. They may vary with time but, if so, the nature of the variation is assumed to be known (Chapter 3.2). In physical problems this is often a quick assumption. There may be large uncertainty in some parameters because of inadequate prior test data about the process. Or, some parameters might be expected to change slowly with time, but the exact nature of the change is not predictable. In such cases, it is highly desirable to design the filter to be self-learning, so that it can self-adapt itself to the situation at hand, whatever that might be (Brown 1983).

Now this is the solution first presented by D.T. Magill (Sinha and Kuszta 1983) to put the whole adaptive filter system in perspective. Qualitatively, the adaptation proceeds as follows. Prior to receiving any measurements, the system must set the weight factors equal to the a priori probabilities. It has no better information about the unknown

parameter, e.g. a, as of this point in time. Then, as measurements are accumulated, each elemental Kalman filter sums its weighted squared residuals and uses this sum as the negative exponent in its Gaussian density computation. As time proceeds, the correct filter's residuals work out to be smaller (on the average) than the others, and thus its probability density is the largest and it is given the most weight in the blending of the elemental estimates. The measurement residuals are summed, with the effect being cumulative; and, in the limit, a weight factor of unity for the correct filter (and zero for others) is approached. In effect, the system "learns" which is the correct a_i and then assigns all of the weight to this filter's estimate (Brown 1983).

The adaptive scheme due to Magill is important because it is optimal (within the Gaussian assumption), and it serves as a point of departure for other less rigorous approaches (Brown 1983). After all, the system only has to implement the various options and choose the one with the smallest average residuals. Simpler intuitive algorithms might not converge quite as rapidly as the optimal scheme, but they might well be considerably easier to implement.

3.4.5 SUMMARY

This chapter summarizes different techniques for the stochastic modeling of inertial sensors errors. The selection of method is depends on the application requirements. From the discussion of different stochastic modeling methods, the benefits and limitations of each method are summarized in Table (3.6).

Table 3.6 Comparing with Different Stochastic Modeling Methods

	Autocorrelation Function	Power Spectral Density	Variance Technique	Adaptive Kalman Filter
Benefits	▪ Suitable for periodic and non-periodic signals analysis ▪ Fourier transform pairs with power spectral density	▪ Suitable for periodic and non-periodic signals analysis ▪ Fourier transform pairs with autocorrelation	▪ Detailed understanding of a data set in time domain ▪ Easy to interpret and extract useful parameters pertaining to the different errors	▪ Ability to track high-frequency information in the signal ▪ Self-adapted to the situation at hand
Limitations	▪ De-noise method should be applied first. ▪ Long-term signal is needed for acceptable solution ▪ Very model sensitive	▪ Frequency averaging technique is needed ▪ Parameters abstraction is complex	▪ Results depend upon the understanding of the physics of the process ▪ Long-term data is needed for improving estimation accuracy	▪ Add-on computational complexity ▪ Possible existence of blunders limits the applicability of the algorithm

CHAPTER FOUR: ALLAN VARIANCE DEFINITION AND PROPERTIES

This chapter introduces the definition and properties of Allan variance as a tool for modeling inertial sensor errors.

4.1 LITERATURE REVIEW

In 1966, David Allan proposed a simple variance analysis method for the study of oscillator stability (Allan 1966), that is the Allan variance method. After its introduction, this method was widely adopted by the time and frequency standards community for the characterization of phase and frequency instability of precision oscillators. Because of the close analogies to inertial sensors, the method has been adapted to random drift characterization of a variety of devices (IEEE Std952-1997). The 1980s witnessed the first paper related Allan variance with inertial sensors (Kochakian 1980). In 1983, M. Tehrani gave out the detailed deviation about the Allan variance noise terms expression from their rate noise power spectral density for the ring laser gyro (Tehrani 1983). This method has since been applied to gyro drift analysis. In 1998, IEEE (Institute of Electrical and Electronics Engineers, Inc.) standard introduced Allan variance method as a noise identification method for linear, single, non-gyroscopic accelerometer analysis (IEEE Std1293-1998). In 2003, the Allan variance method was first applied in Micro Electrical Mechanical Sensor (MEMS) noise identification (Hou and El-Sheimy 2003).

From the discussion in previous chapter, although computations of the autocorrelation function or the power spectral density distribution do contain a complete description of

the error sources, these results are difficult to interpret or extract. Allan variance is a time domain analysis technique originally developed to study the frequency stability of oscillators. It can be used to determine the character of the underlying random processes that give rise to the data noise. As such, it helps identify the source of a given noise term in the data. The source may be inherent in the instrument, but in the absence of a plausible mechanism within the instrument, its origin should be sought in the test set up. The Allan variance method adopted in this thesis may be used as a stand-alone method of data analysis or to complement any of the frequency domain analysis techniques mentioned in Chapter Three. It should be mentioned that the technique could be applied to the noise study of any instrument. Its value, however, depends upon the degree of understanding of the physics of the instrument. In the Allan variance method of data analysis, the uncertainty in the data is assumed to be generated by noise sources of specific character. The magnitude of each noise source covariance is then estimated from the data. The definition of the Allan variance and a discussion of its use in frequency and time metrology are presented in Allan (1966) and IEEE (Std1139-1988). The key attribute of the method is that it allows for a finer, easier characterization and identification of error sources and their contribution to the overall noise statistics (Lawrence and DarryII 1997).

In this thesis, Allan's definition and results are related to seven noise terms and are expressed in a notation appropriate for inertial sensor data reduction. The five basic noise terms are angle random walk, rate random walk, bias instability, quantization noise, and

drift rate ramp. In addition, the sinusoidal noise and exponentially correlated (Markov) noise can also be identified through the Allan variance method.

4.2 METHODOLOGY

Assume there are N consecutive data points, each having a sample time of t_0. Forming a group of n consecutive data points (with $n<N/2$), each member of the group is a cluster, as shown in Figure (4.1).

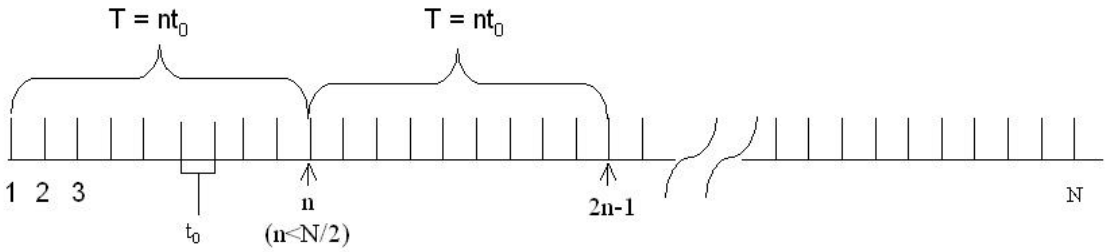

Figure 4.1 Schematic of the Data Structure used in the Derivation of Allan Variance

Associated with each cluster is a time, T, which is equal to nt_0. If the instantaneous output rate of inertial sensor is $W(t)$, the cluster average is defined as:

$$\overline{\Omega}_k(T)=\frac{1}{T}\int_{t_K}^{t_k+T}\Omega(t)\,dt \tag{4.1}$$

where $\overline{\Omega}_k(t)$ represents the cluster average of the output rate for a cluster which starts from the k^{th} data point and contains n data points. The definition of the subsequent cluster average is:

$$\overline{\Omega}_{next}(T)=\frac{1}{T}\int_{t_{k+1}}^{t_{k+1}+T}\Omega(t)\,dt \tag{4.2}$$

where $t_{k+1} = t_k+T$.

Performing the average operation for each two adjoining clusters and form the differences

$$x_{k+1,k} = \overline{\Omega}_{next}(T) - \overline{\Omega}_k(T) \tag{4.3}$$

For each cluster time *T*, the ensemble of *x* defined by Equation (4.3) forms a set of random variables. The quantity of interest is the variance of *x*s over all the clusters of the same size that can be formed from entire data.

Thus, the Allan variance of length *T* is defined as (IEEE Std952-1997):

$$s^2(T) = \frac{1}{2}\left\langle \left[\overline{\Omega}_{next}(T) - \overline{\Omega}_k(T)\right]^2 \right\rangle \tag{4.4}$$

The brackets in Equation (4.4) denote the averaging operation over the ensemble of clusters. Thus, above equation can be rewritten as:

$$s^2(T) = \frac{1}{2(N-2n)} \sum_{k=1}^{N-2n} \left[\overline{\Omega}_{next}(T) - \overline{\Omega}_k(T)\right]^2 \tag{4.5}$$

Clearly, for any finite number of data points (*N*), a finite number of clusters of a fixed length (*T*) can be formed. Hence, Equation (4.5) represents an estimation of the quantity $s^2(T)$ whose quality of estimate depends on the number of independent clusters of a fixed length that can be formed.

The Allan variance can also be defined in terms of the output angle or velocity as (IEEE Std952-1997)

$$q(t) = \int^{t} \Omega(t) dt \tag{4.6}$$

The lower integration limit is not specified, as only angle or velocity differences are employed in the definitions. Angle or velocity measurements are made at discrete times given by $t = kt_0$, $k = 1,2,3,¼, N$. Accordingly, the notation is simplified by writing $q_k = q(kt_0)$. Equations (4.1) and (4.2) can, then, be redefined by

$$\overline{\Omega}_k(T) = \frac{q_{k+n} - q_k}{T} \tag{4.7}$$

and

$$\overline{\Omega}_{next}(T) = \frac{q_{k+2n} - q_{k+n}}{T} \tag{4.8}$$

According to Equation (4.5), Allan variance is estimated as follows:

$$s^2(T) = \frac{1}{2T^2(N-2n)} \sum_{k=1}^{N-2n} (q_{k+2n} - 2q_{k+n} + q_k)^2 \tag{4.9}$$

The Allan variance is a measure of the stability of sensor output. As such it must be related to the statistical properties of the intrinsic random processes, which affect the sensor performance.

There is a unique relationship that exists between $s^2(T)$ and the power spectral density of the intrinsic random processes. This relationship is (IEEE Std952-1997)

$$s^2(T) = 4 \int_0^{\infty} df \cdot S_{\Omega}(f) \cdot \frac{\sin^4(pfT)}{(pfT)^2} \tag{4.10}$$

where $S_W(f)$ is the power spectral density of the random process $W(T)$. In following, the derivation of above relationship is given.

Equation (4.4) can be expanded to give

$$s^{2}(T)=\frac{1}{2}\left\langle \overline{\Omega}_{next}^{2}(T)\right\rangle +\frac{1}{2}\left\langle \overline{\Omega}_{k}^{2}(T)\right\rangle -\left\langle \overline{\Omega}_{next1}^{2}(T)\overline{\Omega}_{k}^{2}(T)\right\rangle \tag{4.11}$$

From Equation (4.1), we can write

$$\left\langle \overline{\Omega}_{k}^{2}(T)\right\rangle =\frac{1}{T^{2}}\int_{t_k}^{t_K+T}dt\int_{t_k}^{t_k+T}\left\langle \Omega(t)\Omega(t')\right\rangle dt' \tag{4.12}$$

where $R(t,t')=\langle W(t)\ W(t')\rangle$ is the rate correlation function. In what follows, we assume that the random processes $W(T)$ are all stationary in time. Therefore,

$$R(t,t')=R(t'-t)\equiv R(t) \tag{4.13}$$

The rate power spectral density is the Fourier transform of the $R(t)$. Thus,

$$S_{\Omega}(f)=\int_{-\infty}^{\infty}R(t)e^{-2pift}\,dt \tag{4.14}$$

or, inversely

$$R(t)=\int_{-\infty}^{\infty}S_{\Omega}(f)e^{2pift}\,df \tag{4.15}$$

Substitution of Equation (4.15) in Equation (4.12) yields

$$\left\langle \overline{\Omega}_{k}^{2}(T)\right\rangle =\frac{1}{T^{2}}\int_{-\infty}^{\infty}S_{\Omega}(f)df\int_{t_k}^{t_K+T}dt\int_{t_k}^{t_k+T}e^{2pif(t'-t)}dt' \tag{4.16}$$

where we have changed the order of integration. The double integral over time is readily calculated to give

$$\int_{t_k}^{t_K+T}dt\int_{t_k}^{t_k+T}e^{2pif(t'-t)}dt'=\frac{\sin^{2}pfT}{(pf)^{2}} \tag{4.17}$$

The use of Equation (4.17) in Equation (4.16) gives

$$\left\langle \overline{\Omega}_k^2(T) \right\rangle = \int_{-\infty}^{\infty} S_\Omega(f) \frac{\sin^2 pfT}{(pfT)^2} df \tag{4.19}$$

Since $<\overline{\Omega}_k^2(T)>$ does not depend on t_k, the same expression holds for $<\overline{\Omega}_{next}^2(T)>$. Thus,

$$\left\langle \overline{\Omega}_{next}^2(T) \right\rangle = \int_{-\infty}^{\infty} S_\Omega(f) \frac{\sin^2 pfT}{(pfT)^2} df \tag{4.20}$$

We now calculate $<W_{next}(T)\, W_k(T)>$. From Equation (4.1) we can write

$$\begin{aligned} \left\langle \overline{\Omega}_{next1}(T) \overline{\Omega}_k(T) \right\rangle &= \frac{1}{T^2} \int_{t_k}^{t_k+T} dt \int_{t_k+T}^{t_k+2T} \langle \Omega(t) \Omega(t') \rangle dt' \\ &= \frac{1}{T^2} \int_{-\infty}^{\infty} S_\Omega(f) df \int_{t_k}^{t_k+T} dt \int_{t_k+T}^{t_k+2T} e^{2pif(t'-t)} dt' \end{aligned} \tag{4.21}$$

Straightforward integration of the double integral over time yields

$$\int_{t_k}^{t_k+T} dt \int_{t_k+T}^{t_k+2T} e^{2pif(t'-t)} dt' = e^{2pifT} \frac{\sin^2 pfT}{(pf)^2} \tag{4.22}$$

From this

$$\left\langle \overline{\Omega}_{next}(T) \overline{\Omega}_k(T) \right\rangle = \int_{-\infty}^{\infty} S_\Omega(f) e^{2pifT} \frac{\sin^2 pfT}{(pfT)^2} df \tag{4.23}$$

Substituting Equations (4.19), (4.20), and (4.23) in Equation (4.11) gives

$$\begin{aligned} s^2(T) &= \int_{-\infty}^{\infty} S_\Omega(f) (1 - e^{2pifT}) \frac{\sin^2 pfT}{(pfT)^2} df \\ &= 2 \int_{-\infty}^{\infty} S_\Omega(f) \frac{\sin^4 pfT}{(pfT)^2} df - i \int_{-\infty}^{\infty} S_\Omega(f) \frac{\sin^2 pfT \sin 2pfT}{(pfT)^2} df \end{aligned} \tag{4.24}$$

The fact is that a real function requires that the second integral in Equation (4.24) be identically zero. This is satisfied if $S_\Omega(f)$ is an even function of f, which is the same

requirement for the reality of correlation function (Tehrani 1983). Therefore, Equation (4.24) can be written as

$$s^2(T) = 4\int_0^\infty S_\Omega(f)\frac{\sin^4(pfT)}{(pfT)^2}df \qquad (4.25)$$

Equation (4.25) is same as Equation (4.10), which is the desired relation.

In the derivation of Equation (4.25), it is assumed that the random process *W(T)* is stationary in time (Tehrani 1983). For non-stationary processes, such as flicker noise, the time average power spectral density should be used.

Equation (4.25) states that the Allan variance is proportional to the total power output of the random process when passed through a filter with the transfer function of the form $sin^4(x)/(x)^2$. This particular transfer function is the result of the method used to create and operate on the clusters.

Equation (4.25) is the focal point of the Allan variance method. This equation will be used to calculate the Allan variance from the rate noise PSD. The power spectral density of any physically meaningful random process can be substituted in the integral, and an expression for the Allan variance $s^2(T)$ as a function of cluster length is identified. Conversely, since $s^2(T)$ is a measurable quantity, a log-log plot of $s(T)$ versus T provides a direct indication of the types of random processes, which exist in the inertial sensor data. The corresponding Allan variance of a stochastic process may be uniquely derived

from its power spectral density; however, there is no general inversion formula because there is no one-to-one relation (Tehrani 1983).

It is evident from Equation (4.25) and the above interpretation that the filter bandwidth depends on T. This suggests that different types of random processes can be examined by adjusting the filter bandwidth, namely by varying T. Thus, the Allan variance method provides a means of identifying and quantifying various noise terms that exist in the data. It is normally plotted as the square root of the Allan variance versus T, $[s(T)]$, on a log-log plot. To estimate the amplitude of different noise components, it is convenient to let $n = 2^l, l = 0,1,2,\ldots$(Allan, 1987).

4.3 REPRESENTATION OF NOISE TERMS IN ALLAN VARIANCE

The following sub-sections will show the integral solution for a number of specific noise terms, which are either known to exist in the inertial sensor or are suspected to influence the data. The definition is defined in Allan (1966) and Keshner (1982), and the detail derivations are given in Tehrani (1983). The physical origin of each noise source term will be discussed.

4.3.1 QUANTIZATION NOISE

Quantization noise is one of the types of error introduced into an analog signal that results from encoding it in digital form. Quantization noise is caused by the small

differences between the actual amplitudes of the points being sampled and the bit resolution of the analog-to-digital converter (Savage 2002).

The angle PSD for such a process, given in Papoulis (1991) is:

$$S_q(f) = T_z Q_z^2 \left(\frac{\sin^2(pfT_z)}{(pfT_z)^2} \right) \approx T_z Q_z^2 \qquad f < \frac{1}{2T_z} \tag{4.26}$$

where Q_z is the quantization noise coefficient

T_z is the sample interval

The theoretical limit for Q_z is equal to $S/12^{1/2}$ where S is the gyro-scaling coefficient, for tests with fixed and uniform sampling times. The rate PSD is related to the angle PSD through the equation:

$$S_\Omega(2pf) = (2pf)^2 S_q(2pf) \tag{4.27}$$

and is (IEEE 952 1997)

$$S_\Omega(f) = \frac{4Q_z^2}{T_z} \sin^2(pfT_z) \approx (2pf)^2 T_z Q_z^2 \qquad f < \frac{1}{2T_z} \tag{4.28}$$

Substituting Equation (4.28) in Equation (4.25) and performing the integration yields:

$$s^2(T) = \frac{3Q_z^2}{T^2} \tag{4.29}$$

Thus

$$s(T) = Q_z \frac{\sqrt{3}}{T} \tag{4.30}$$

This indicates that the quantization noise is represented by a slope of –1 in a log-log plot of $s(T)$ versus T, as shown in Figure (4.2). The magnitude of this noise can be read off the slope line at $T = 3^{1/2}$.

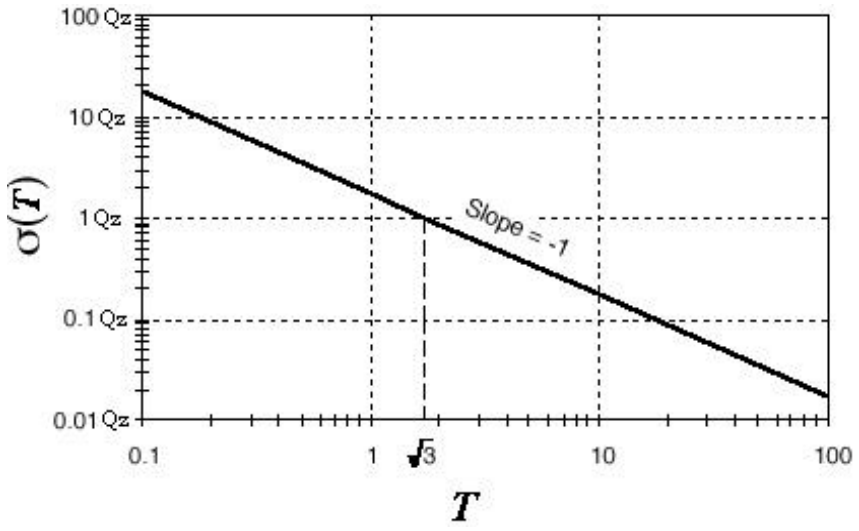

Figure 4.2 ***s (T)*** **Plot for Quantization Noise (after IEEE 952 1997)**

It should be noted that there are other noise terms with different spectral characteristics, such as flicker angle noise and white angle noise, that lead to the same Allan variance T dependence. Also, it should be noted that quantization noise has a short correlation time or equivalent a wide bandwidth. Wideband noise can usually be filtered out because of low bandwidth of the vehicle motion in many applications; it is not a major source of error (Lawrence and DarryII 1997).

4.3.2 ANGLE (VELOCITY) RANDOM WALK

High frequency noise terms that have correlation time much shorter than the sample time can contribute to the gyro angle (or accelerometer velocity) random walk. However, most of these sources can be eliminated by design (IEEE 952 1997). These noise terms are all

characterized by a white noise spectrum on the gyro (or accelerometer) rate output. Angle random walk, if not modeled accurately, can be a major source of error that limits the performance of an attitude control system (Lawrence and DarryII 1997).

The associated rate noise PSD is represented by (IEEE 952 1997):

$$S_{\Omega}(f)=Q^2 \tag{4.31}$$

where Q is the angle (velocity) random walk coefficient.

Substituting Equation (4.31) in Equation (4.25) and performing the integration yields:

$$s^2(T)=4\int_0^{\infty} Q^2 \frac{\sin^4 pfT}{(pfT)^2} df \tag{4.32}$$

If the variable of integration is changed to $u=pfT$, it gives

$$s^2(T)=\frac{4}{pT}\int_0^{\infty} Q^2 \frac{\sin^4 u}{(u)^2} du \tag{4.33}$$

which can be simplified to

$$s^2(T)=\frac{4Q^2}{pT}\int_0^{\infty} \frac{\sin^4 u}{(u)^2} du \tag{4.34}$$

The value of the integral in Equation (4.34) is given in Gradshteyn and Ryzhik (1980) as

$$\int_0^{\infty} \frac{\sin^4 u}{(u)^2} du=\frac{p}{4} \tag{4.35}$$

The Allan variance for angle (velocity) random walk becomes

$$s^2(T)=\frac{Q^2}{T} \tag{4.36}$$

Then,

$$s(T) = \frac{Q}{\sqrt{T}} \tag{4.37}$$

As shown in Figure (4.3), Equation (4.37) indicates that a log-log plot of $s(T)$ versus T has a slope of $-1/2$. Furthermore, the numerical value of Q can be obtained directly by reading the slope line at $T = 1$.

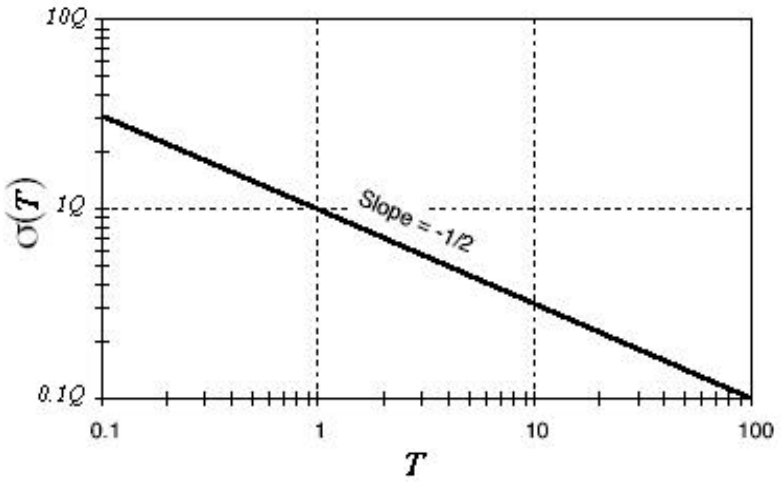

Figure 4.3 ***s(T)*** **plot for angle (velocity) random walk (after IEEE 952 1997)**

4.3.3 BIAS INSTABILITY

The origin of this noise is the electronics, or other components susceptible to random flickering (Keshner 1982). Because of its low-frequency nature it shows as the bias fluctuations in the data. The rate PSD associated with this noise is (IEEE 952 1997):

$$S_{\Omega}(f) = \begin{cases} \left(\frac{B^2}{2p}\right)\frac{1}{f} & f \le f_0 \\ 0 & f > f_0 \end{cases} \tag{4.38}$$

where B is the bias instability coefficient

f_0 is the cutoff frequency

Substitution of Equation (4.38) in Equation (4.25) and according to Equation (4.33):

$$s^2(T) = \frac{2B^2}{p}\int_0^{pTf_0}\frac{\sin^4 u}{u^3} \tag{4.39}$$

Now, consider the integral

$$I(a) = \int_0^a \frac{\sin^4 u}{u^3}du \tag{4.40}$$

According to Gradshteyn and Ryzhik (1980),

$$I(a) = -\frac{\sin^3 a}{2a^2}(\sin a + 4a\cos a) - 8\int_0^a \frac{\sin^4 u}{u}du + 6\int_0^a \frac{\sin^2 u}{u}du \tag{4.41}$$

Also, from Gradshteyn and Ryzhik (1980), we can write

$$\int \frac{\sin^4 u}{u}du = \frac{3}{8}\ln u + \frac{1}{8}Ci(4u) - \frac{1}{2}Ci(2u) \tag{4.42}$$

and

$$\int \frac{\sin^2 u}{u}du = \frac{1}{2}\ln u - \frac{1}{2}Ci(2u) \tag{4.43}$$

where C_i is the cosine-integral function, defined as

$$Ci(x) = \int_x^\infty \frac{\cos t}{t}dt \tag{4.44}$$

Substituting Equations (4.42) and (4.43) in Equation (4.41) gives

$$I(a) = -\frac{\sin^3 a}{2a^2}(\sin a + 4a\cos a) + Ci(2a) - Ci(4a) - \lim_{x\to 0}[Ci(2x) - Ci(4x)] \tag{4.45}$$

The last term in Equation (4.45) can be calculated from the expansion of C_i (x)

$$Ci(x) = C + \ln x + \sum_{k=1}^{\infty} (-1)^k \frac{x^{2k}}{2k(2k)!} \tag{4.46}$$

where C is the Euler constant. Using Equation (4.46), we can write

$$\lim_{x\to 0}[Ci(2x) - Ci(4x)] = \lim_{x\to 0}\left(\ln \frac{2x}{4x}\right) = -\ln 2 \tag{4.47}$$

To complete the derivation, substitute Equation (4.41), (4.45), and (4.47) in Equation (4.39), which gives

$$s^2(T) = \frac{2B^2}{p}\left[\ln 2 - \frac{\sin^3 x}{2x^2}(\sin x + 4x\cos x) + Ci(2x) - Ci(4x)\right] \tag{4.48}$$

where x is pf_0T.

From Equation (4.48), it is shown

$$s^2(T) \to 0 \qquad for\ T << \frac{1}{f_0} \tag{4.49}$$

and

$$s^2(T) \to \frac{2B^2}{p}\ln 2 \qquad for\ T >> \frac{1}{f_0} \tag{4.50}$$

Equation (4.50) can be simplified as

$$s(T) \to \sqrt{\frac{2\ln 2}{p}}\, B \cong 0.664B \qquad for\ T >> \frac{1}{f_0} \tag{4.51}$$

Figure (4.4) represents a log-log plot of square root of Equation (4.48). It is seen that Allan standard deviation begins with a slope of +1 for $f_0 << 1/T$ and reaches the asymptotic value of 0.664B for T much longer than the inverse cut-off frequency. Thus

the flat region of the plot can be examined to estimate the limit of the bias instability. Of course, such behaviour, particularly the rising part of the curve, may be overshadowed by the influence of other noise terms (IEEE 952 1997).

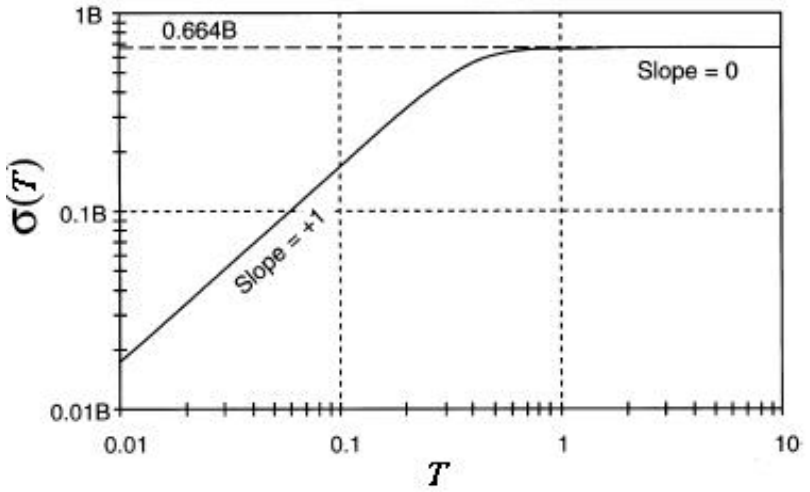

Figure 4.4 ***s(T)*** **plot for bias instability (for** $f_0 = 1$**) (after IEEE 952 1997).**

4.3.4 RATE RANDOM WALK

This is a random process of uncertain origin, possibly a limiting case of an exponentially correlated noise with a very long correlation time. The rate PSD associated with this noise is (IEEE 952 1997):

$$S_{\Omega}(f) = \left(\frac{K}{2p}\right)^2 \frac{1}{f^2} \tag{4.52}$$

where K is the rate random walk coefficient.

Substituting Equation (4.52) in Equation (4.25) and performing the integration yields:

$$s^2(T) = \frac{K^2 T}{3} \tag{4.53}$$

Thus

$$s(T) = K\sqrt{\frac{T}{3}} \tag{4.54}$$

This indicates that rate random walk is represented by a slope of +1/2 on a log-log plot of $s(T)$ versus T, as shown in Figure (4.5). The magnitude of this noise, K can be read off the slope line at $T = 3$.

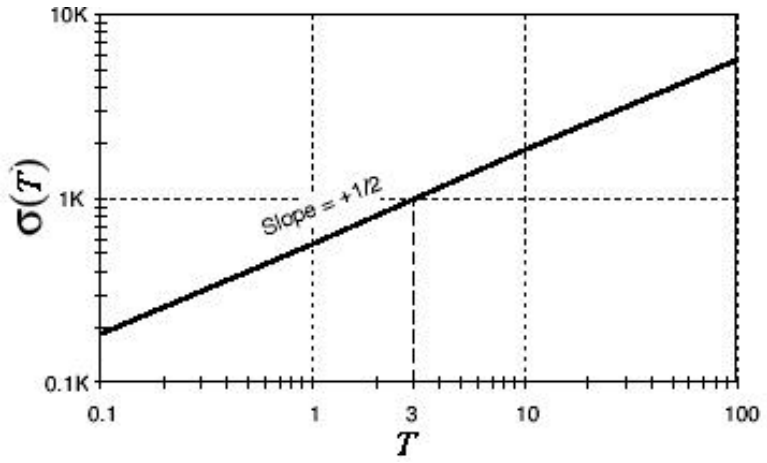

Figure 4.5 ***s(T)*** **plot for rate random walk (after IEEE 952 1997)**

4.3.5 DRIFT RATE RAMP

The error terms considered thus far are of random character. It is, however, useful to determine the behaviour of $s(T)$ under systematic (deterministic) errors. One such error is the drift rate ramp defined as (IEEE 952 1997):

$$\Omega = Rt \tag{4.55}$$

where R is the drift rate ramp coefficient

By forming and operating on the clusters of data containing an input given by Equation (4.55), we obtain:

$$s^2(T) = \frac{R^2 T^2}{2} \tag{4.56}$$

Thus,

$$s(T) = R\frac{T}{\sqrt{2}} \tag{4.57}$$

This indicates that the drift rate ramp noise has a slope of +1 in the log-log plot of $s(T)$ versus T, as shown in Figure (4.6). The amplitude of drift rate ramp R can be obtained from the slope line at $T = 2^{1/2}$.

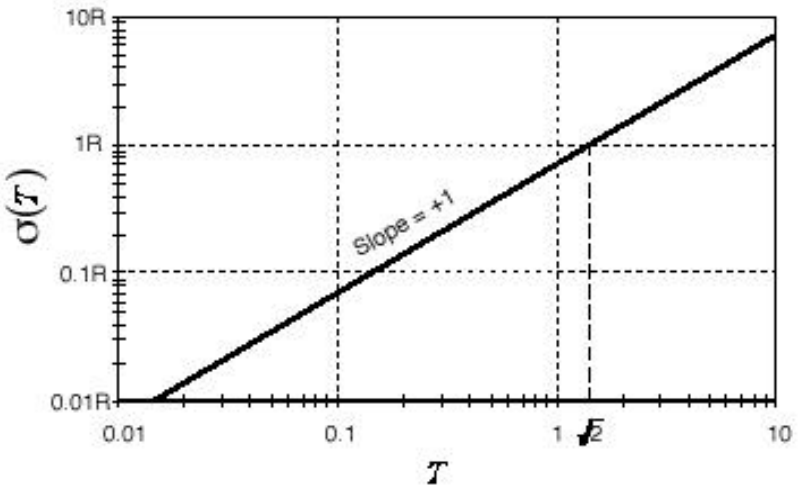

Figure 4.6 ***s(T)*** **plot for drift rate ramp (after IEEE 952 1997)**

The rate PSD associated with this noise is (IEEE 952 1997):

$$S_\Omega(f) = \frac{R^2}{(2pf)^3} \tag{4.58}$$

It should be noted that there might be a flicker acceleration noise with $1/f^3$ PSD that leads to the same Allan variance T dependence.

4.3.6 EXPONENTIALLY CORRELATED (MARKOV) NOISE

This noise is characterized by an exponential decaying function with a finite correlation time. The rate PSD for such a process (IEEE 952 1997):

$$S_\Omega(f) = \frac{(q_c T_c)^2}{1 + (2\pi f T_c)^2} \tag{4.59}$$

where q_c is the noise amplitude

T_c is the correlation time

Substitution of Equation (4.59) in Equation (4.25) and performing the integration yields:

$$\sigma^2(T) = \frac{(q_c T_c)^2}{T}\left[1 - \frac{T_c}{2T}\left(3 - 4e^{-\frac{T}{T_c}} + e^{-\frac{2T}{T_c}}\right)\right] \tag{4.60}$$

Figure (4.7) shows a log-log plot of square root of Equation (4.60). It is instructive to examine various limits of this equation. For T much longer than the correlation time, it is found that:

$$\sigma^2(T) \Rightarrow \frac{(q_c T_c)^2}{T} \qquad T >> T_c \tag{4.61}$$

which is the Allan variance for angle (velocity) random walk where $Q = q_c T_c$ is the angle (velocity) random walk coefficient. For T much smaller than the correlation time, Equation (4.60) reduces to:

$$s^2(T) \Rightarrow \frac{(q_c)^2}{3} T \qquad T << T_c \tag{4.62}$$

which is the Allan variance for rate random walk.

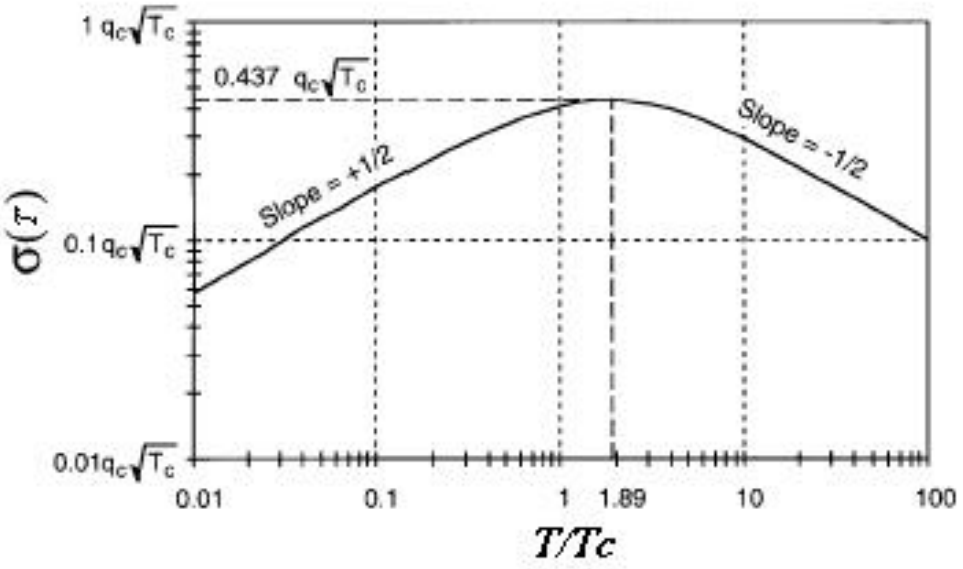

Figure 4.7 ***s(T)*** **plot for correlated noise (after IEEE 952 1997)**

4.3.7 SINUSOIDAL NOISE

The PSD of this noise is characterized by one or more distinct frequencies. A low-frequency source could be the slow motion of the test platform due to periodic environmental changes. A representation of the PSD of this noise containing a single frequency is given as (IEEE 952 1997):

$$S_\Omega(f) = \frac{1}{2}\Omega_0^2[d(f - f_0) + d(f + f_0)] \tag{4.63}$$

where W_0 is the amplitude

f_0 is the frequency

$d(x)$ is the Dirac delta function

Multiple frequency sinusoidal errors can be similarly represented by a sum of terms such as Equation (4.63) at their respective frequencies and amplitudes. Substitution of Equation (4.63) in Equation (4.25) and performing the integration yields:

$$s^2(T) = \Omega_0^2 \left[\frac{\sin^2 p f_0 T}{p f_0 T} \right]^2 \tag{4.64}$$

Figure (4.8) shows a log-log plot of square root of Equation (4.64). Thus, the root Allan variance of a sinusoid when plotted in log-log scale would indicate sinusoidal behaviour with successive peaks attenuated at a slope of -1. Identification and estimation of this noise in data requires the observation of several peaks. As is seen however, the amplitudes of consecutive peaks fall off rapidly and may be masked by higher order peaks of other frequencies making observation difficult. This is one case where a conventional PSD plot is superior in identifying the sinusoidal components (Lawrence and DarryII 1997).

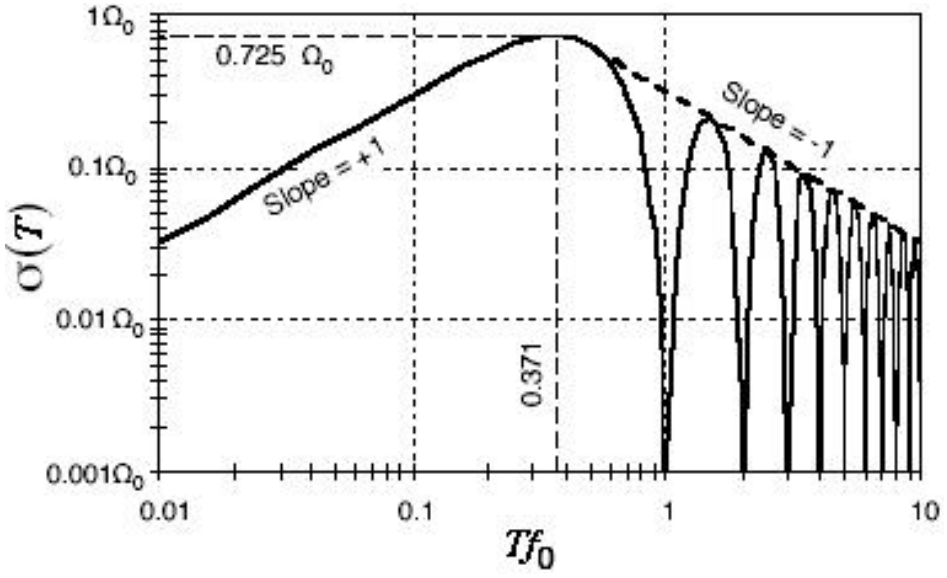

Figure 4.8 ***s(T)*** **plot for sinusoidal error (after IEEE 952 1997)**

4.4 SAMPLE PLOT OF ALLAN VARIANCE

In general, any number of the random process discussed above (as well as others) can be present in the data. Thus, a typical Allan variance plot looks like the one shown in Figure (4.9). Experience shows that in most cases, different noise terms appear in different regions of *T*. this allows easy identification of various random processes that exist in the data.

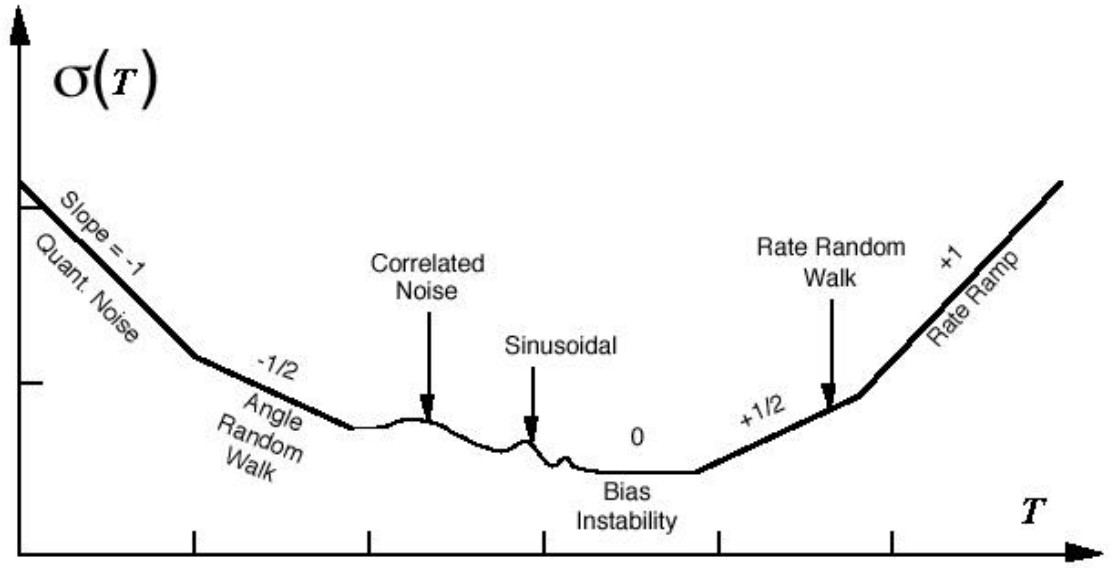

Figure 4.9 Sample plot of Allan variance analysis results (after IEEE 952 1997)

With real data, gradual transitions would exist between the different Allan standard deviation slopes. A certain amount of noise or hash would exist in the plot curve due to the uncertainty of the measured Allan variance (IEEE Std 1293 1998).

4.5 ESTIMATION QUALITY OF ALLAN VARIANCE

In practice, estimation of the Allan variance is based on a finite number of independent clusters that can be formed from any finite length of data. The Allan variance of any noise terms is estimated using the total number of clusters of a given length that can be created. The confidence of the estimation improves as the number of independent clusters is increased.

Defining the parameters d_{AV} as the percentage error in estimating the Allan standard deviation of the cluster due to the finiteness of the number of clusters gives (IEEE 952 1997)

$$d_{AV} = \frac{s(T,M) - s(T)}{s(T)} \tag{4.65}$$

where $s(T,M)$ denotes the estimate of the Allan standard deviation obtained from M independent clusters, $s(T,M)$ approaches its theoretical value, $s(T)$, in the limit of M approaching infinity. A lengthy and straightforward calculation (Papoulis 1991) shows the percentage error is equal to

$$s(d_{AV}) = \frac{1}{\sqrt{2\left(\frac{N}{n} - 1\right)}} \tag{4.66}$$

where N is the total number of data points in the entire data set, and n is the number of data points contained in the cluster.

Equation (4.66) shows that the estimation errors in the region of short (long) T are small (large) as the number of independent clusters in these regions is large (small). For example, if there are 20,000 data points and cluster sizes of 5,000 points are used, the percentage error in estimating $s(T)$ is approximately 40%. On the other hand, for cluster containing only 100 points, the percentage error is about 5%.

4.6 SUMMARY

This chapter introduces the definition and properties of Allan variance as a tool for modeling inertial sensor errors. If the total data points and sample rate are known, it is easy to obtain Allan variance solution with Equation (4.5) or (4.9). According to the log-log plot of Allan standard deviation versus cluster length, different noise terms can be easily identified and extracted. The noise coefficients abstraction is discussed in Section

4.3. The method used to determine the estimation accuracy is discussed in Section 4.5. From above discussion, it is convenient to identify the existing noise terms and estimate the coefficients for a given data set. The application of Allan variance method for inertial sensors will be given in detail in next chapter.

CHAPTER FIVE: TEST AND RESULT

The purpose of the tests conducted in this chapter is to identify noise terms existing in different grade IMU sensors. The tests are conducted using the Allan variance technique presented in Chapter Four, which is expected to provide better understanding of the inertial sensors performance and noise sources.

5.1 TEST ENVIRONMENT

Three different grade IMUs were involved in evaluating the use of Allan Variance in modeling inertial sensor noise. The IMUs include the Honeywell CIMU navigation grade IMU, the Honeywell HG1700 tactical grade IMU and the Systron Donner MotionPak II-3g consumer grade MEMS based IMU. The test was held at room temperature for seven days at the Mobile Multi-Sensor System (MMS) research group Inertial Lab, in the Geomatics Engineering department of The University of Calgary. The test layout and the equipment used in this test are shown in Figure (5.1). All of the analysis presented in this chapter was conducted using the MMS research group Allan Variance (AV) Tool Box. The AV Tool Box was developed by the author, and was implemented under the Matlab® environment (http://www.mathworks.com/). The following sections provide the details and the characteristics of the tested IMUs and the data acquisition system.

5.1.1 CIMU TERRAMATICS BOX

The Commercial Inertial Measurement System (CIMU) (Figure (5.1B)) is a relatively small (i.e. a cube 13.4cm high with 19.3cm length and 16.9cm width) navigation grade

IMU manufactured by Honeywell International Inc. (http://www.honeywell.com/). The gyro-in-run bias is about 0.0022°/h and random walk is about 0.0022 °/$h^{1/2}$. The accelerometer in run bias is about 25 µg and noise is about 0.00076 m/s/$h^{1/2}$ (0.0025 FPS/$h^{1/2}$).

5.1.2 HG1700 TERRAMATICS BOX

The Honeywell HG1700 (Figure (5.1B)) is a lightweight cylinder 7.6 cm high and 9.4 cm in diameter, and is equipped with a low-cost tactical grade IMU that utilizes 3 GG1308 miniature ring laser gyros (RLGs) along with 3 Honeywell RBA-500 resonant beam digital accelerometers to measure angular rate and linear acceleration, respectively. This IMU has a gyro bias repeatability of better than 3°/h, gyro scale-factor accuracy of better than 150 ppm, and a gyro random-walk PSD level of less than 0.15 °/$h^{1/2}$. The accelerometer residual bias is less than 1000 µg, scale factor stability is 300 ppm, and linearity is 500 ppm.

The Terramatics Data Acquisition Board Box (Terramatics Inc., Calgary, Canada) was used to perform data acquisition for the CIMU and HG1700 units as well as time tagging of the inertial measurement unit. The inertial sensor output data are decoded at 200Hz data rate for the CIMU and 100Hz data rate for the HG1700. The output of gyro data is the delta angle with units in radians, and that of accelerometer is the delta velocity with units in m/s.

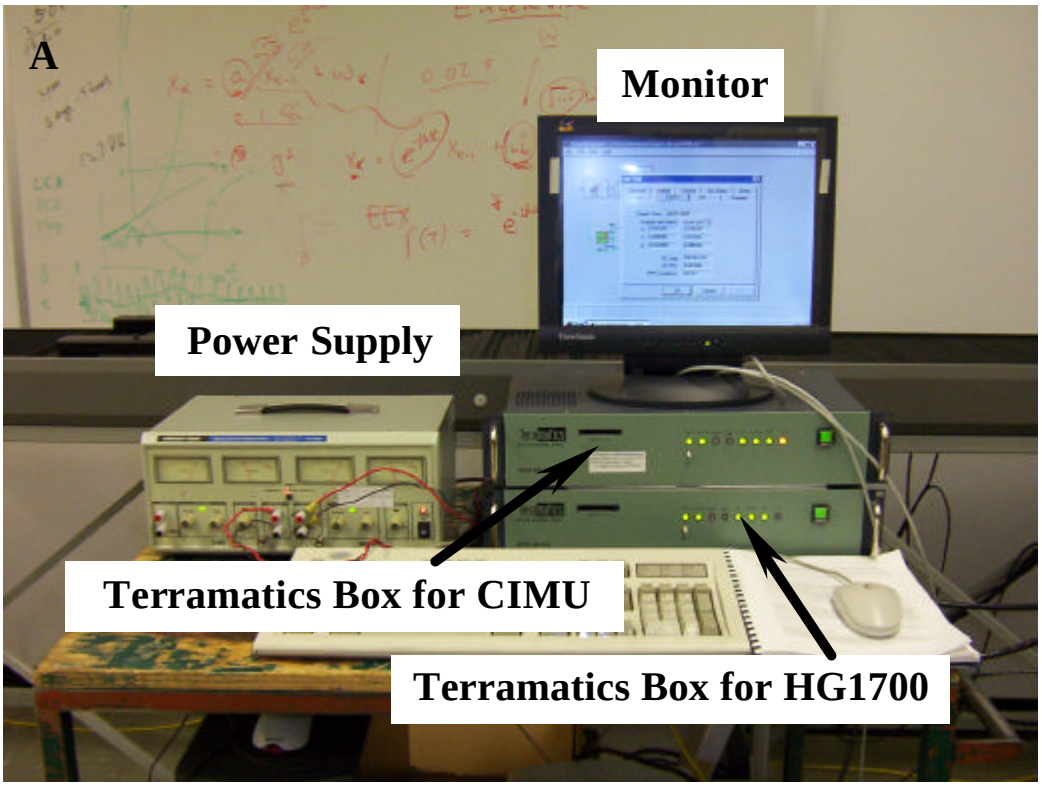

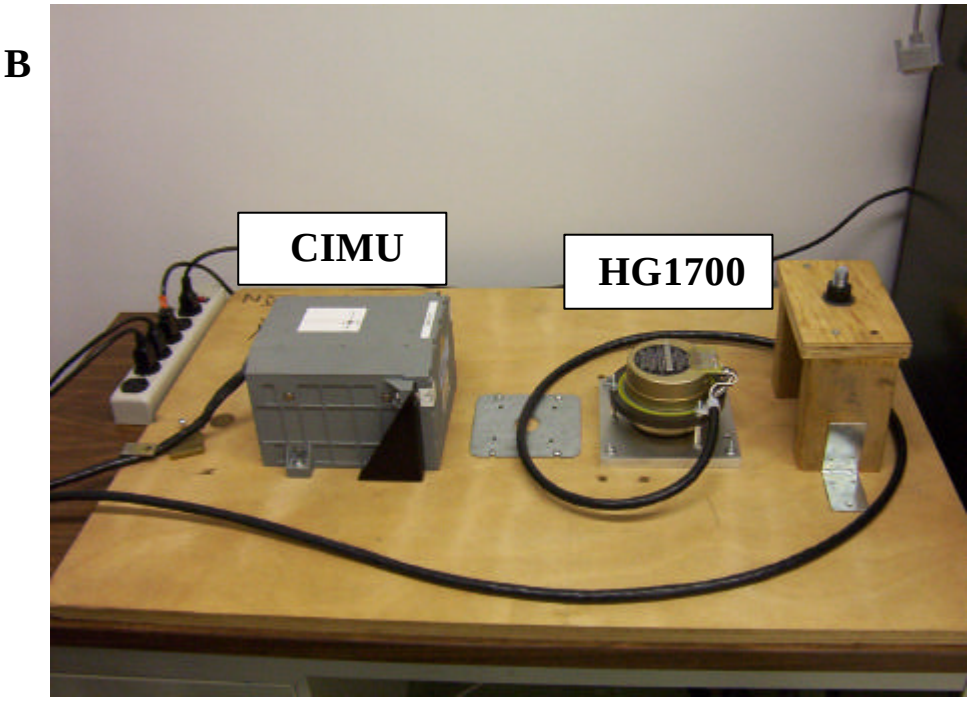

Figure 5.1 Test Environment Setup

5.1.3 MOTIONPAK II ANALOG OUTPUT

The MotionPak® is a solid-state six Degree-of-Freedom inertial sensing system used for measuring linear accelerations and angular rates in instrumentation and control applications. It uses three orthogonally mounted solid-state micro-machined quartz angular rate sensors, and mounted in a compact, rugged package are three high performance linear servo accelerometers with internal power regulation and signal conditioning electronics. Maximum bias error is ±5°/s for gyro and ±200mg for accelerometers. The bandwidth is larger than 30Hz for gyro and 250Hz for accelerometers (http://www.systron.com/).

For this unit the data was collected using the National Instruments (http://www.ni.com/) DAQCard™-6036E, which has 16 Inputs/2 Outputs, 200kS/s, 16-bit Multifunction I/O. The software used for acquiring and storing data is the National Instrument LabVIEW 7.0. The connection flow is shown as in Figure (5.2).

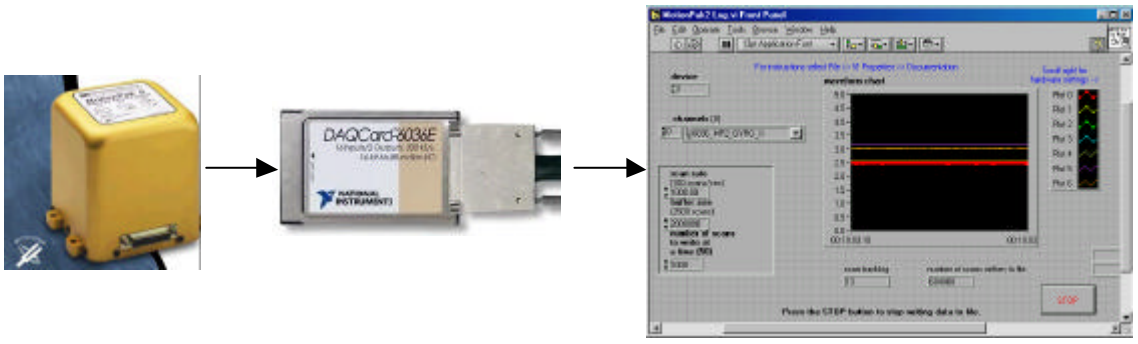

MotionPak II DAQCard™ 6036E LabVIEW 7.0

Figure 5.2 MotionPak II Data Acquiring System

5.1.4 ALLAN VARIANCE (AV) TOOL BOX

The Allan Variance (AV) Tool Box is developed by the author under the Matlab environment according to the methodology described in Chapter Four.

The input data of the AV Tool Box should be transformed into the unit as deg/h for gyros and m/s/h for accelerometers. Three-axis sensor data can be loaded at the same time. In addition, the input parameters include the number of total data points, sample rate, and the IMU type. Then the AV Tool Box will output the Allan variance result plot and the identified noise coefficients.

The AV Tool Box has been successfully applied in the following test data analysis. The corresponding results and explanation are provided.

5.2 TEST RESULTS

5.2.1 CIMU ALLAN VARIANCE ANALYSIS

Two-hour static data were collected from the CIMU IMU at room temperature. The entire data was then analysed using the AV Tool Box. A log-log plot of CIMU three axis gyros' Allan standard deviation versus cluster time is shown in Figure (5.3).

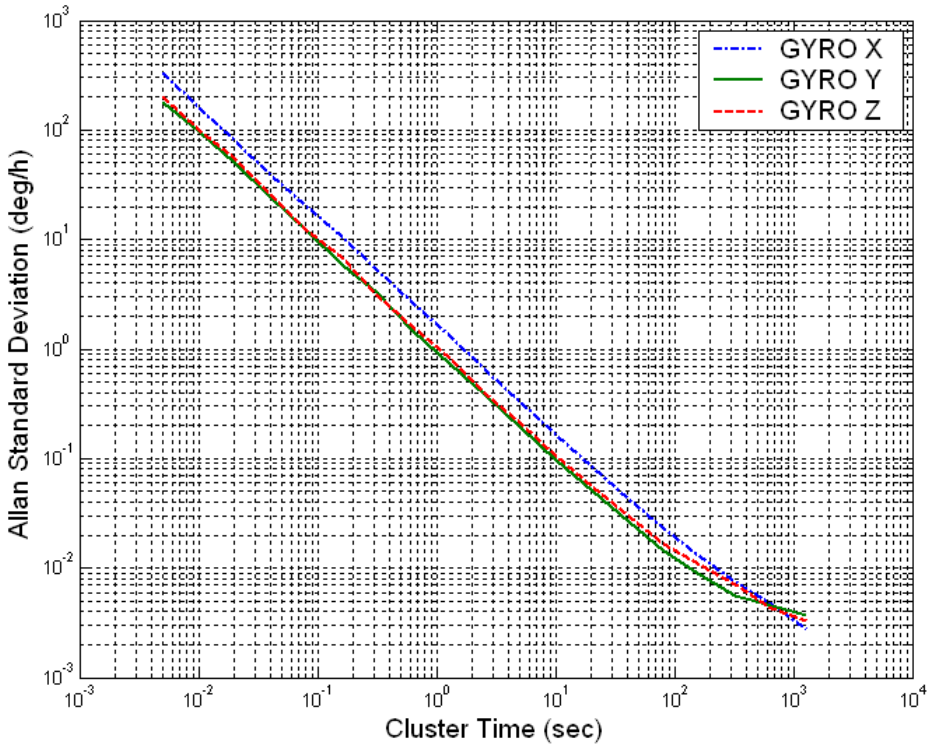

Figure 5.3 CIMU Gyro Allan variance results

Figure (5.3) clearly indicates that the quantization noise is the dominant noise for short cluster times. Figure 5.4 shows an example of how to obtain quantization noise coefficient from the Allan variance result in a log-log plot for CIMU Z-axis gyro. A straight line with slope of -1 (refer to the dashed line in the figure), fitted to the beginning of the plot meets $T = 3^{1/2}$ *hour* line (see Section 4.3.1) at a value of 1.60×10^{-4} deg (Point A in Figure 5.4), which is equal to 0.5770 arc seconds. Since the estimation of quantization noise is based on very short cluster times, the number of independent clusters is very large and the quality of estimation is very good. In fact, even for cluster time as long as T=100 sec, according to Equation (4.66), the percentage error is only 7.58%. In fact, the estimation percentage error can be reduced to 2.7%, making the line with slope of -1 to cover only the region from T=0.05 sec till T=10sec. The value of

percentage error is equal to 0.5770 $\times$ 2.7% = 0.0155 arc seconds. Thus the quantization coefficient for CIMU Z-axis gyro is estimated as:

$$Q_z = (0.5770 \pm 0.0155) arc\sec \tag{5.1}$$

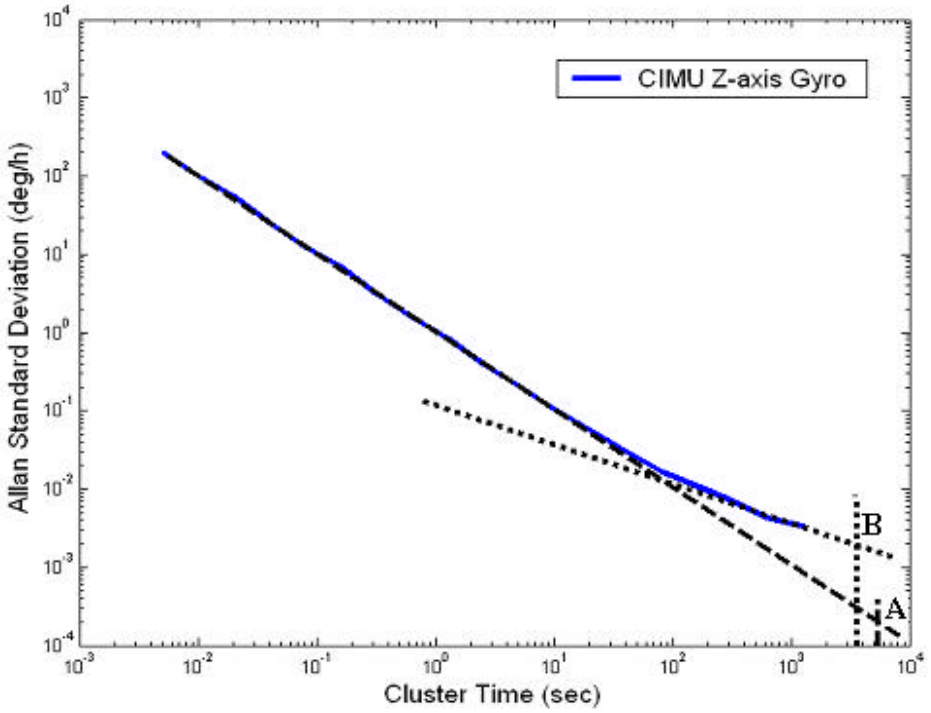

Figure 5.4 CIMU Z-axis Gyro Allan variance result with slopes of –1 and –1/2

Table (5.1) lists the estimated quantization noise coefficients for seven days tests for all three axes gyros. It is clear that the standard deviation of the seven days tests is smaller than the estimation percentage error as shown in Table (5.2), which means that the CIMU sensor random processes have very good repeatability. In conclusion, each individual test result of CIMU can be used for system prediction and analysis.

Table 5.1 CIMU Gyro Quantization Noise Estimation Results			
	Gyro X (arcsec)	Gyro Y (arcsec)	Gyro Z (arcsec)
Day1	0.9732	0.5174	0.5770
Day2	0.9601	0.5357	0.6023
Day3	0.9193	0.5059	0.5745
Day4	0.9472	0.4982	0.5693
Day5	0.9577	0.4992	0.5592
Day6	0.9589	0.5065	0.5624
Day7	0.9450	0.5068	0.5785
STD	0.0170	0.0129	0.0141

In Figure (5.3) there is also a clear indication that the angle random walk is the dominant noise term for long cluster times. There is an example in Figure (5.4) to show how to obtain the random walk coefficients from the Allan variance log-log plot result. A straight line with slope of $-1/2$ (the dotted line) is fitted to the long cluster time part of the plot and meets the T=1 *hour* line (see Section 4.3.2) at a value of 0.0018 (Point B in Figure 5.4). The unit of angle random walk is $\mathrm{deg/h^{1/2}}$. Inspection of the curve shows that the estimation percentage error in this region can reach to 33.36% according to Equation (4.66). The value of the percentage error is calculated as $0.0018 \times 33.36\% = 0.0006$ $\mathrm{deg/h^{1/2}}$. Thus the angle random walk coefficient for CIMU Z-axis gyro is estimated as:

$$Q = (0.0018 \pm 0.0006)\,\mathrm{deg}/\sqrt{h} \tag{5.2}$$

For two hours of static CIMU accelerometer data, the Allan variance results are shown in Figure (5.5). The figure clearly indicates that the quantization noise is the prominent noise term in short cluster times while the drift rate ramp noise term in long cluster times.

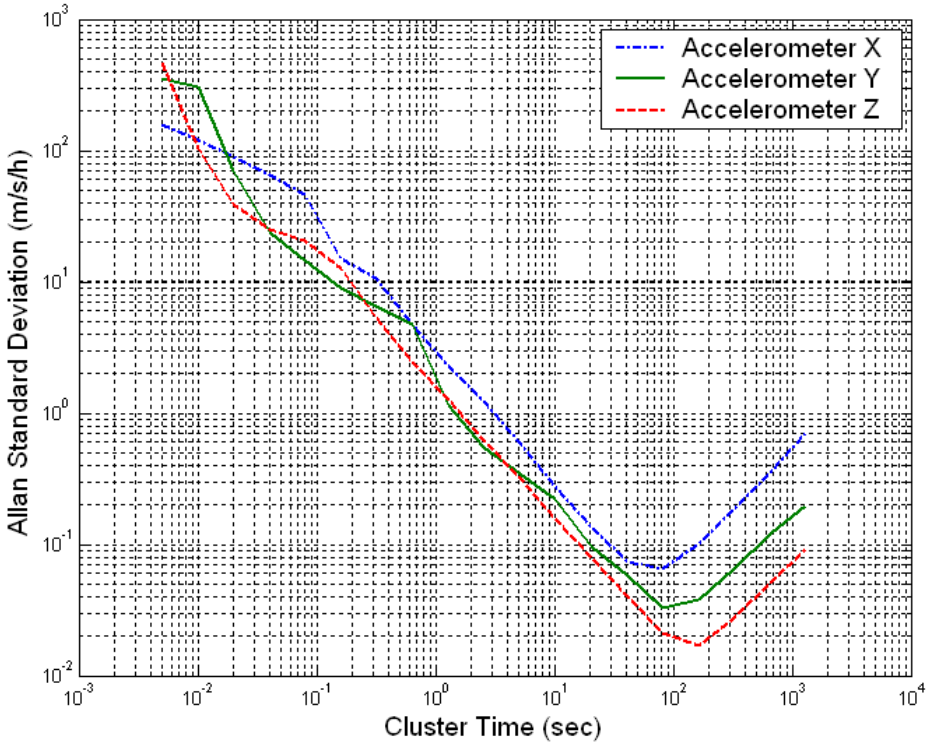

Figure 5.5 CIMU Accelerometer Allan variance results

In Figure (5.6), there is an example shown for how to obtain drift rate ramp noise coefficient from the Allan variance log-log plot. A straight line with slope of +1 (the dashed line) is fitted to the long cluster time part of the plot and meets T = $2^{1/2}$ hour line (see Section 4.3.5) at a value of 0.3915. The unit for velocity drift rate ramp is m/s/h^2. Inspection of the curve shows that the estimation percentage error in this region can reach 33.36% according to Equation (4.66). The value of the percentage error is equal to 0.3915 × 33.36% = 0.1309 m/s/h^2. Thus the drift rate ramp coefficient for CIMU Z-axis accelerometer is estimated as:

$$R = (0.3915 \pm 0.1309)\, m/s/h^2 \tag{5.3}$$

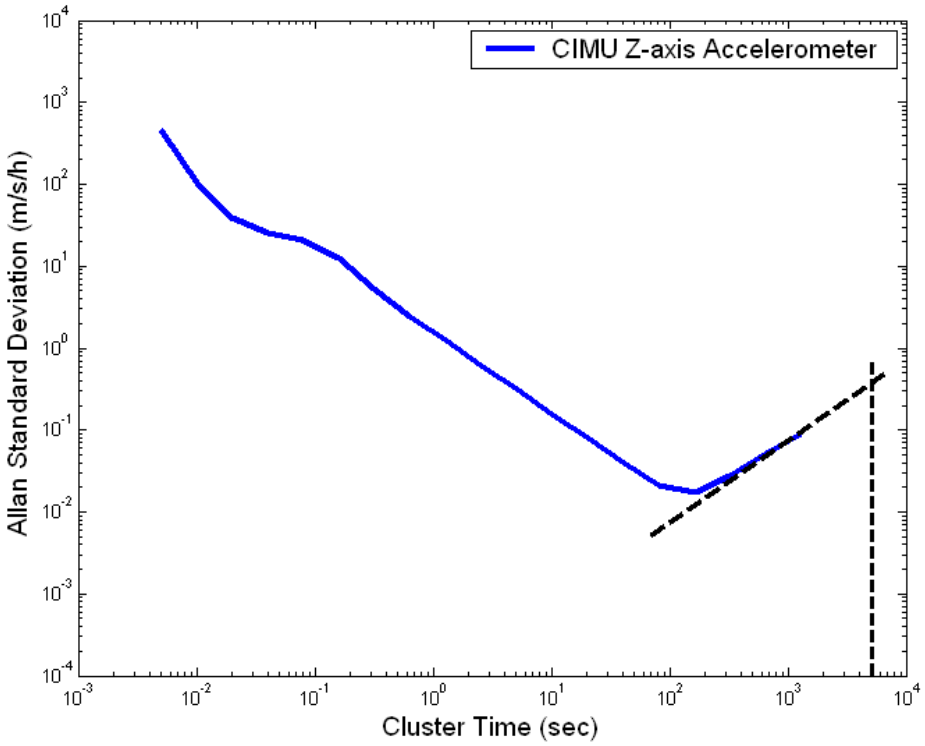

Figure 5.6 CIMU Z-axis Accelerometer Allan variance result with slopes of –1 and +1

Table (5.2) lists all the identified noise coefficients for the CIMU two-hour static data.

Table 5.2 Identified Noise Coefficients for CIMU

	Quantization (arcsec)	Random Walk (deg/√h)		Quantization (m/h)	Rate Ramp ($m/s/h^2$)
Gyro X	0.9732±0.0738	0.0015±0.0005	Accl X	1.6801±0.1275	2.6364±0.8795
Gyro Y	0.5174±0.0197	0.0019±0.0006	Accl Y	1.2980±0.0985	0.8915±0.2974
Gyro Z	0.5770±0.0155	0.0018±0.0006	Accl Z	0.8785±0.0666	0.3915±0.1309

5.2.2 HG1700 ALLAN VARIANCE ANALYSIS

Two-hour static data from HG1700 were collected at room temperature. Applying the Allan variance method to the whole data set, a log-log plot of HG1700 three axis gyros' Allan standard deviation versus cluster time is shown in Figure (5.7).

From the Allan variance result, for two hours of static HG1700 gyro data, it is clear that the quantization noise is the dominant noise for short cluster times while the angle random walk is the dominant noise for long cluster times. The methodology for obtaining noise coefficients has been discussed in the previous section. Table (5.3) lists the estimated quantization noise coefficients for seven days tests for all three axes HG1700 gyros. The results clearly indicate that the standard deviation for the seven days of tests is close to the estimation percentage error as listed in Table (5.4). That means that the HG1700 sensor random processes have relatively good repeatability. To conclude, each individual test result of HG1700 can be used as system prediction and analysis.

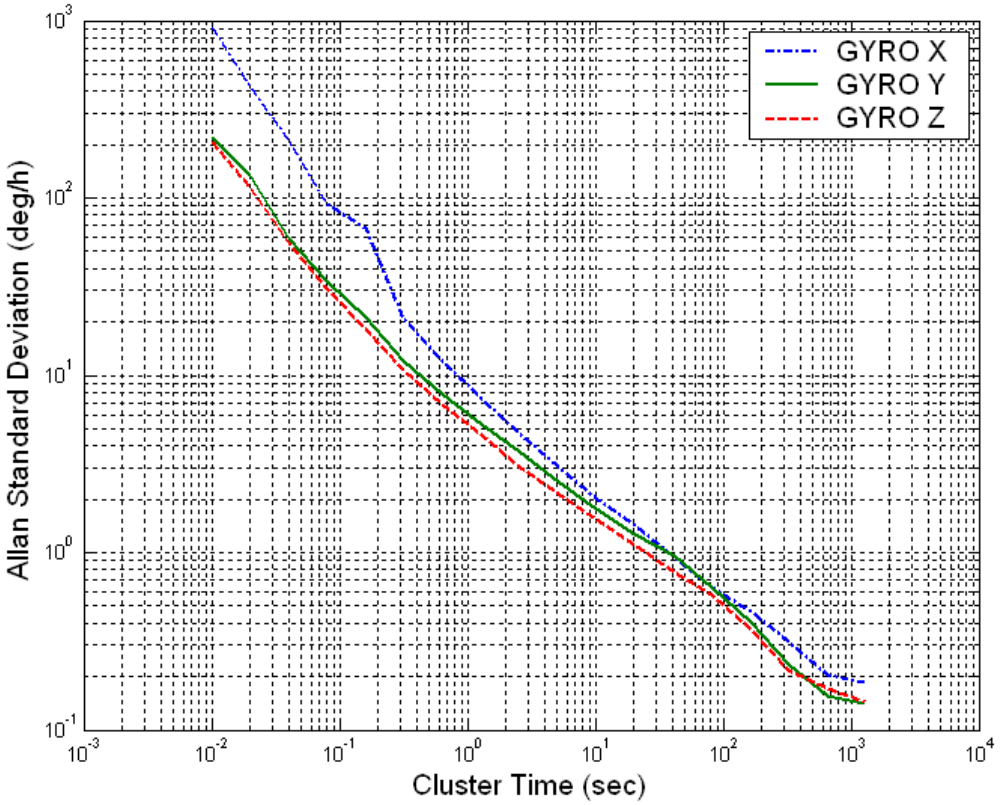

Figure 5.7 HG1700 Gyro Allan variance results

Table 5.3 HG1700 Gyro Quantization Noise Estimation Results			
	Gyro X (arcsec)	Gyro Y (arcsec)	Gyro Z (arcsec)
Day1	5.1154	1.2742	1.2316
Day2	5.1117	1.2842	1.2025
Day3	5.1113	1.2801	1.2227
Day4	5.1239	1.3065	1.2256
Day5	5.0312	1.2864	1.2193
Day6	5.1051	1.3054	1.2065
Day7	5.0487	1.2954	1.2226
STD	0.0366	0.0124	0.0104

For two hours of static HG1700 accelerometer data, the Allan variance results are shown in Figure (5.8). It is seen that the quantization noise is the prominent noise term in short cluster times while the rate random walk noise term in long cluster times. There is an example to show how to obtain the rate random walk coefficient in Figure (5.9). For HG1700 Z-axis accelerometer Allan variance result plot, Figure (5.9), a straight line with slope of +1/2, the dashed line, fitted to the long cluster time part of the plot and meets T = 3 hour line (see Section 4.3.4) at a value of 3.3514. The unit of the velocity rate random walk is m/s/h/$h^{1/2}$. Inspection of the curve shows that the estimation percentage error in this region can reach 33.36% according to Equation (4.66). The value of the percentage error is equal to 3.3514×33.36%=1.1180 m/s/h/$h^{1/2}$. Thus the rate random walk coefficient for HG1700 z-axis accelerometer is estimated as:

$$K = (3.3514 \pm 1.1180)\, m/s/h/\sqrt{h} \tag{5.4}$$

Table (5.4) listed all the identified noise coefficients for HG1700 two hours static data set.

Table 5.4 Identified Noise Coefficients for HG1700					
	Quantization (arcsec)	Random Walk (deg/√h)		Quantization (m/h)	Rate Random Walk (m/s/h/√h)
Gyro X	5.1154±0.0683	0.0936±0.0312	Accl X	2.1188±0.0673	0.7637±0.2548
Gyro Y	1.2742±0.0032	0.0883±0.0295	Accl Y	2.1988±0.1176	1.1572±0.3860
Gyro Z	1.2316±0.0028	0.0753±0.0251	Accl Z	2.1845±0.0583	3.3514±1.1180

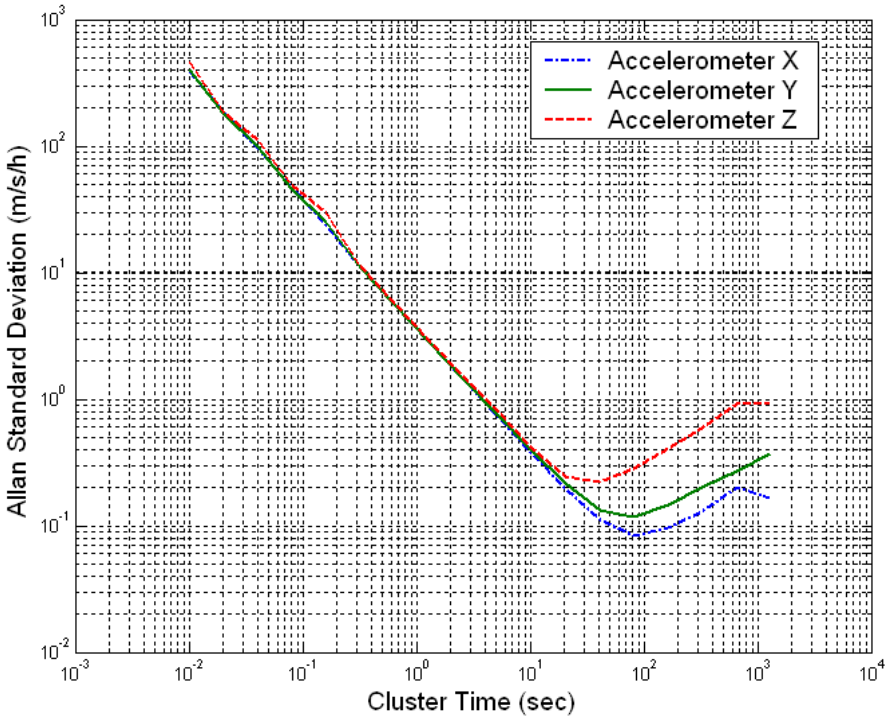

Figure 5.8 HG1700 Accelerometer Allan variance results

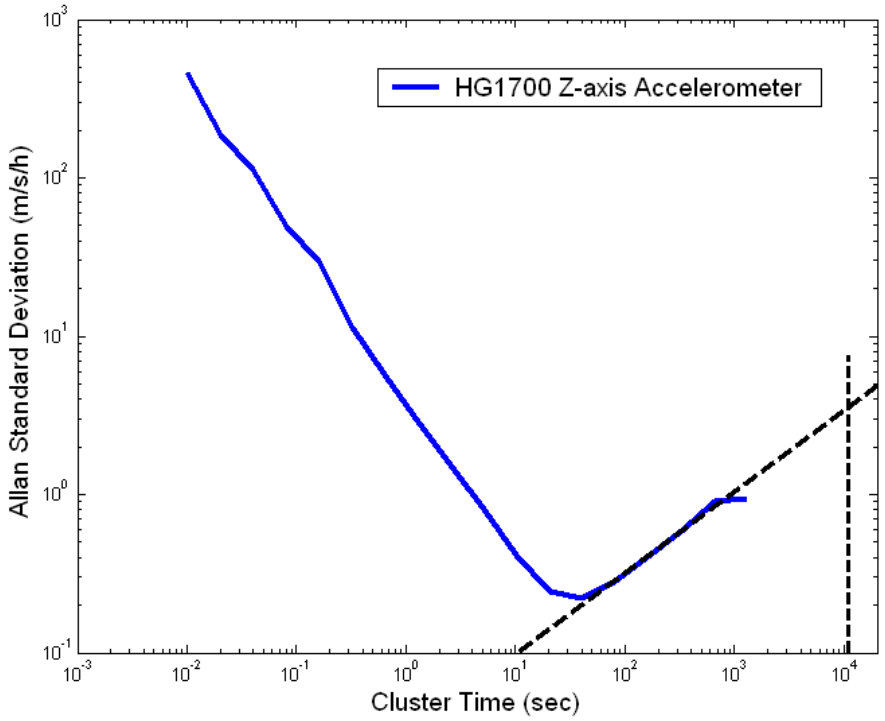

Figure 5.9 HG1700 Z-axis Accelerometer Allan variance result with slopes of –1 and +1/2

5.2.3 MOTIONPAK II ALLAN VARIANCE ANALYSIS

Since data integration is used in the Allan variance analysis (Equation (4.6)), when collecting data through A/D card, the sample rate will affect the Allan variance result. In order to check the data-sampling rate effect on the Allan variance result and the fact that the MotionPak II provides analog data, different sampling rate data sets were collected for the system through the A/D card.

Using the A/D card with the National Instrument LabVIEW 7.0 software, 10 minutes data sets at different sampling rates (10Hz, 50Hz, 100Hz, 500Hz, 1000Hz, and 2000Hz) were collected separately. Applying the Allan variance method to all the data sets, the Allan variance results are shown in Figure (5.10).

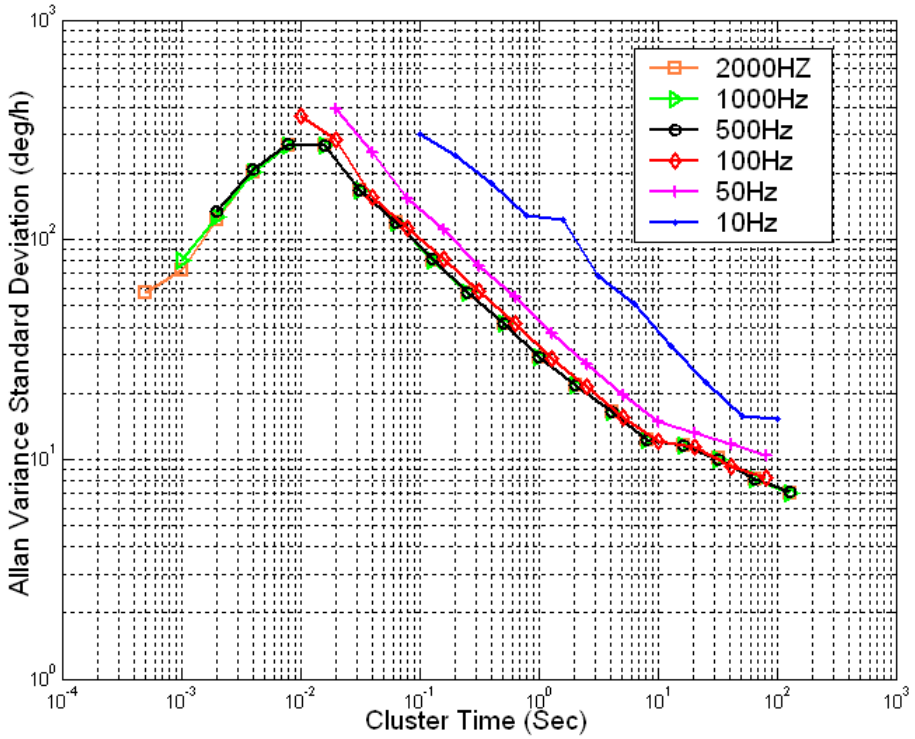

Figure 5.10 MotionPak II Gyro X Allan Variance Sample Rate Test Result

Figure (5.10) clearly shows similar results for data rates higher than 100Hz sampling rate. The attenuation in the high frequency part (i.e. T < 0.01 sec) is the embodiment of the sensors bandwidth. From the data sheet of MotionPak II, the bandwidth of gyros is larger than 30Hz. Therefore; the sampling rate should reach three to five times the bandwidth to meet the requirement for reliable sensor performance analysis, which also meets the requirement of Nyquist theorem. Therefore, the sample rate for the MotionPak II gyro is set as 100Hz while that for accelerometer is set as 1000Hz.

Two-hour static data from MotionPak II was collected at room temperature at the above recommended data rate. Applying the Allan variance method to the whole data set, a log-log plot of MotionPak II three axis gyros' Allan standard deviation versus cluster time is

shown in Figure (5.11). From the Allan variance result, for two hours static MotionPak II gyro data, it is clear that the angle random walk noise is the dominant noise in short cluster times while the bias instability noise term is the dominant noise term in long cluster times.

What follow is an example of how to obtain the bias instability noise coefficient from the Allan variance results. For the MotionPak II Z-axis gyro Allan variance result plot in Figure (5.12), the almost flat part of the curve of long cluster part is indicative of the low-frequency noise, which determines the bias variations of the run. The dashed line, a zero slope line, which is fitted to the bottom of the curve determines the upper limit of bias instabilities. Such a line meets the ordinate axis at a value of 11.1488 and dividing this by 0.664 (see Section 4.3.3) yields the maximum bias instability value of 16.79 deg/h. Analysis of the curve indicates that the estimation percentage error in this region is approximately 10% according to Equation (4.66). The value of the percentage error is equal to 16.79 $\times$ 10% = 1.68 deg/h. Thus the bias instability coefficient for MotionPak II Z-axis gyro is estimated as:

$$B = (16.79 \pm 1.68)\text{deg}/h \tag{5.5}$$

The method described above can be used to acquire the bias instability coefficient from Allan variance result plot.

Figure (5.13) shows the Allan variance results for two hours of static MotionPak II three axes accelerometer data collected at the above recommended data rate. The results clearly indicates that, for the MotionPak II accelerometers, the velocity random walk is the

dominant noise term in the short clustering time while the bias instability noise term is the dominant noise in the long clustering time. The identified noise coefficients for MotionPak II are listed in Table (5.5).

Table 5.5 Identified Noise Coefficients for MotionPak II

100Hz Data	Random Walk ($deg/h^{1/2}$)	Bias Instability (deg/h)	1000Hz Data	Random Walk ($m/s/h^{1/2}$)	Bias Instability (m/s/h)
Gyro X	0.5121±0.0068	13.58±1.36	Accl X	0.01664±0.00003	4.36±0.04
Gyro Y	0.4859±0.0065	11.69±1.17	Accl Y	0.01593±0.00003	4.09±0.08
Gyro Z	0.4891±0.0065	16.79±1.68	Accl Z	0.01612±0.00003	4.36±0.08

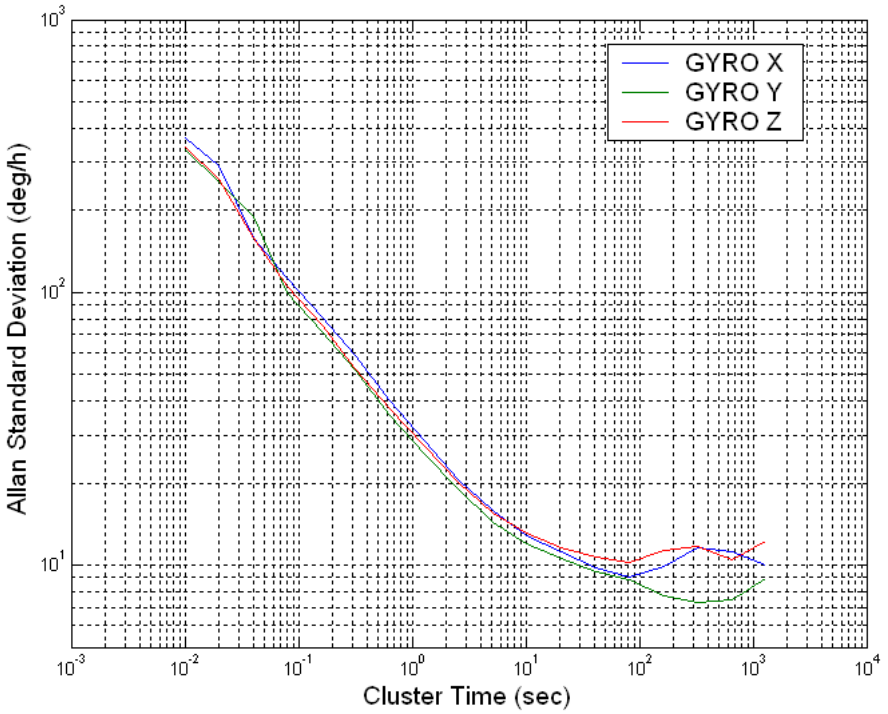

Figure 5.11 MotionPak II Gyro Allan Variance Test Results

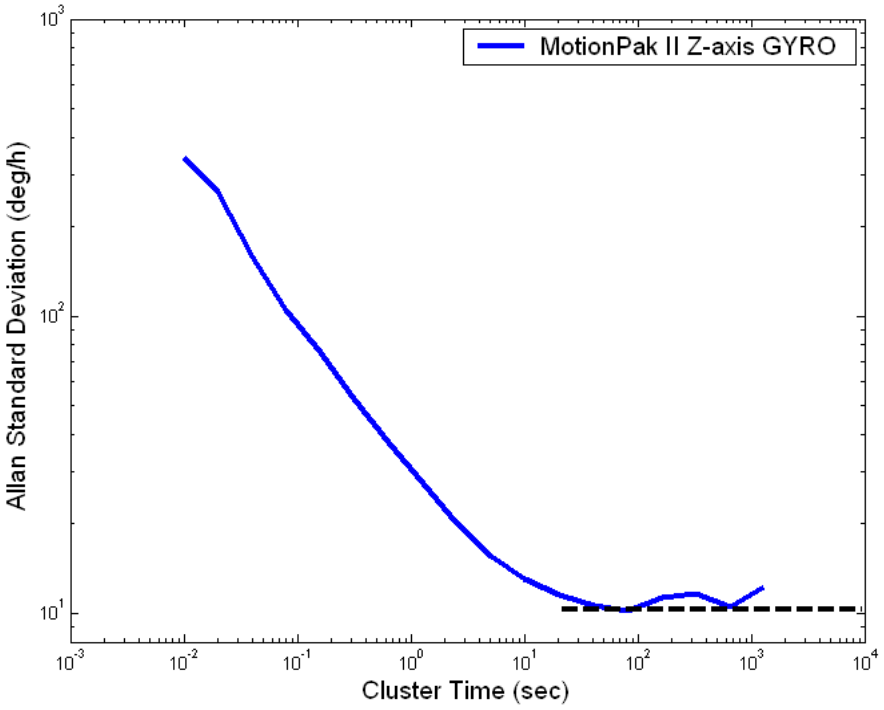

Figure 5.12 MotionPak II Z-axis Gyro Allan Variance Result with slope of –1/2 and 0

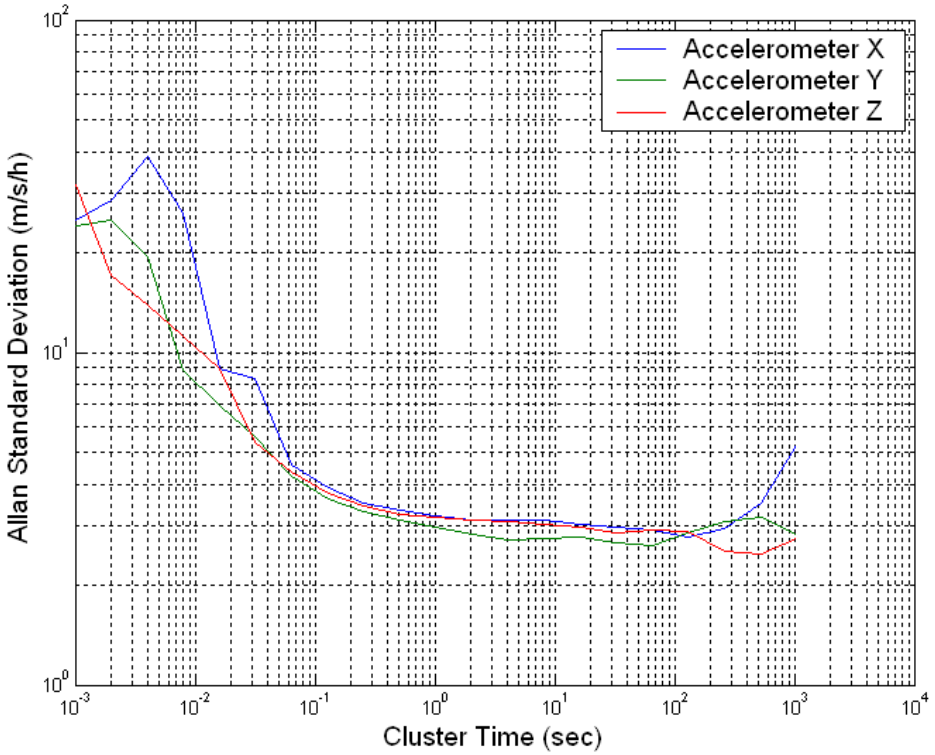

Figure 5.13 MotionPak II Accelerometer Allan Variance Results

5.3 SUMMARY

The Allan variance method presented has proven to be able to identify the characterization of various random errors contained in the output data of inertial sensors. By performing a simple operation on the entire length of data, a characteristic curve is obtained whose inspection facilitates the determination of the different types and magnitude of noise terms existing in inertial sensors.

The identified noise terms for two-hour static data from gyros and accelerometers of different grades of IMUs are listed in Table (5.6).

Table 5.6 Summary of Identified Noise Terms

		Quantization	Angle random walk	Bias instability	Rate random walk	Drift rate ramp
Gyro	CIMU	√	√			
	HG1700	√	√			
	MP2		√	√		
		Quantization	Velocity random walk	Bias instability	Rate random walk	Drift rate ramp
Accelero-meter	CIMU	√				√
	HG1700	√			√	
	MP2		√	√		

It should be noted that the noise terms, which haven't been identified, may need long-term test data to prove whether or not they exist.

By comparing the estimated noise coefficients obtained from power spectral density, listed in Table (3.5) with Allan variance method, Table (5.2) for CIMU and Table (5.5) for Motion Pak II, the noise coefficient is identical for same noise term. Consequently, the Allan variance method performed in this thesis work is correct.

In addition, the noise coefficients can be read off directly from the Allan variance result plot. For power spectral density method, the frequency averaging technique should be applied first to make the slopes of the curve distinguishable. Then, further calculation is needed to obtain the coefficients. Thus, the procedure of parameter abstraction for Allan variance is much simpler than that for power spectral density. As a conclusion, Allan variance method is more suitable for inertial system performance analysis and prediction.

CHAPTER SIX: CONCLUSIONS AND RECOMMENDATIONS

6.1 CONCLUSIONS

Compared to the stochastic modeling methods discussed in Chapter Three, Allan variance has many advantages in inertial sensor noise term analysis and modeling.

The autocorrelation method is useful in modeling Gauss-Markov processes. But, in order to reveal the parameters, test data needs to be de-noised first. In addition, autocorrelation methods need very long term static data to produce results within an acceptable range, especially for the sensors in the high grade IMU's. From experience, the correlation time is very long for high grade IMUs; the test can even take a few weeks.

The power spectral density method is straightforward but the computation is complex and difficult for non-system analysts to understand. After the calculations are performed, the results need to be simplified through the frequency averaging technique. Even after that, it is complex to extract the parameters of the identified noise terms from the result plot.

On the other hand, the Allan variance method is a finer, easier characterization and identification of error sources and their contribution to the overall noise statistics.

Seven-day static data from CIMU, HG1700, and MotionPak II-3g IMUs were investigated. Approximately 80% of results are close to the manufacture claimed

performance characteristics of these units, which prove the reliability of the Allan Variance method. Overall, the results obtained from the data analysis indicate that:

- The quantization noise is the dominant noise term in short cluster times while the angle random walk noise term is the dominant noise in long cluster times for the gyros used in the CIMU and HG1700 IMUs. For the accelerometers, the quantization noise is the dominant noise term in short cluster times while the rate random walk and drift rate ramp is the dominant noise in long cluster times for HG1700 and CIMU, respectively.

- The results of the MotionPak II sensors clearly indicate that random walk is the dominant noise term in the short clustering time while the bias instability noise terms are the dominant noise in the long clustering time.

- When colleting data through the A/D card, the Nyquist theorem should be utilized. The recommended sampling frequency should be three to five times of sensor bandwidth to meet the requirement for reliable sensor performance analysis.

Based on the above analysis, the Allan variance method is helpful in IMU analysis and modeling for both manufacturers and users. Manufacturers can improve sensor performance based on the identified noise terms. Users can better model sensor performance according to the existing noise terms within the sensor output.

Consequently, the author expects that Allan variance will attract more and more attention in the field of INS sensors analysis and modeling.

6.2 RECOMMENDATIONS

Identification and modeling the noise terms within the inertial sensors was the main objective of this thesis. There is still a long road ahead to improve the navigation solution with all these results. What follows are a few recommendations from the author's point of view in the application of the results and the potential for further research work:

- Quantization noise, which has been identified in CIMU and HG1700 gyro and accelerometer sensors, is strictly due to the digital nature of the sensor output. Inertial sensor quantization error generally is a minor contributor to attitude/ velocity/ position and initial heading determination inaccuracy in a strapdown INS. However, mis-modeling of quantization error effects can result in erroneously large estimates of their impact on INS performance (Savage 2002). In future work, it is necessary to add the quantization noise into the stochastic model.

- Random walk is an important noise term and can be used to evaluate the sensor noise intensity. In the Kalman filter design, the amplitude of random walk coefficients can be directly used in the process noise covariance matrix with respect to the appropriate sensor.

- The standard definition of bias instability used by inertial sensor manufacturers is the minimum point on the Allan variance curve. This is the best stability one could achieve with a fully modeled sensor and active bias estimation (Stockwell 2004). Thus, in future work, the minimum point on the Allan variance curve can be used in the inertial sensor bias instability estimation.

- Since the rate random walk and rate ramp have been identified by Allan variance method, in future work, these two noise terms should be considered in system modeling.

REFERENCE

Allan, D. W. (1966), "Statistics of Atomic Frequency Standards", Proceedings of IEEE, vol. 54, no. 2, pp. 221-230, Feb, 1966.

Allan, D.W. (1987), "Time and Frequency (Time-Domain) Characterization, Estimation, and Prediction of Precision Clocks and Oscillators", IEEE Transportations on Ultrasonics, Ferroelectrics, and Frequency Control, Vol. UFFC-34, no.6, pp.647-654.

Barbour, N.M., Elwell, J.M., and Setterlund, R.H. (1992), "Inertial Instruments—Where to Now", Proc. AIAA Guidance, Navigation and Control Conference, paper AIAA-92-4414-CP, Hilton Head, SC, August 1992, pp.566-574.

Blakelock, J.H. (1991), "Automatic Control of Aircraft and Missiles", Wiley, New York.

Brigham, E. O. (1988), "The Fast Fourier Transform and Its Applications", Englewood Cliffs, NJ: Prentice-Hall, Inc., 448 pp.

Britting, K. (1971), "Inertial Navigation Systems Analysis". New York: Wiley-Insterscience.

Brogan W. (1974), "Modern Control Theory". New York: Quantum Publishers.

Brown, R. G. (1983), "Introduction to Random Signal Analysis and Kalman Filtering", John Wiley & Sons, Inc. 1983.

El-Sheimy, N. (1996), "The Development of VISAT-A Mobile Survey System for GIS Applications", Report No. 20101, Department of Geomatics Engineering, The University of Calgary, Calgary, Canada.

El-Sheimy, N. (2003), ENGO 623 Lecture Notes: *Inertial Techniques and INS/DGPS Integration*, Department of Geomatics Engineering, The University of Calgary, Winter 2003.

Embree, P. M. and Danieli, D. (1999), "C++ Algorithms for Digital Signal Processing", Prentice-Hall, Inc.

Gelb, A. (1974), TASC Staff, "Applied Optimal Estimation", Cambridge MA: M.I.T. Press.

Gradshteyn, I. S. and Ryzhik, I. M. (1980), "Table of Integrals, Series, and Products", Americ Press.

Greenhall, C. A. (1998), "Spectral Ambiguity of Allan Variance", IEEE Transactions on Instrumentation and Measurement, Vol. 47, No.3, June 1998.

Grewal, Mohinder S., and Angus P. Andrews. (1993), "Kalman Filtering Theory and Practice". Upper Saddle River, NJ USA, Prentice Hall.

Hou, H. and El-Sheimy, N. (2003), "Inertial Sensors Errors Modeling Using Allan Variance", Best Presentation Winning Paper, The US Institute of Navigation, ION GPS/GNSS 2003 Proceedings, pp. 2860-2867, Sep 9-12, Portland, 2003.

IEEE Std 1139-1988, *IEEE Standard Definitions of Physical Quantities for Fundamental Frequency and Time Metrology*.

IEEE Std 952-1997 *IEEE Standard Specification Format Guide and Test Procedure for Single –Axis Interferometric Fiber Optic Gyros.*

IEEE Std 1293-1998 *IEEE Standard Specification Format Guide and Test Procedure for Linear, Single-Axis, Non-gyroscopic Accelerometers*.

Jacobs, O. L. R. (1993), "Introduction to Control Theory", 2nd Edition. Oxford University Press.

Kalman, R.E. (1960), "A New Approach to Linear Filtering and Prediction Problems", ASME Transactions, vol. 182D, Mar. 1960, pp.35-45.

Keshner, M. S. (1982), "1/f Noise", Proceedings of the IEEE, vol.70, no.3, pp.212-218, March 1982.

Kochakian, C.R. (1980), "Time-Domain Uncertainty Charts (Green Charts): A Tool for Validating the Design of IMU/Instrument Interfaces", Proceedings of the AIAA Guidance and Control Conference, Aug. 11-13, 1980.

Lachapelle, G., Petovello, M.G. and Zhang, H. (2003), "Assessment of A Motorola Single-Axis IMU", Technical Report to Motorola Inc. PLAN Group, Department of Geomatics Engineering, The University of Calgary, October 2003.

Lawrence C. Ng and DarryII J. Pines. (1997), "Characterization of Ring Laser Gyro Performance Using the Allan Variance Method", Journal of Guidance, Control, and Dynamics, Vol. 20, No. 1: Engineering Notes, p 211-214. January-February, 1997.

Lewis, R. (1986), "Optimal Estimation with an Introduction to Stochastic Control Theory", John Wiley & Sons, Inc.

Mallat, S. (1989), "A Theory for Multiresolution Signal Decomposition: The Wavelet Representation", IEEE Trans Patt Recog And Mach Intell 11(7), pp. 674-693.

Maybeck, Peter S. (1979), "Stochastic models, Estimation and Control", Volumn 1, Academic Press, Inc.

McRuer, D.T., Ashkenas, I., and Graham, D. (1973), "Aircraft Dynamics and Automatic Control", Princeton University Press, Princeton, NJ.

Merhav, S. (1982), "A Nongyroscopic Inertial Measurement Unit", AIAA Journal of Guidance, Control and Dynamics, Vol. 5, No.3, pp. 227-235, May-June.

Merhav, S. (1996), "Areospace Sensor Systems and Applications", Springer-Verlag New York, Inc.

Misiti, M. et al. (2000), "Wavelet Tool Box for The Use with Matlab", The Math Works Inc., MA, USA

Nassar, S. (2003), "Improving The Inertial Navigation System (INS) Error Model for INS and INS/DGPS Applications", UCGE Reports No. 20183, The University of Calgary Novenber 2003

Norling, B. (1990), "Accelerometers: Current and Emerging Technology", International Association of Geodesy Symposium No 107, Banff, Alberta, Canada, September 10-13, 1990.

Papoulis, A. (1965), "Probability, Random Variables and Stochastic Processes". New York: McGraw-Hill.

Papoulis, A. (1991), "Probability, Random Variables, and Stochastic Process", Third Edition, McGraw-Hill, Inc.

Savage, P. G. (1978), "Strapdown Sensors", NATO/AGARD Lecture Series 95, 1978.

Savage P.G. (2002), "Analytical Modeling of Sensor Quantization in Strapdown Inertial Navigation Error Equations", Journal of Guidance, Control, and Dynamics, vol. 25, No. 5, September-October 2002.

Schwarz, K.P., and El-Sheimy, N. (1999), "Future Positioning and Navigation Technologies" Study performed under the Scientific Services Agreement with

Batelle, Columbus Division and Topographic Engineering Center, Fort Belvoir, VA, USA.

Sinha, N. K. and Kuszta, B. (1983), "Modeling and Identification of Dynamic Systems", New York: Van Nostrand Reinhold.

Smith, R. B. and Weyrauch, J. A. (1990), "Gyroscopes: Current and Emerging Technologies", International Association of Geodesy Symposium No. 107, Banff, Alberta, Canada, September 10-13, 1990.

Sorenson, H. W. (1970), "Least –Squares estimation: from Gauss to Kalman", IEEE Spectrum, vol.7, pp. 63-68, July 1970.

Stockwell, W. (2004), "Bias Stability Measurement: Allan Variance", Crossbow Technology, Inc. Visited February 26, 2004. http://www.xbow.com/Support/Support_pdf_files/Bias_Stability_Measurement.pdf

Tehrani, M. M. (1983), "Ring Laser Gyro Data Analysis with Cluster Sampling Technique", Proceedings of SPIE, vol. 412.

Titterton, D. H. and Weston J. L. (1997), *Strapdown Inertial Navigation Technology*, Peter Peregrinus Ltd.

Van Trees, H. L. (1968), "Detection, Estimation, and Modulation Theory", Part I, New York: John Wiley and Sons.

Verplaetse, C. (1995), "Can A Pen Remember What It Has Written Using Inertial Navigation?: An Evaluation Of Current Accelerometer Technology**",** Class Paper, Physics and Media group, MIT, 1995.

Weinberg, H. (2004), "MEMS (Micro Electro-Mechanical Systems) Technology ", http://www.sensorland.com/HowPage023.html, visited June 20, 2004.

Welch, G. and Bishop, G. (2004), "An Introduction to the Kalman Filter", available from http://www.cs.unc.edu/~welch/kalman/kalman_filter/kalman.html Updated April 5th, 2004.

Wiener, N. (1961), "Cybernetics: or Control and Communication in the Animal and Machine", Cambridge, MA: MIT Press, 1948, Second Edition.

Yun, W. and Howe, R. T. (1991), "Silicon Microfabricated Accelerometers: A Perspective on Recent Developments", Sensors Expro Proceedings.